

ABSTRACT

Title of Dissertation: FUNCTIONALIZATION OF NANOPARTICLES
 FOR BIOLOGICAL APPLICATIONS

Isaac Koh, Doctor of Philosophy, 2005

Directed By: Sheryl H. Ehrman, Associate Professor
 Department of Chemical and Biomolecular Engineering

Functionalization of metal oxide nanoparticles enables their use in biological applications via hybridization of biological molecules and modification of surface properties. This Ph. D research is aimed at increasing knowledge of the process of metal oxide nanoparticle functionalization for biological applications. The achievements presented in this dissertation can be divided into three categories: i) a fluorescence-based quantitative evaluation of surface coverage and bio-activity of antibodies immobilized on magnetic nanoparticles (MNPs), ii) differential functionalization of SiO₂/TiO₂ mixed nanoparticles via preferential binding of phosphonic acids to TiO₂ and subsequent trimethyl silyl group binding to the remaining surface, and iii) X-ray scattering (XRS)-mediated detection of peak shifts of a biological substrate, *Escherichia coli* (*E. coli*), as a function of applied magnetic field strength and magnetic nanoparticle concentration in a cell growth medium.

In a study of MNP surface modification, quantitative evaluation of anti-mouse IgG binding on MNPs and bioactivity on MNPs was conducted via fluorescence assays. Nanosize γ -Fe₂O₃ particles were hybridized with anti-mouse IgG via silane chemistry with 3-aminopropyltriethoxy silane and glutaraldehyde activation. A chemisorption isotherm via fluorescence assays demonstrated that immobilization of anti-mouse IgG can be stoichiometrically controlled with the surface coverage at saturation corresponding to 36% of the theoretical limit. The immobilized anti-IgG retains ~50% of its bioactivity at saturation.

Differential functionalization of SiO₂/TiO₂ mixed nanoparticles was demonstrated via aqueous-phase preferential binding of phosphonic acids to TiO₂ and subsequent binding of trimethyl silyl group to the remaining surface. SiO₂/TiO₂ mixed nanoparticles with three different mole ratios of Si/Ti together with pure SiO₂ and TiO₂ nanoparticles were used in comparative XPS study of differential functionalization. Differential functionalization of metal oxide-metal oxide mixed nanoparticles demonstrated herein adds a route to multifunctional nanoparticles.

An *In situ* XRS study of *E. coli* in applied magnetic fields up to 423 mT was performed. Two peaks, a sharp peak at $q = 0.528 \text{ \AA}^{-1}$ (1.189 nm) and a diffuse peak at $q = 0.612 \text{ \AA}^{-1}$ (1.027 nm), were detected in XRS of MNP-absent *E. coli* culture. The presence of SiO₂/ γ -Fe₂O₃ MNPs at 40 mg/L in *E. coli* growth medium changes the sharp peak to the lower side of q as a function of applied magnetic field strength, while the position of the diffuse peak is invariable. 362 mT was found to be a critical magnetic field strength, at which the sharp peak disappears. This study demonstrates magnetic field-assisted interactions between *E. coli* cell membranes and MNPs.

FUNCTIONALIZATION OF NANOPARTICLES
FOR BIOLOGICAL APPLICATIONS

By

Isaac Koh.

Dissertation submitted to the Faculty of the Graduate School of the
University of Maryland, College Park, in partial fulfillment
of the requirements for the degree of
Doctor of Philosophy
2005

Advisory Committee:

Professor Sheryl H. Ehrman, Chair

Professor Luz J. Martínez-Miranda

Professor Douglas S. English

Professor Srinivasa R. Raghavan

Professor John P. Fisher

© Copyright by

Isaac Koh

2005

Dedication

To my loving parents, Kwang-Ok Koh and Kye-Ja Jung,
my sons, David and Paul,
and my wife, Soona

Acknowledgements

First of all, my sincere gratitude is directed toward my advisor, Dr. Sheryl Ehrman, for her dedicated discipline and guidance for me to stand as an independent researcher. I am indebted to my co-advisors, Dr. Douglas English, Dr. Lyle Isaacs, and Dr. Luz Martínez-Miranda, for their invaluable advices during my Ph. D years. I am grateful to Dr. Srinivasa Raghavan and Dr. John Fisher for their service as my committee members. I am thankful to Dr. Tracey Pulliam Holoman for her advice during the early years of my Ph. D studies.

The group members of Dr. Ehrman, Dr. English, Dr. Isaacs, and Dr. Martínez-Miranda have been very helpful. Specifically, I am thankful to Dr. Ranjan Pati, Jason Repac, and Bani Cipriano for particle synthesis, Xiang Wang for confocal microscopy study, Dr. Darryl Williams and Seonmin Kim for TEM images, Oluwatosin Ogunsola for BET measurement, and Jason Lagona for discussion about FTIR and fluorescence spectroscopy study. I appreciate assistance from Dr. Bindhu Varughese in X-ray photoelectron spectroscopy study and from Tim Mangel in taking TEM and SEM images. I am thankful to Ben Woodard, the Bio Scale-up Facility manager, and Dr. Nam Sun Wang for kindly allowing me to use their facilities. I appreciate financial support from the Materials Research Science and Engineering Center in University of Maryland and the Defense Advanced Research Projects Agency-the Office of Naval Research.

Personally, I am thankful to my church members including Jacob and Esther Lee, Dr. Luke and Rebekah Lim, Elijah and Grace Park, Moses and Sarah Chang, David and Sarah Yun, Haejin Kim, and Anthony and Grace Mokre for their love and

fellowship. I am grateful for the friendship I have enjoyed with colleagues in the department of Chemical and Biomolecular Engineering including Dr. Wook Chang, Dr. Young Soon Um, Chi-Wei Hung, Dr. Hyunmin Yi, Jaeho Lee, Joongjin Han, Seonmin Kim, Heeyoung Lee, and Yuesheng Ye. I appreciate the fine education I have received from the faculty members of the department of Chemical and Biomolecular Engineering. I am especially thankful to Dr. Kyu Yong Choi for his care.

I bow in deep respect and appreciation to my parents, and my parents-in-law for their love and support. I am sincerely thankful for love and support from my sisters, my sisters-in-law, my aunt-in-law, and other family members.

My wife, Soona, deserves much credit for her love, support, and prayer for me. David and Paul, my sons, are a source of joy to me.

Table of Contents

Dedication.....	ii
Acknowledgements.....	iii
List of Tables	vii
List of Figures and Schemes.....	viii
Chapter 1: Introduction.....	1
1.1 Motivation.....	1
1.2 Objectives	2
1.3 Overview.....	3
Chapter 2: Background	6
2.1 Abstract.....	6
2.2 Introduction.....	6
2.3 Generation of metal oxide nanoparticles	8
2.3.1 Synthesis in solution	8
2.3.2 Synthesis via aerosol methods	14
2.4 Surface modification of metal oxide nanoparticles	18
2.4.1 Silanes.....	18
2.4.2 Carboxylic acids.....	23
2.4.3 Phosphorous compounds	24
2.4.4 Diols.....	25
2.5 Multifunctional metal oxide nanoparticles and nanocomposites.....	27
2.6 Cellular membranes and X-ray scattering.....	32
2.6.1 <i>E.coli</i> cellular membrane	32
2.6.2 X-ray scattering.....	33
Chapter 3: Magnetic iron oxide nanoparticles for bio-recognition: Evaluation of surface coverage and activity	35
3.1 Abstract.....	35
3.2 Introduction.....	35
3.3 Experimental methods	39
3.3.1 Materials	39
3.3.2 APTES modification of magnetic iron oxide nanoparticles	39
3.3.3 Preparation of antibody-coated iron oxide nanoparticles through crosslinking with glutaraldehyde	40
3.3.4 Dye-labeling of target antibody	41
3.3.5 Magnetic immobilization of target antibody (mouse IgG) using the anti- mouse IgG modified MNPs	42
3.3.6 Fluorescence microscopy and spectroscopy	42

3.3.7 X-ray photoelectron spectroscopy	43
3.3.7 Transmission Electron Microscopy (TEM)	44
3.4 Results and Discussion	44
3.5 Conclusion	55
3.5 Conclusion	56
Chapter 4: Differential functionalization of SiO ₂ /TiO ₂ mixed nanoparticles: an X-ray photoelectron spectroscopy study	57
4.1 Abstract	57
4.2 Introduction	58
4.3 Materials and methods	60
4.4 Results and discussion	63
4.5 Conclusions	81
Chapter 5: X-ray scattering study of the interactions between magnetic nanoparticles and living cell membranes	83
5.1 Abstract	83
5.2 Introduction	84
5.3 Methods	85
5.3.1 Magnetic nanoparticles	85
5.3.2 Biological system	88
5.3.3 X-ray scattering system	89
5.3.4 Transmission electron microscope (TEM) images	92
5.4 Results and Discussion	92
5.4 Conclusions	99
Chapter 6: Conclusions and recommendations	101
6.1 Conclusions	101
6.2 Recommendations	103
Appendices	114
References	173

List of Tables

Table 2.1 Ligands and the functionalized surfaces.	19
Table 4.1 Effect of solvent (toluene) in the BSTFA reaction step: atomic concentration (%).	78
Table 5.1 Peak positions as a function of the presence of the particles and applied magnetic field strengths.	96
Table A.1 Maximum absorbance/emission wavelength of dyes.	123
Table A.2 Surface coverage of MNPs as a function of the anti-IgG orientation.	133
Table C.1 Medium composition of three types of M9 media used in XRS studies.	161
Table C.2 Peak positions of XRS data of M9 medium type I as a function of magnetic field strength and MNP concentration.	163
Table C.3 Peak positions of XRS data of M9 medium type II as a function of magnetic field strength and MNP concentration.	166
Table C.4 Peak positions of XRS data of M9 medium type III as a function of magnetic field strength and MNP concentration.	168

List of Figures and Schemes

Figure 2.1 Strategies to attach Au or Ag nanoparticles on metal oxide nanoparticles.	12
Figure 2.2 Mole ratio-dependent morphologies of flame-synthesized SiO ₂ /metal oxide mixed nanoparticles: (a) SiO ₂ /TiO ₂ , (b) SiO ₂ /Fe ₂ O ₃ .	17
Figure 2.3 Schematic diagram of surface modification of Fe ₃ O ₄ nanoparticles for MRI.	21
Figure 2.4 Schemes of silane chemistry on iron oxide nanoparticles.	22
Figure 2.5 Differential functionalizations of SiO ₂ /TiO ₂ surfaces.	31
Figure 2.6 Electron micrograph of a gram negative cell wall.	32
Figure 2.7 Fluid mosaic model of a cell membrane.	34
Scheme 3.1 (a) Surface modification of γ -Fe ₂ O ₃ nanoparticles with APTES for the immobilization of fluorescein-labeled anti-mouse IgG (FL-anti-mouse IgG). (b) Separation of Alexa Fluor 568-labeled mouse IgG (AF-mouse IgG) using the anti-mouse IgG antibody coated MNPs.	38
Figure 3.1 XPS spectra of γ -Fe ₂ O ₃ nanoparticles.	46
Figure 3.2 Adsorption isotherm of fluorescein-labeled anti-mouse IgG antibody on γ -Fe ₂ O ₃ nanoparticles.	47
Figure 3.3 Fluorescence analysis of magnetic separations performed on mouse IgG.	51
Figure 3.4 Spectra of spin-coated MNPs excited with 488 nm Ar-ion laser.	55
Scheme 4.1 Scheme of the proposed differential functionalization of SiO ₂ , TiO ₂ , and SiO ₂ /TiO ₂ mixed nanoparticles.	61
Figure 4.1 (a) Morphologies of SiO ₂ , TiO ₂ , and SiO ₂ /TiO ₂ mixed nanoparticles used in this work. (b) TEM of SiO ₂ /TiO ₂ (Si:Ti = 1:1) mixed nanoparticles.	64

Figure 4.2	TEM of SiO ₂ /TiO ₂ nanocomposites at different ratios of Si and Ti.	65
Figure 4.3	Atomic concentration (%) of (a) Si and (b) Ti, and (c) the ratio of Ti versus Si atomic concentration in the XPS data of SiO ₂ , and SiO ₂ /TiO ₂ mixed nanoparticles.	66
Figure 4.4	Phosphorous 2p region of XPS scan of (a) SiO ₂ nanoparticles, (b)-(d) SiO ₂ /TiO ₂ mixed nanoparticles, and (e) TiO ₂ nanoparticles.	68
Scheme 4.2	Schematic representation of surface modification of TiO ₂ nanoparticles with (a) BSTFA and (b) PPA.	71
Scheme 4.3	Schematic representation of surface modification of SiO ₂ nanoparticles with (a) BSTFA and (b) PPA.	72
Figure 4.5	Ti 2p XPS spectra of (a) bare unreacted TiO ₂ , (b) BSTFA-reacted TiO ₂ , and (c) PPA-reacted TiO ₂ nanoparticles.	73
Figure 4.6	(a) Atomic concentration (%) of phosphorous 2p (P 2p) peaks and (b) the ratio of atomic concentration of P peaks versus atomic concentration of Ti peaks.	74
Figure 4.7	(a) Atomic concentration (%) of carbon 1s (C 1s) peaks and (b) the atomic concentration ratio of C 1s peaks versus (Si 2p + Ti 2p) peaks.	75
Scheme 4.4	Formation of phenyl-P(OTi) ₂ (OSi) bonds at the interface of TiO ₂ and SiO ₂ portion of SiO ₂ /TiO ₂ mixed nanoparticles.	76
Figure 4.8	Ti 2p spectra of SiO ₂ /TiO ₂ mixed nanoparticles. Si:Ti = 5:1 (A), 1:1 (B), and 1:5 (C).	80
Figure 5.1	Transmission electron microscope image of a SiO ₂ /γ-Fe ₂ O ₃ particle.	86
Figure 5.2	(a) Distribution of particle sizes as measured using TEM. (b) Agglomeration of the particles as a function of time in the M9 medium.	87
Figure 5.3	A schematic diagram of (a) the continuous culture of <i>E. coli</i> and (b) the <i>in situ</i> x-ray scattering.	89

Figure 5.4 Magnetic field strength as a function of the distance between the two magnets.	91
Figure 5.5 <i>In situ</i> X-ray scattering results from <i>E. coli</i> continuous cultures.	94
Figure 5.6 Peak position as a function of the applied magnetic field strength.	97
Figure 5.7 Transmission electron micrograph images showing that <i>E. coli</i> have contacts with the SiO ₂ /γ-Fe ₂ O ₃ particles.	98
Figure 6.1 Proposed reactions to build multifunctional magnetic nanoparticles for MR imaging.	105
Figure 6.2 Suggested scheme of differential functionalization.	107
Figure 6.3 Methodologies to attach noble metal nanoparticles only to TiO ₂ surfaces of SiO ₂ /TiO ₂ nanoparticles.	108
Figure 6.4 Selective binding of Au nanoparticles to the SiO ₂ portion of SiO ₂ /TiO ₂ mixed nanoparticles. PPA: phenyl phosphonic acid.	110
Figure 6.5 Asymmetric binding of two different size-Au nanoparticles to SiO ₂ /TiO ₂ mixed nanoparticles.	111
Figure 6.6 Synthesis of Au- SiO ₂ /Fe ₂ O ₃ dimers via a nanoparticle assembly at a liquid-liquid interface.	112
Figure A.1 Standard calibration curve of fluorescein-labeled anti-mouse IgG.	128
Figure A.2 Washing effect of MNPs treated with fluorescein-labeled anti-mouse IgG.	129
Figure A.3 A schematic configuration of anti-IgG binding on the MNP surface.	132
Figure A.4 Transmission electron microscopy images for bare γ-Fe ₂ O ₃ nanoparticles.	135
Figure A.5 Particle size distribution of bare γ-Fe ₂ O ₃ nanoparticles.	136
Figure C.1 Growth curve of <i>E. coli</i> in M9 medium in a batch culture.	148
Figure C.2 Specific growth rate as a function of the <i>E. coli</i> culture time.	149

Figure C.3 Derivation of Bragg's law for X-ray scattering.	150
Figure C.4 Comparison of growth curves of <i>E. coli</i> in batch cultures in LB medium.	158
Figure C.5 Comparison of growth curves of <i>E. coli</i> in batch cultures in LB medium.	159
Figure C.6 XRS data of M9 medium type I as a function of MNP concentration up to 100 mg/L.	162
Figure C.7 XRS data of M9 medium type II as a function of MNP concentration up to 100 mg/L.	165
Figure C.8 XRS data of M9 medium type III as a function of MNP concentration up to 100 mg/L.	167
Figure C.9 d spacing (Å) as a function of applied magnetic field strengths at different MNP concentrations.	171
Figure C.10 d spacing (Å) as a function of MNP concentration in the applied magnetic field strength of 0 and 362 mT.	172

Chapter 1: Introduction

1.1 Motivation

Nanosize metal oxide particles have emerged as versatile tools for biological applications due to their magnetic, electronic, photonic and optical properties. Surface modification of metal oxide nanoparticles adds to the usefulness of the nanoparticles on top of their intrinsic characteristics, since hybridization of functional molecules on the nanoparticles provides target-specific recognition, catalytic abilities, and controlled surface properties such as hydrophobicity. Assemblies of metal oxide nanoparticles and biomolecules such as antibodies, enzymes, and streptavidin via surface modification of the nanoparticles have drawn a growing interest in the areas of bioanalysis and fabrication of bioelectronic devices.^{1,2} A quantitative evaluation of biomolecule hybridization with nanoparticles is desired, since it will lead to a better control of nanoparticle-biomolecule assemblies.

Multifunctional nanoparticles have promising potential in biological applications, especially in cancer-specific applications as drug carriers and imaging agents, because they multitask, overcoming biological barriers, targeting specific cancer cells and delivering drugs.³ Multiplexed nanoparticles such as metal-metal^{4,5} and metal-metal oxide³ nanocomposites have been applied as multifunctional nanoparticles via differential surface modification. Differential surface modifications of SiO₂-TiO₂ surfaces,⁶⁻⁸ via the preferential binding of phosphonates to TiO₂ and subsequent binding of poly(L-lysine)-g-poly(ethylene glycol) or trimethyl silyl

groups (-OSi-(CH₃)₃) to SiO₂, open the possibility to develop multifunctionality on SiO₂/TiO₂ mixed nanoparticles⁹ synthesized in our group.

The ever increasing number of biological applications of metal oxide nanoparticles, especially magnetic iron oxide nanoparticles, requires a better understanding of the interactions between biological cells and nanoparticles. X-ray scattering (XRS) provides a useful tool for detection of the interactions between cellular membranes and magnetic nanoparticles, since XRS has been employed in measurement of layer separation of biomimetic phospholipid layers.¹⁰

1.2 Objectives

This research is aimed at biological applications of metal oxide nanoparticles, specifically γ -Fe₂O₃ nanoparticles and SiO₂/TiO₂ and SiO₂/ γ -Fe₂O₃ mixed nanoparticles. Surface modification of the metal oxide nanoparticles via silane chemistry plays a crucial role in hybridizing anti-mouse IgG on γ -Fe₂O₃ nanoparticles. A quantitative evaluation of surface coverage and bioactivity of the γ -Fe₂O₃ nanoparticle-anti-mouse IgG assembly is provided via fluorescence characterization of the dye-labeled anti-mouse IgG. Differential functionalization of SiO₂/TiO₂ mixed nanoparticles is achieved via preferential binding of phosphonic acids on TiO₂ and subsequent reaction with a mild silylating reagent. Various characterization methods including X-ray photoelectron spectroscopy, Fourier transform infrared spectroscopy, fluorescence spectroscopy, and fluorometer measurement of emission from dye-labeled antibodies along with electron microscopy are used to characterize the particle surfaces before and after surface modifications. XRS is used to detect the

interactions between *E. coli* cellular membranes and SiO₂/ γ -Fe₂O₃ mixed nanoparticles as a function of applied magnetic field strength, concentrations of the magnetic mixed nanoparticles and divalent ions in the cell growth medium.

1.3 Overview

An overview of each chapter is presented as follows:

Chapter 2–Background

This chapter contains a literature review of the following three topics: i) generation of nanosize Fe₃O₄, Fe₂O₃, SiO₂, and TiO₂ particles and their nanocomposites such as Fe₃O₄-Au (or Ag) and SiO₂-Fe₂O₃ composite particles via solution methods and aerosol synthesis, ii) ligands used to modify the surface of the metal oxide nanoparticles, and iii) *E. coli* cell membranes and X-ray scattering. The section on solution phase synthesis of metal oxide nanoparticles and nanocomposites describes recent advances in the synthesis of the nanoparticles including iron oxide, titania, silica and metal oxide-noble metal composites. The aerosol synthesis portion focuses mainly on the generation of metal oxide-metal oxide nanocomposites such as SiO₂/TiO₂ and SiO₂/Fe₂O₃ composite nanoparticles. Ligands used for surface modification of the metal oxide nanoparticles are reviewed including silanes, carboxylates, and diols. Differential modifications of SiO₂-TiO₂ mixed surfaces are described focusing on the preferential binding of phosphonates to TiO₂ surfaces. The last part of this chapter is allotted for a brief description of *E. coli* cell membrane structures and X-ray scattering as a detection method of crystalline structures.

Chapter 3- *Magnetic iron oxide nanoparticles for bio-recognition: Evaluation of surface coverage and activity*

This chapter describes a quantitative evaluation of anti-mouse IgG binding on γ -Fe₂O₃ nanoparticles via silane chemistry and glutaraldehyde activation. A quantitative understanding of the anti-mouse IgG coverage of the magnetic nanoparticles (MNPs) and the bio-activity of the immobilized anti-mouse IgG is provided via measurements of fluorescence spectra of the dye-labeled anti-mouse IgGs and mouse IgGs. The results demonstrate that loading of anti-IgG on the MNPs can be stoichiometrically adjusted with ~36% saturated surface coverage of the theoretical limit and the immobilized anti-IgG retains ~50% of its bioactivity at saturation.

Chapter 4- *Differential functionalization of SiO₂/TiO₂ mixed nanoparticles: an X-ray photoelectron spectroscopy study*

This chapter describes differential functionalization of aerosol-phase synthesized SiO₂/TiO₂ mixed nanoparticles. Differential functionalization of the mixed metal oxide-metal oxide nanoparticles is achieved via preferential binding of phosphonic acids to TiO₂ in aqueous solution and subsequent trimethyl silyl group-binding to the remaining SiO₂ surface. An X-ray photoelectron spectroscopy study demonstrates the preferential binding of phenyl phosphonic acids to TiO₂ of the mixed nanoparticles and ~80% retention of bound phenyl phosphonic acid following

trimethyl silyl group binding to SiO₂. Binding characteristics as a function of different mole ratios of Si to Ti are discussed.

Chapter 5- *X-ray scattering study of the interactions between magnetic nanoparticles and living cell membranes*

This chapter describes an X-ray scattering (XRS) study of the interactions between *E. coli* cell membranes and magnetic SiO₂/γ-Fe₂O₃ mixed nanoparticles in magnetic fields. *In situ* X-ray scattering study of *E. coli* in the presence of magnetic fields up to 423 mT displays two peaks, a sharp peak at $q = 0.528 \text{ \AA}^{-1}$ (1.189 nm) and a diffuse peak at $q = 0.612 \text{ \AA}^{-1}$ (1.027 nm). Addition of SiO₂/γ-Fe₂O₃ mixed nanoparticles at a concentration of 40 mg/l of growth medium changes the sharp peak to the lower side of q , while the position of the diffuse peak is invariable. 362 mT is found to be a critical magnetic field strength, where the sharp peak disappears.

Chapter 6-*Conclusions and recommendations*

This chapter contains conclusions and recommendations for future studies. Surface modification of metal oxide nanoparticles, especially iron oxide nanoparticles and SiO₂/TiO₂ mixed nanoparticles, is summarized. *In situ* XRS study of *E. coli* is also summarized as a function of applied magnetic field strength up to 423 mT, and added SiO₂/γ-Fe₂O₃ mixed nanoparticles. Based on the summarized results, recommendations for future studies are presented.

Chapter 2: Background

2.1 Abstract

This chapter contains a literature review of synthesis and applications of nanosize metal oxide particles, focusing especially on Fe_2O_3 , Fe_3O_4 , TiO_2 , SiO_2 and their nanocomposites. A brief overview is presented of the synthesis of these metal oxide nanoparticles via solution phase and aerosol methods. Several functional compounds are discussed, focusing on their metal oxide-surface modification capabilities for biological, medicinal, and catalytic applications. Multiplexed nanoparticles, such as metal oxide-metal and metal oxide-metal oxide nanocomposites that demonstrate potential for utilization as multifunctional nanoparticles via differential surface modifications, are described. Cell membrane structures along with X-ray scattering as a detection method for the d-spacing of a crystalline structure are briefly described at the end of the chapter.

2.2 Introduction

Nanosize metal oxide particles, especially Fe_2O_3 , Fe_3O_4 , TiO_2 and SiO_2 , have been of intense interest due to their characteristic features such as electric, optical, magnetic, photo-sensitive properties. In addition to their inherent characteristics, their amenability for surface modification has led to a great extension of their utilization in biological, medicinal and environmental applications. Readily-available

functional groups including silanes, carboxylates, and diols have demonstrated capabilities for surface modification of these metal oxide nanoparticles. Functional surface modifications of metal oxide nanoparticles have provided a number of tools for a construction of metal oxide nanoparticle-biomolecule hybrid systems, for example, iron oxide nanoparticle-antibody conjugates.¹

There is a great need for multifunctional nanoparticles in the areas such as magnetic resonance imaging (MRI), drug delivery and sensitive detection of pathogens.¹¹ Multifunctional metal oxide nanoparticles have been constructed via the fabrications of metal oxide-metal^{3, 12} and metal oxide-metal oxide nanocomposites.⁶ Differential surface modifications of metal oxide-metal oxide surfaces⁶⁻⁸ suggest the potential for the development of multifunctional metal oxide/metal oxide composite nanoparticles.

There is also a need for the investigation of the interactions between biological cell membranes and metal oxide nanoparticles for the purpose of enhancing understanding of the mechanisms of transport and for understanding chemical/physical interactions of the nanoparticles with cell membranes as drug carriers and cancer-treatment agents. X-ray scattering is a useful tool for the detection of the interactions.¹³

This chapter is composed of the following sections: i) synthesis of Fe₂O₃, Fe₃O₄, TiO₂ and SiO₂ nanoparticles and their nanocomposites via solution phase and aerosol methods, ii) an overview of ligands for the surface modification of the metal oxide nanoparticles, iii) multifunctional metal oxide nanoparticles, focusing on metal oxide-metal oxide surfaces, and iv) *E. coli* cell membranes and X-ray scattering.

2.3 Generation of metal oxide nanoparticles

2.3.1 Synthesis in solution

Iron oxide nanoparticles: Iron oxide nanoparticles have attracted much interest due to their useful characteristics including magnetic properties, biocompatibility and availability for surface modification.

In the early 1980s, Massart developed a co-precipitation method of ferrous and ferric salts in alkaline and acidic aqueous phase to prepare Fe_3O_4 nanoparticles in the size range of 10-20 nm.¹⁴ The co-precipitation method has been used in many applications¹⁵⁻²¹ and also has been followed by efforts to improve the polydispersity by size fractionation after the co-precipitation step²²⁻²⁴. Synthesis of monodisperse (standard deviation in size < 5%) iron oxide nanoparticles is highly desired in applications such as magnetic resonance imaging to enhance imaging capability.^{25, 26}

Recently, high-temperature decomposition of organic precursors led to the synthesis of monodisperse iron oxide nanoparticles. Hyeon and collaborators²⁷ reported the synthesis of monodisperse $\gamma\text{-Fe}_2\text{O}_3$ nanoparticles with average diameters from 4 to 16 nm as a result of a careful control of the molar ratio of metal precursor to surfactant, $\text{Fe}(\text{CO})_5$ and oleic acid respectively. Amorphous monodisperse iron nanoparticles were first formed in their process and then were oxidized to nanocrystalline $\gamma\text{-Fe}_2\text{O}_3$ particles with a mild oxidant, trimethylamine oxide. They further modified the methodology, thermolysis of the iron-oleate complex, as a source for ultra-large-scale synthesis of monodisperse nanocrystalline iron oxide particles, 40 g in a batch.²⁸ They were able to substitute the toxic and expensive organometallic compound, $\text{Fe}(\text{CO})_5$, with an environmentally benign and cost-effective reagent,

$\text{FeCl}_3 \cdot 6\text{H}_2\text{O}$, in the metal-surfactant complex formation step. They also investigated the mechanism of the nanocrystalline synthesis through analysis using transmission electron microscopy, infrared spectroscopy, thermogravimetric analysis, and differential scanning calorimetry. According to their analysis results, the difference in temperature dependence between the rates of nucleation and particle growth is a key factor in synthesizing the monodisperse nanocrystalline metal oxides. Sun and Zeng²⁹ reported the synthesis of magnetite (Fe_3O_4) nanoparticles in high-temperature (265°C) treatment of iron (III) acetylacetonate in phenyl ether in the presence of alcohol, oleic acid, and oleylamine. 4 nm size magnetite particles were synthesized in this process and larger magnetite particles up to 20 nm in diameter were made through a seed-mediated growth method. In this approach, additional precursors are added to the 4 nm magnetite particles.

The facile synthesis of monodisperse maghemite (Fe_2O_3) and magnetite nanoparticles via the methods including those mentioned above has led to an active application of the magnetic nanocrystallites in biological and medicinal areas through surface modification and fabrication of the nanoparticles.

Silica nanoparticles: The Stöber process has typically been used to prepare spherical silica particles.³⁰ The Stöber process involves hydrolysis of an alkoxy silane such as alkoxide tetraethoxysilane (TEOS) and silanol-condensation. Silica-coatings in Fe_2O_3 core/shell structures have also been prepared using the Stöber process.³¹ In addition to the synthesis of spherical silica nanoparticles, Martin and collaborators³² have demonstrated template-based synthesis of silica nanotubes.

Titania nanoparticles: TiO₂ is a well-known and widely-used semiconductor material because of its photocatalytic property. TiO₂ has three phases: thermodynamically stable rutile, metastable anatase, and brookite. Generally, anatase phase is found in crystalline TiO₂ synthesized by the sol-gel and aerosol methods. Several preparation methods of TiO₂ nanoparticles are available in the literature. For example, hydrolysis of titanium (IV) alkoxides in aqueous and alcohol solvent led to TiO₂ nanoparticles of three different sizes and phases: 0.7 nm (amorphous), 0.8-1.4 nm (polycrystal-like), and 6.0 nm (polycrystal).³³ Rajh and collaborators have synthesized nanocrystalline TiO₂ in two steps: (i) dropwise addition of titanium (IV) chloride to cooled water, (ii) slow growth of the particles by dialysis until pH 3.5 was reached in the solution.^{34, 35} The synthesized TiO₂ nanoparticles were 4.3 ± 0.4 nm in diameter. Cozzoli *et al.*³⁶ reported the synthesis of TiO₂ nanocrystals by low-temperature (80-100 °C) hydrolysis of titanium (IV) alkoxide in the presence of oleic acid as surfactant.

Metal oxide-metal nanocomposites: Recent progress in the synthesis of metal-metal or metal oxide-metal composite nanoparticles has been reported.^{3, 12, 37-39} Figure 2.1 summarizes the schemes for the attachment of Au (or Ag) nanoparticles on metal oxide nanoparticles.

Metal oxide/Au (or Ag) nanocomposites were fabricated in several ways. Halas and collaborators have reported an application of the affinity between Au and the amine functional group to the fabrication of silica-gold nanoshells with tunable

optical properties.⁴⁰⁻⁴² Gold nanoparticles were attached on amine groups of APTES-modified silica core nanoparticles and a gold shell was grown along the attached Au nanoparticles in a subsequent treatment of HAuCl₄. The plasmonic characteristic of the dielectric silica core-gold shell structures was effective in inducing a thermal damage on carcinoma cells. This approach was followed in the preparation of Fe₃O₄-Au nanocomposites.⁴³

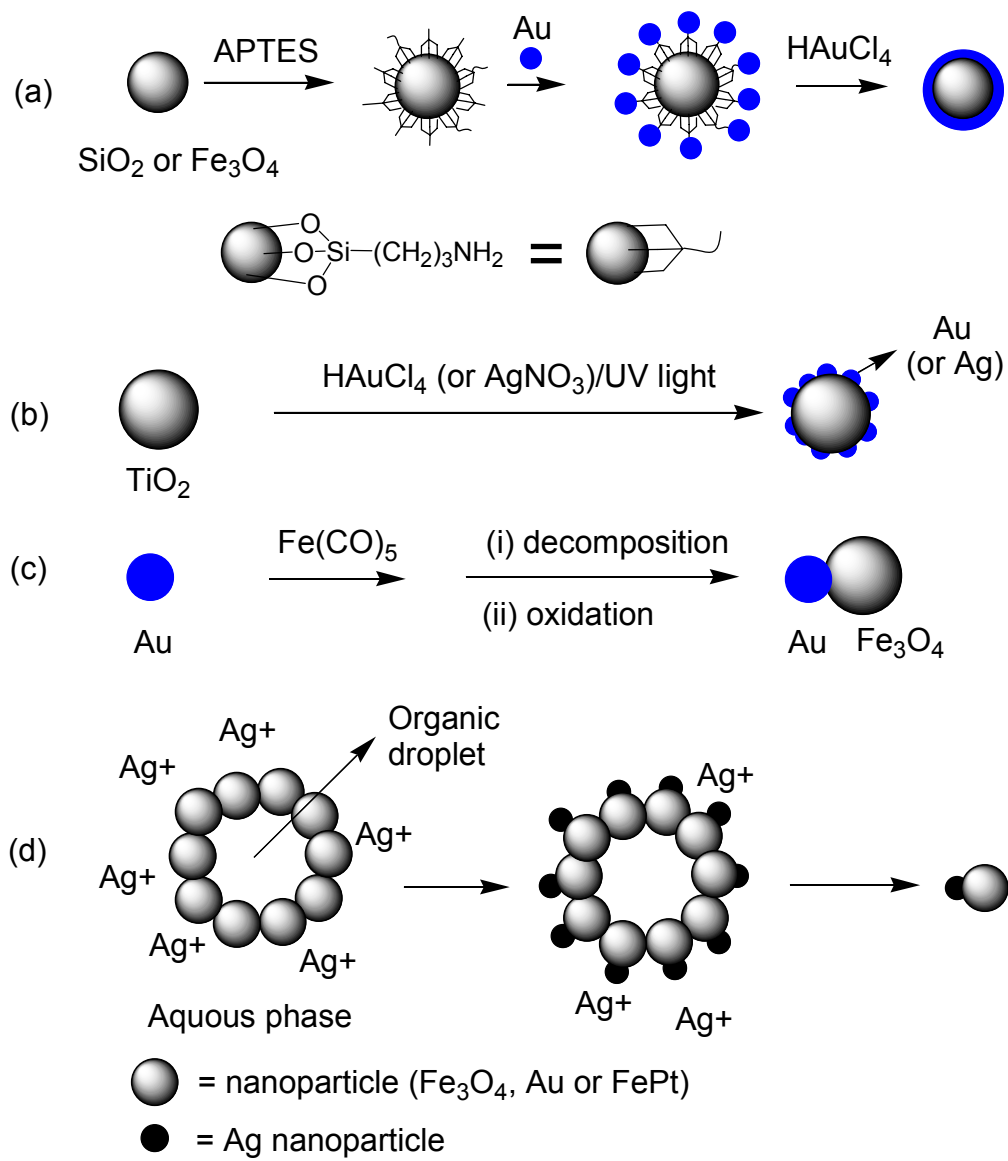


Figure 2.1 Strategies to attach Au or Ag nanoparticles on metal oxide nanoparticles.

Recent efforts have been directed to the development of heterodimeric iron oxide-metal nanocomposites. The heterodimeric nanoparticles were synthesized in the following ways: i) metal oxide nanoparticle assembly at liquid-liquid interfaces and deposition and growth of Au (or Ag) on the metal oxide nanoparticles,³ ii) decomposition and oxidation of metal oxide precursor on the surface of Au nanoparticles.¹² Xu and collaborators used nanoparticle assembly at a liquid-liquid interface to form heterodimeric nanoparticles, for example Fe₃O₄-Ag.³ Ag nanoparticles were seeded and grown on the surface of Fe₃O₄ nanoparticles (d= 8 nm) assembled at the interface between organic droplets and an aqueous phase (Figure 2.1(d)). Sun and collaborators¹² also prepared heterodimeric Fe₃O₄-Au nanoparticles by high-temperature decomposition (> 450 °C) of iron pentacarbonyl on Au nanoparticles and oxidation in air. These methods yielded heterodimers below 20 nm in diameter. Other preparation methods of metal oxide-Au composites led to the formation of composite particles over 100 nm in diameter.^{37, 38}

The well-known photocatalytic activity of TiO₂ has led the semiconductor to be a material of intense study in the area of environmental treatment such as degradation of organic contaminants in wastewater and air.⁴⁴ Deposition of Au (or Ag) on TiO₂ nanostructures leads to increased photocatalytic activity and photoelectrochemical response due to the coupling between the noble metal and the semiconductor oxide. The increased photoelectrochemical response results in reduced recombination of photogenerated charges. Ag nanoparticles generated in a nanoporous TiO₂ film under UV light exhibited reversible photochromatic behavior.^{45,}
⁴⁶ The noble metal-TiO₂ composite nanostructures have been generally prepared with

the following methods: (i) photoelectrochemical deposition of Ag or Au nanoparticle on TiO₂ nanostructures,⁴⁵⁻⁴⁹ (ii) chemical reduction of precursor materials, HAuCl₄ or AgNO₃, on TiO₂ nanoparticles.⁵⁰

2.3.2 Synthesis via aerosol methods

Flame aerosol synthesis of oxide powders have typically been employed commercially in large-scale production of titania pigment and fumed silica additive.^{51, 52} Flame processes have been effective in the synthesis of oxide-oxide composite particles^{9, 53-57} as well as single component oxide particles⁵⁸⁻⁶¹.

In the 1980s, Chung and Katz⁵⁹ developed the counterflow diffusion flame burner to synthesize refractory oxides such as SiO₂, Al₂O₃, and Fe₂O₃ in H₂/O₂ flame. Zachariah *et al.*⁵⁸ investigated this counterflow geometry to see the effects of process variables such as precursor loading and flame temperatures on particle formation. Their results illustrated that flame temperatures were a key factor in particle morphology because of particle morphology dependence on chemical kinetic rates. In the late 1990s, Pratsinis and collaborators⁶⁰ examined the effect of silicon precursors, organosilane compounds vs. SiCl₄, on specific surface areas of the generated SiO₂ particles in a diffusion flame reactor. A smaller specific surface area of organosilane-derived SiO₂ was attributed to the increase of the flame temperature involved with the additional combustion source from the organosilane precursors. Recently, Pratsinis and collaborators⁶¹ employed a premixed methane-oxygen flame to synthesize TiO₂ nanoparticles from titanium tetraisopropoxide precursor and investigated various particle formation pathways by monitoring sampled particle

morphologies and flame temperatures. Surface reaction was found to contribute to early particle growth in their reaction conditions.

Mixed oxide powders are useful in industry in the area of ceramics, optical fibers, catalysts, and paint opacifiers.⁵⁴ In early 1990s, Katz and collaborators demonstrated the flame synthesis of various metal oxide powders such as TiO₂/SiO₂, SiO₂/GeO₂, Al₂O₃/TiO₂, V₂O₅/TiO₂, and V₂O₅/Al₂O₃.⁵³⁻⁵⁵ Recently, Zachariah and collaborators^{62, 63} demonstrated aerosol-based sol-gel synthesis of nanoporous iron oxide and silica particles. They also presented a method to coat an iron oxide layer on a strong oxidizer nanoparticle (potassium permanganate; ~150 nm).⁶⁴ Serna and collaborators⁶⁵ exhibited the direct synthesis of silica-coated γ -Fe₂O₃ hollow spherical particles (150 ± 100 nm) via the aerosol pyrolysis of precursors, iron ammonium citrate and TEOS dissolved in methanol.

SiO₂/TiO₂ mixed nanoparticles have drawn a high level of interest because of an enhanced reactivity coming from a combined effect of photocatalytic activity of TiO₂ and high absorption capability of SiO₂.⁶⁶ Since the early 1990s-report of the counterflow diffusion flame-synthesis of TiO₂/SiO₂ composites by Hung and Katz,⁵⁴ active studies on the aerosol-mediated formation of the mixed oxides and their catalytic activities have been reported.^{9, 56, 57, 66-71} For example, Ehrman *et al.*^{9, 56} demonstrated the synthesis of SiO₂/TiO₂ and SiO₂/Fe₂O₃ mixed nanoparticles (diameter < 100 nm) in an aerosol flame reactor. High-temperature aerosol reactions (> 2300 K) led to a single-step generation of large amounts of the mixed nanoparticles. They employed various mole ratio of the precursors, C₆H₁₈OSi₂ versus TiCl₄ or Fe(CO)₅, to produce the phase-segregated nanoparticles with different

morphologies (Figure 2.2). X-ray diffraction results along with transmission electron micrographs, electron energy loss spectra, and Fourier transform spectra illustrated the mole ratio-dependent distribution of the species.

Theoretical studies have gained attention because of interest in achieving control of flame reactors. Particle morphology of materials made by flame aerosol synthesis is a strong function of temperature and residence time. Modeling and simulation studies^{61, 72-76} have been published relating particle morphology to measured process control parameters such as flame temperature, cooling rate, and precursor concentration. A number of monitoring methods have been used including laser scattering,⁷⁷ dynamic light scattering and thermophoretic sampling,⁵⁴ particle mass spectrometry,⁷⁸ Fourier transform infrared spectroscopy,⁹ and computer imaging analysis of transmission electron micrographs.⁷⁹

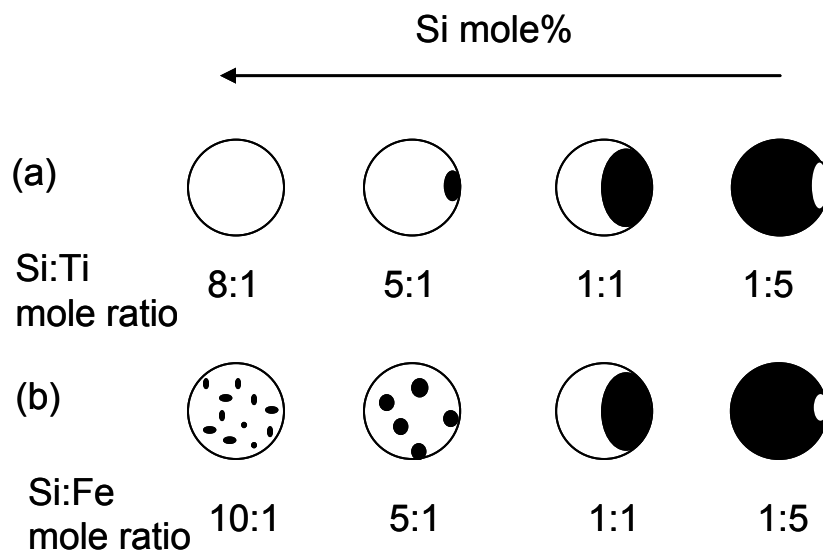


Figure 2.2 Mole ratio-dependent morphologies of flame-synthesized SiO₂/metal oxide mixed nanoparticles: (a) SiO₂/TiO₂, (b) SiO₂/Fe₂O₃. The dark portions represent (a) TiO₂ and (b) Fe₂O₃ respectively.⁹

2.4 Surface modification of metal oxide nanoparticles

In addition to their intrinsic properties such as optical, electrical, and magnetic characteristics, surface modification of metal oxide nanoparticles is a key step to extend their applications in biological and medical areas. Several ligands have shown their availability for surface modification of the metal oxide nanoparticles. The ligands and the metal oxide surfaces reacting with the ligands are summarized in Table 2.1. Details of the reactions of the metal oxide surface-modifying ligands are described as follows.

2.4.1 Silanes

Alkylalkoxysilanes with a functional group such as 3-aminopropyltriethoxy silane (APTES) and 3-aminopropyltrimethoxy silane (APTMS) are useful molecules to render functionalities on a metal oxide surface by the reaction with the surface hydroxyl groups.⁸⁰ Reaction of silane compounds with a silica surface is a well-established chemistry.⁸¹⁻⁸⁵ Levy *et al.*⁸⁶ modified the surface of silica-coated Fe₂O₃ nanoparticles with anhydride-treated APTES to attach cancer-targeting hormones on the nanocomposites. Martin and collaborators³² demonstrated differential functionalization to the inner versus outer surfaces of their silica nanotubes by sequential reaction with two different silanes in the process of the nanotube synthesis. Lee and collaborators⁸⁷ applied a similar approach to iron oxide-layered silica nanotubes to have differentially-modified inner and outer surfaces with APTES and poly(ethylene glycol)-silane respectively. APTES-modified interiors of the composite nanotubes were activated with glutaraldehyde to immobilize human IgG.

Table 2.1 Ligands and the ligand-functionalizing surfaces.⁸⁸

Ligand	Name	Reacting surfaces	References
R-SH R-S-S-R'	thiols disulfides	Au, Ag, Cu, Hg, Fe	3-5, 112-115
$\begin{array}{c} \text{O} \\ \parallel \\ \text{R}-\text{C}-\text{OH} \end{array}$	carboxylic acids	metal oxides	25, 26, 33, 35, 97, 98
$\begin{array}{c} \text{OH} \\ \\ \text{R}-\text{P}-\text{OH} \\ \parallel \\ \text{O} \end{array}$	phosphonates phosphonic acids	metal oxides	6-8, 49, 99-102
$\begin{array}{c} \text{O}-\text{R}' \\ \\ \text{R}-\text{Si}-\text{O}-\text{R}' \\ \\ \text{O}-\text{R}' \end{array}$	siloxanes	metal oxides	32, 43, 80-87, 89-96
$\begin{array}{c} \text{R} \quad \text{R}' \\ \diagdown \quad / \\ \text{C}=\text{C} \\ / \quad \diagdown \\ \text{HO} \quad \text{OH} \end{array}$	enediols	transition metal oxides (TiO ₂ , Fe ₂ O ₃ , ZrO)	3, 34, 103-109
$\begin{array}{c} \text{HO}-\text{CH}_2 \quad \text{R} \\ \diagdown \quad / \\ \text{C} \\ / \quad \diagdown \\ \text{HO}-\text{CH}_2 \quad \text{R}' \end{array}$	diols	Fe ₂ O ₃	110, 111

Silane chemistry has been employed extensively to modify the surface of iron oxide nanoparticles, maghemite (Fe_2O_3) and magnetite (Fe_3O_4). Zhang and collaborators^{89, 90} adopted silane chemistry to magnetite nanoparticles in the application of the superparamagnetic nanoparticles for MRI (Figure 2.3). They adapted APTES with a poly(ethylene) glycol (PEG)-bridge and terminal target-recognizing functionalities such as folic acid and chlorotoxin to achieve the goals of improved particle suspension time in blood and adherence to the target cells at the same time. They also achieved addition of dye molecules, Cy5.5, on the surface of the amine-functionalized magnetite surface for intraoperative optical application. Recently, Lin and collaborators⁹¹ demonstrated the usage of APTES-modified Fe_3O_4 nanoparticles as controllable caps of mesoporous silica nanorods in their study of a controlled-release delivery system. APTES- Fe_3O_4 nanoparticles capped the mesopores of the fluorescein-loaded nanorods through the reaction with 3-(propylthiol)propionic acid functional groups on the pores. The disulfide linkage was cleaved by cell-produced antioxidants and disulfide reducing agents to remove Fe_3O_4 caps from the mesopores and release fluorescein from inside of the mesoporous nanorods. O'Connor and collaborators⁴³ took advantage of affinity between Au and amine functional groups to attach Au nanoparticles around APTES-modified Fe_3O_4 nanoparticles. Hubbuch and Thomas⁹² illustrated the application of APTES-modified iron oxide nanocrystals in separation of trypsin from a mixture via a sequential modification of the APTES-iron oxide particles with polyglutaraldehyde, epichlorohydrin, and p-aminobenzamidine.

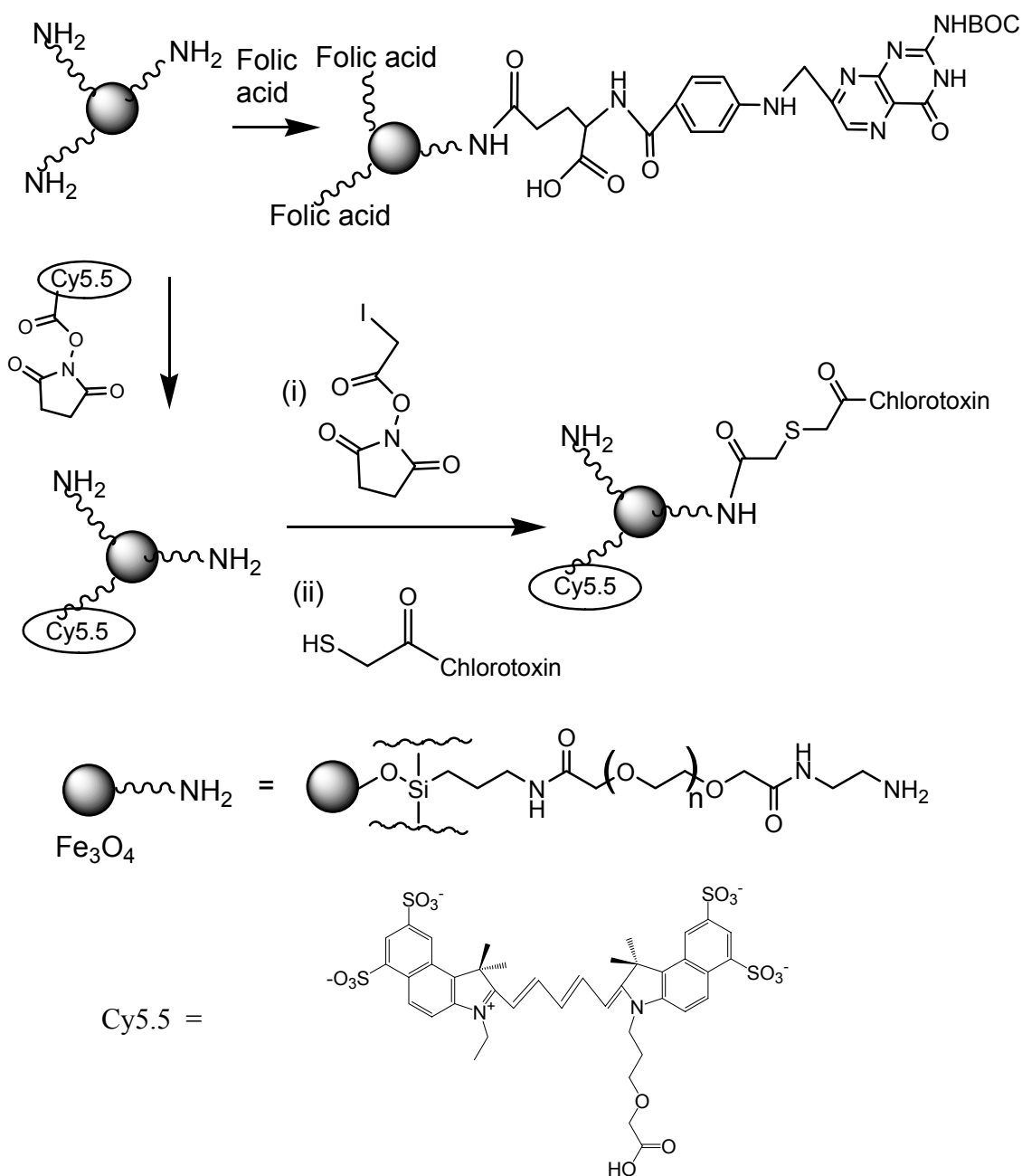


Figure 2.3 Schematic diagram of surface modification of Fe_3O_4 nanoparticles for MRI^{89, 90}. (i) Activation of amine terminal group with N-succinimidyl iodoacetate, (ii) attachment of sulfhydryl-functionalized chlorotoxin to iodoacetate-modified particles.

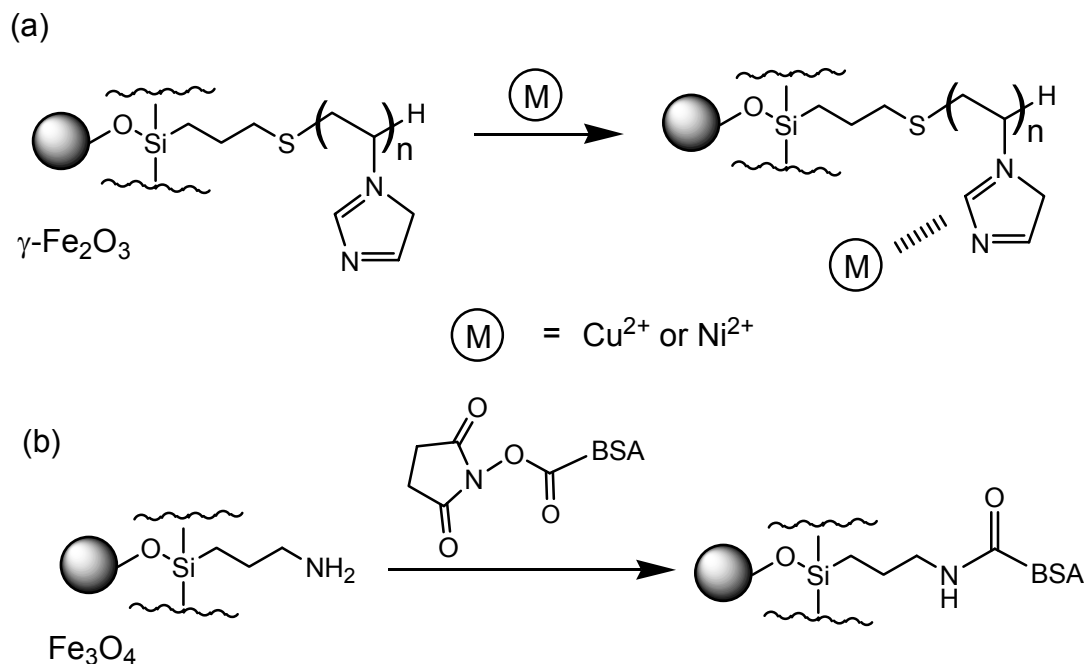


Figure 2.4 Schemes of silane chemistry on iron oxide nanoparticles: (a) metal ion removal using imidazole functional groups grafted on $\gamma\text{-Fe}_2\text{O}_3$ nanoparticles,⁹³ (b) bovine serum albumin (BSA) immobilization on Fe_3O_4 nanoparticles.⁹⁴

Xu and collaborators⁹⁵ demonstrated APTES-modification of $\gamma\text{-Fe}_2\text{O}_3$ nanoparticles in aqueous solution as well as in organic solutions such as toluene. They demonstrated the removal of divalent metal ions from solution with polymer-grafted iron oxide nanoparticles (Figure 2.4(a)).⁹³ For this purpose, they modified the terminal thiol group of 3-mercaptopropyltrimethoxysilane with poly(1-vinylimidazole) and grafted the polymer on $\gamma\text{-Fe}_2\text{O}_3$ nanoparticles using silane chemistry. Muhammed and collaborators⁹⁶ modified APTMS-iron oxide particles with PEG to improve the biocompatibility of the magnetic particles. They also demonstrated bovine serum albumin (BSA)-immobilization on iron oxide

nanoparticles in the succinimide-activated BSA treatment of the APTMS-iron oxide nanoparticles (Figure 2.4(b)).⁹⁴ The BSA-immobilized magnetic nanoparticles did not cause cell damage and no endocytosis was seen in the incubation of the modified particles with human dermal fibroblast cells for 6 and 24 hours.

2.4.2 Carboxylic acids

Several reports are available describing the use of carboxylic functional groups in surface modification of iron oxide and titania nanoparticles. Dyal *et al.*⁹⁷ demonstrated that enzymes immobilized on γ -Fe₂O₃ nanoparticles maintained their native activity for an extended period of one month. They attached 11-bromoundecanoic acid via the carboxylic linkage to the γ -Fe₂O₃ nanoparticles. After additional surface modifications, they then immobilized the enzyme via a C=N bond. Cheon and collaborators^{25, 26} illustrated recently that 2,3-dimercaptosuccinic acid (DMSA) was effective in surface modification of Fe₃O₄ nanocrystals through carboxylate bonding on the nanocrystals and intermolecular disulfide cross-linkages. They demonstrated size-dependent magnetic resonance (MR) signal intensity of the DMSA-modified Fe₃O₄ nanocrystals. The spin-spin relation time-weighted MR signal intensity decreased as the size of the surface-modified magnetic nanocrystals increased from 4 to 6, 9 and 12 nm. They achieved immobilization of cancer-specific antibodies on the magnetic nanocrystals by using the remaining free thiol groups of the surface-bound DMSA ligands. They applied the antibody-immobilized magnetic nanocrystals to *in vitro* and *in vivo* mouse MRI.

Dimitrijevic and collaborators^{35, 98} exhibited attachment of carboxyethyl β -cyclodextrin on TiO₂ nanoparticles via carboxyl linkages to the surface Ti atoms.

Surface-conjugated cyclodextrins were used as host molecules as the hydrophobic cavity of cyclodextrin is well-suited for host-guest interactions in aqueous solutions. They observed guest-oxidation potential controlling charge separation and trapping. The high oxidation potential of adamantane serving as a guest molecule prevented charge transfer between TiO₂ and the entrapped guest, while the low oxidation potential of ferrocenemethanol led to oxidation and dissociation of the guest from the inclusion complex. Weng and collaborators³³ described size-controllable binding nature of all-*trans*-retinoic acid with TiO₂ nanoparticles. Their transient absorbance difference spectra demonstrated that chemical bonding became more dominant versus physisorption as the semiconductor nanoparticle-size decreased from 6 to 0.8-1.4, and 0.7 nm.

2.4.3 Phosphorous compounds

Organophosphorous compounds have attracted interest as an alternative to organosilane compounds in functionalization of inorganic surfaces due to their characteristic features such as a large number of available organophosphorous functional molecules and difference in surface reaction mechanisms between phosphorous- and silane-compounds.⁹⁹ Many metal oxides, including metal oxides of titanium, aluminum, iron, steel, copper, and brass, have been used as matrix in organophosphorous compound-involved surface modification.⁹⁹ Binding mode of organophosphorous molecules can be mono-, bi-, and tridentate as a combination of the property of functionalizing surfaces and the nature of the organophosphorous compounds. Surface modification of TiO₂ with phosphonates or phosphonic acids is an attractive topic because of the altered catalytic function of the transition metal

oxide surface.⁶ Phosphonates and phosphonic acids form self-assembled monolayers (SAMs) on TiO₂ surface by the formation of Ti-O-P bonds. Textor, Spencer, and collaborators have extensively studied alkyl phosphate-SAM formation on TiO₂ in alkyl phosphate ammonium salt-dissolved aqueous solutions.^{7, 8, 100, 101} X-ray photoelectron spectroscopy was employed to study the binding of TiO₂-alkyl phosphates. Water contact angles on a SAM-formed surface depended on the nature of the tail group of the phosphates, either hydrophobic alkyl- or hydrophilic hydroxy-alkyl groups.¹⁰⁰ Grätzel and collaborators demonstrated dye-sensitized solar cells using a combined effect of photosensitivity of the TiO₂ surface and surface modification-provided stability of the photovoltaic cells.¹⁰² An amphiphilic ruthenium compound and dodecyl phosphonic acids were bound to TiO₂ surface to improve the lifetime of the solar cells. Chen and Chen⁴⁹ applied the affinity of TiO₂-phosphorus compound to magnetic-field assisted separation of phosphopeptides from an enzyme-digest mixture using TiO₂-coated Fe₃O₄ nanoparticles.

2.4.4 Diols

Bidentate binding of enediol ligands stabilizes undercoordinated surface metal atoms on the surface of transition metal oxide nanoparticles: TiO₂, Fe₂O₃, and ZrO₃.³⁴ This bidentate binding was reported to be characteristic of nanocrystalline metal oxide particles below 20 nm in diameter. Enediol ligand-binding onto 4.5 nm TiO₂ nanoparticles altered the optical characteristics of the nanoparticles due to the shift in the dipole moment of Ti-ligand complexes. Dopamine (DA) is of particular interest among the enediol ligands, since the terminal amine group of dopamine can be further modified by reaction with other functional molecules. Dopamine pretreated with

functional molecules such as nitrilotriacetic acid (NTA) or biotin demonstrated a robust binding on iron oxide nanoparticles below 10 nm used for separation of histidine-tagged proteins or streptavidin.^{3, 103} DNA oligonucleotides were hybridized onto 4.5 nm TiO₂ particles through dopamine-bridging and the photocatalytic, electronic, and bioactive characteristics of the TiO₂-oligonucleotide nanocomposites were assessed.^{104, 105} Size-dependent binding of enediol ligands such as dopamine on TiO₂ nanocrystalline surfaces was the basis for tip-to-tip assembly of TiO₂ nanorods.^{106, 107} Biotinylated dopamine exhibited a preferential binding on undercoordinated Ti atoms at the highly-curved tips of the nanorods. Reaction of avidin with the TiO₂/DA-biotin structure resulted in a linear assembly of the nanorods. The presence of 3,4-dihydroxyphenylalanine (DOPA), the precursor of dopamine, is correlated with the adhesive properties of mussel adhesive proteins. PEG-DOPA-TiO₂ nanoparticle complexes exhibited resistance to serum protein adsorption.^{108, 109}

Rotello and collaborators¹¹⁰ illustrated that 1,3-diols with bulky tail groups were attached to as-synthesized alkylamine-coated γ -Fe₂O₃ nanoparticles in an exchange reaction with the surface alkylamines. They attributed the stability of the diol-modified magnetic nanoparticles to both the bidentate coordination of diols and steric stabilization of the bulky tail groups. They demonstrated dendrimer-mediated self-assembly of the magnetic nanoparticles through an electrostatic interaction between cationic functional derivatives at the end of the 1,3-diol bulky tails and anionic polyamidoamine dendrimers.¹¹¹

2.5 Multifunctional metal oxide nanoparticles and nanocomposites

Multifunctionality of nanostructures including biobARRIER-overcoming ability, target-specificity, and drug-delivery is a key feature to their biological applications. Differential functionalization of multi-component nanocomposites leads to fabrication of multifunctional nanostructures. Differential functionalization of metal-metal, metal-metal oxide, and metal oxide-metal oxide surfaces has been achieved via preferential binding of a given functional compound to a specific component and is described below.

Differential functionalization of metal-metal surfaces: Differential functionalization of metal-metal surfaces is achieved using multi-component nanowires synthesized in template-based fabrication methods. Most of these approaches employ Au-metal nanowires to use thiol-affinity toward Au surface. Leong and collaborators⁵ demonstrated segment-dependent binding of DNA plasmids and targeting molecules to Au-Ni bimetallic nanowires. They applied this approach to *in vivo* and *in vitro* gene delivery. Mirkin and collaborators⁴ displayed a magnetic-field assisted separation of histidine-tagged proteins by differential modification of Au-Ni-Au tri-segment nanowires with binding of thiolated PEG (PEG-SH) to Au end portions and affinity of histidine-groups to the Ni portion. PEG-SH binding to gold end segments functioned to suppress nonspecific binding of proteins and to stabilize suspension of the nanowires. Metal-metal nanowires such as Au-Ni⁵ and Au-Pt⁴ exhibited the selective adsorption of functional molecules and proved their applicability in gene delivery and separation of histidine-tagged proteins.

Recent efforts to fabricate metal oxide-metal nanocomposites are described in Section 2.3.1.

Differential functionalization of metal-metal oxide surfaces: Differential

functionalization on metal oxide-Au heterodimeric nanoparticles was achieved using the preferential binding of a thiol group on Au surface over metal oxide surfaces.³

Whiteside and collaborators demonstrated simultaneous differential functionalization of Au-alumina surface via preferential binding of Au-alkane thiol and alumina-alkane carboxylic acid.¹¹² Since then a large number of applications have been reported using a similar approach to differently fabricated Au-metal oxide surfaces.¹¹³⁻¹¹⁵

Specific binding interaction of Au-thiol compounds is also used for a differential modification of Au-metal oxide nanoparticles to acquire multifunctionality. Very recently, Xu and collaborators³ developed binary nanoparticles of Fe₃O₄-Au via self-assembly of metal oxide nanoparticles at liquid-liquid interface and partial exposure of the inorganic particle surface to a reactant, silver nitrate. They employed a sequential surface-specific binding approach of Au-thiolated porphyrin and Fe₃O₄-biotinylated dopamine. In this way, the differentially-modified Fe₃O₄-Au binary nanoparticles exhibited a dual function of porphyrin-related fluorescence and biotin-mediated separation of avidin-functionalized molecules.

Selective modification of metal oxide-metal oxide surfaces: Selective reaction of functional molecules on a metal oxide-metal oxide surface is a challenging task compared with multifunctional reactions on metal-metal and metal-metal oxide

surfaces, since most functional groups exhibit a similar binding affinity to both the metal oxide surfaces. Nonetheless, a few reports of selective functionalization on SiO₂-TiO₂ surfaces are available, using the preferential binding of phosphonic acids and organic phosphates on the TiO₂ portions of the mixed metal oxide surfaces. Mutin *et al.*⁶ demonstrated through their solid-state NMR studies that phosphonic acids were bound on a SiO₂ surface in toluene, an organic aprotic solvent (Figure 2.5(a)). However, the phosphonic acid-binding on the silica surface was not detected in an aqueous solution likely due to the hydrolysis of the Si-O-P bonds. Much higher stability of Ti-O-P bonds against hydrolysis led to the formation of the bonds on a TiO₂ surface via the reaction with the phosphonic acids in the aqueous environment. Both chemical bond formation and physical coordination of surface Ti atoms contributed to the binding of the phosphonic acids on the TiO₂ surface. In addition, scanning auger electron spectroscopy analysis of phosphonic acid-modified SiO₂-TiO₂ support substantiated their NMR study results by showing a preferential binding of the phosphonic acid to the TiO₂ region. Based on their results, they suggested selective sequential functionalization of the SiO₂-TiO₂ mixed oxide surface by the following two steps: (i) preferential reaction of phosphonic acid on the TiO₂ region, (ii) subsequent binding of trimethylsilyl group on the remaining SiO₂ portion using a mild silylating agent, N,O-bis(trimethylsilyl)trifluoroacetamide (BSTFA). Michel *et al.*^{7,8} reported selective surface fabrication of a SiO₂-TiO₂ surface by using the preferential self-assembly of organic phosphates on the TiO₂ region in an aqueous solution (Figure 2.5(b)). The remaining SiO₂ surface after the phosphate treatment became protein binding-resistant through adsorption of poly(L-lysine)-g-

poly(ethylene glycol) (PLL-g-PEG) on the SiO₂ portion. They adopted X-ray photoelectron spectroscopy (XPS) and time-of-flight secondary ion mass spectrometry (ToF-SIMS) to characterize the selective modification of the mixed oxide surface. XPS results for the carbon (1s) region along with ToF-SIMS mapping results demonstrated that organic phosphates were selectively bound on the TiO₂ surface and the subsequent PLL-g-PEG treatment led to adsorption of PLL-g-PEG on both TiO₂/phosphates and SiO₂ surfaces. Immersion of the selectively-modified TiO₂-SiO₂ surface in full serum resulted in replacement of the loosely-bound PLL-g-PEG on TiO₂/phosphates with proteins while the SiO₂/PLL-g-PEG surface was unaffected. They proved through fluorescence microscopy and atomic force microscopy studies that chemical patterns could be constructed on the selectively-modified TiO₂-SiO₂ surface with organic phosphates and PLL-g-PEG due to the protein-binding resistant character of the SiO₂/PLL-g-PEG surface.

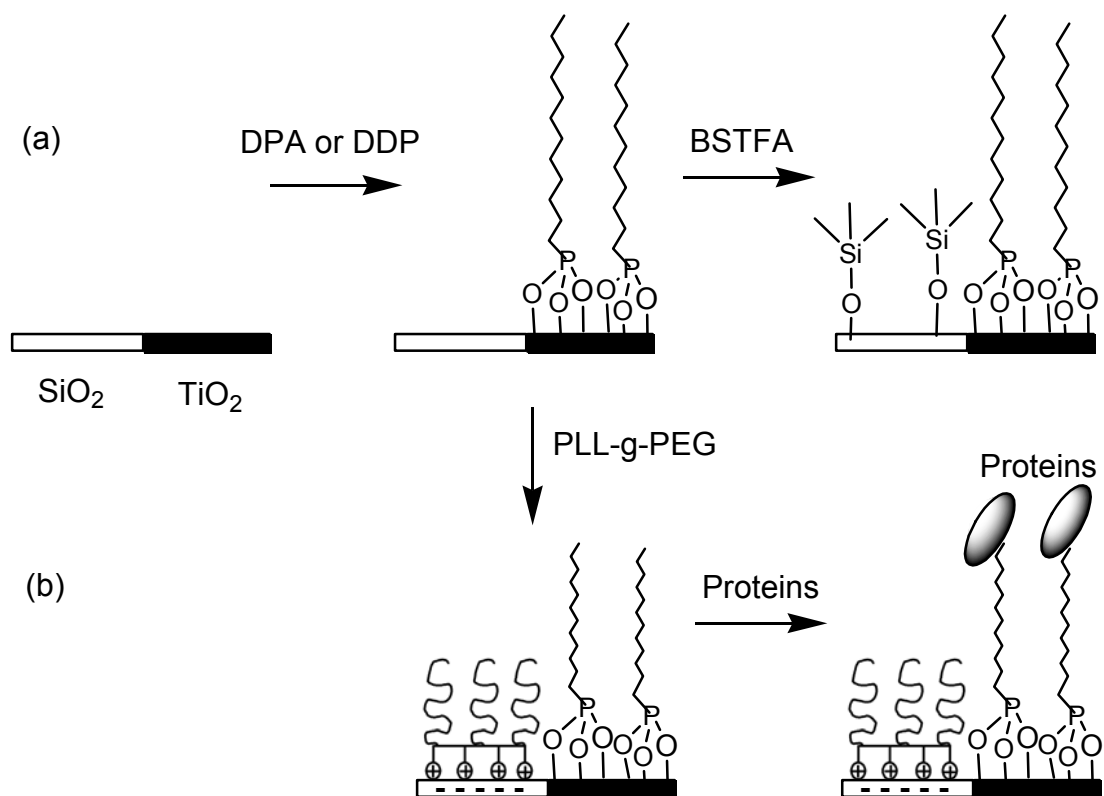


Figure 2.5 Differential functionalizations of SiO₂/TiO₂ surfaces: Sequential functionalization with (a) DPA and BSTFA,⁶ and (b) DDA and PLL-g-PEG.^{7,8} DPA: Dodecyl phosphonic acid, DDP: Dodecyl phosphate.

2.6 Cellular membranes and X-ray scattering

2.6.1 *E.coli* cellular membrane

Escherichia coli was used in Chapters 5 and 6 to demonstrate its magnetic field-assisted interactions with magnetic nanoparticles, SiO₂/γ-Fe₂O₃ mixed particles. *E. coli* is gram-negative bacteria and the dimension of the *E. coli* cell is about 2 μm in length and a little less than 1 μm in diameter. The cell envelope of gram-negative bacteria is composed of three layers: outer membrane, peptidoglycan layer and inner (cytoplasmic) membrane.¹¹⁶ Figure 2.6 demonstrates an electron micrograph of a gram negative cell wall.

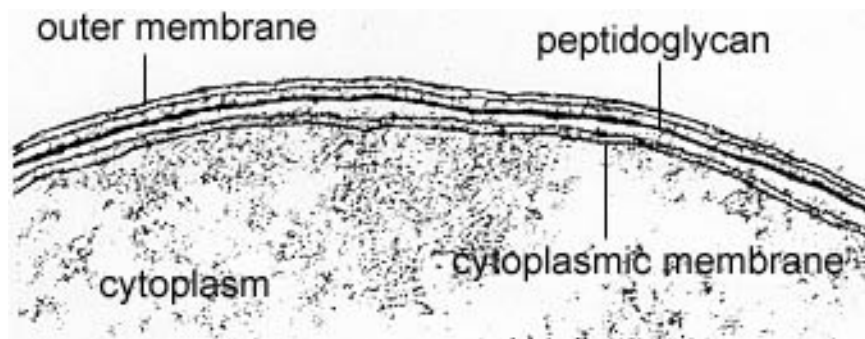


Figure 2.6 Electron micrograph of a gram negative cell wall.¹¹⁷

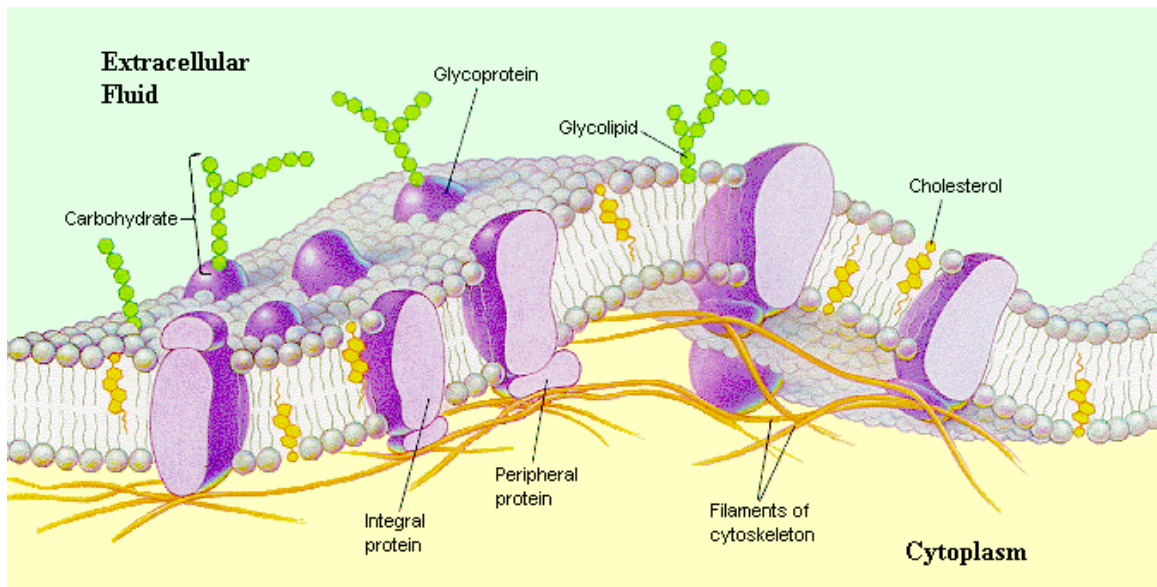
The peptidoglycan layer is generally 2-3 nm thick with the composition of cross-linked sugar polymers. The peptidoglycan layer helps the bacteria to maintain the shape and rigidity. The cellular membranes are 7 nm in average thickness with the main composition of lipids and proteins. A fluid mosaic model of a cellular membrane (Figure 2.7) is generally used to understand the cellular membrane.

2.6.2 X-ray scattering

In this dissertation, the *E. coli* cell membrane-magnetic nanoparticle interactions were detected with X-ray scattering, as described in Chapters 5 and 6. X-rays are electromagnetic radiation of wavelength in the range between 10 and 0.1 nm. A typical process of the generation of X-rays for X-ray scattering experiments is described as follows. Monochromatic X-rays are produced when a beam of accelerated electrons in a high voltage such as 30 kV collide with a metal target, often copper. Collisions with enough energy knock out some of the copper 1s (K shell) electrons. Energy release in the transition of electrons from the outer-orbital (2p or 3p) to the vacancy is emitted as X-ray radiation. Copper 2p \rightarrow 1s transition is called $K\alpha$ with a wavelength of 1.5418 Å. This $K\alpha$ radiation is commonly employed in X-ray scattering experiments.

Bragg's Law is used to measure the perpendicular distance between adjacent planes of crystals, the d-spacing, from X-ray scattering data. The derivation of Bragg's Law is presented in Appendix C.4.1.

(a)



(b)

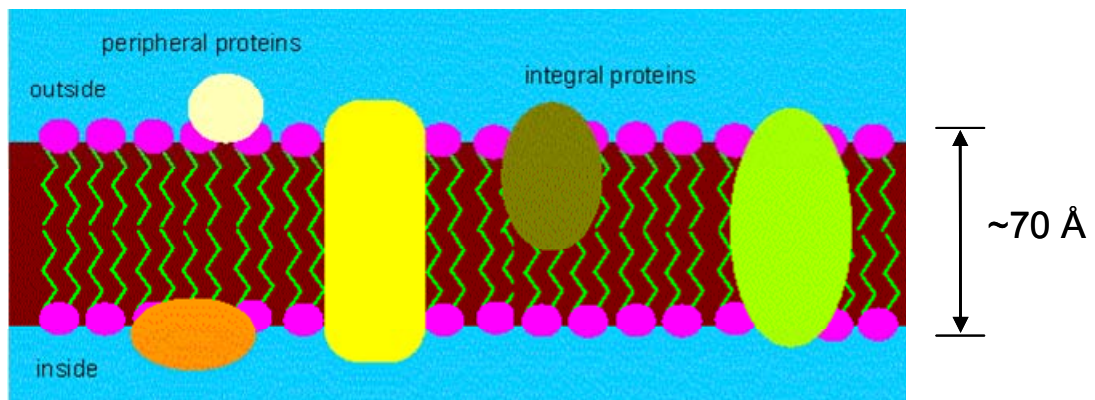


Figure 2.7 Fluid mosaic model of a cell membrane. (a) A two dimensional model,¹¹⁸

(b) an one dimensional model.¹¹⁹

Chapter 3: Magnetic iron oxide nanoparticles for bio-recognition: Evaluation of surface coverage and activity

3.1 Abstract

Modifying the surface of magnetic nanoparticles (MNPs) by the covalent attachment of biomolecules will enable their implementation as contrast agents for magnetic resonance imaging or as media for magnetically assisted bioseparations. This chapter describes both the surface coverage and activity of IgG antibodies on MNPs. The antibodies were immobilized on γ -Fe₂O₃ nanoparticles by conventional methods using aminopropyltriethoxy silane and subsequent activation by glutaraldehyde. Novel fluorescence methods were used to provide a quantitative evaluation of this well-known approach. The results show that surface coverage can be stoichiometrically adjusted with saturated surface coverage occurring at ~ 36% of the theoretical limit. The saturated surface coverage corresponds to 34 antibody molecules bound to an average-sized MNP (32 nm diameter). The results also show that the immobilized antibodies retain ~50% of their binding capacity at surface-saturated levels.

3.2 Introduction

Magnetic iron oxide nanoparticles (MNPs) are inherently biocompatible^{97, 120} and are amenable to post-synthesis surface modification making them excellent candidates for many important applications. For instance, biotechnological

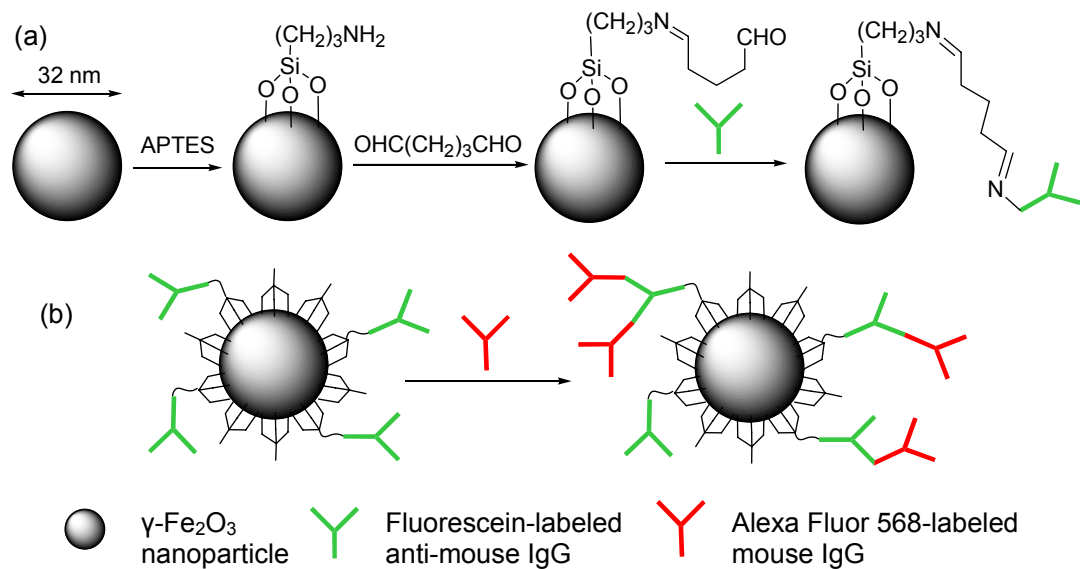
applications of MNPs include magnetic resonance (MR) imaging contrast agents,^{25, 26, 89, 90} targetable drug carriers,¹¹ hyperthermia-inducing agents^{121, 122} and magnetically controlled media for sensitive separation and detection of biomolecules.^{123, 124} In order to optimize MNPs for these applications it is necessary to confer a high level of binding-specificity through surface chemistry. High specificity can be introduced by using biological moieties that possess lock-and-key interactions including those observed in antibody-antigen and enzyme-substrate recognition. In surface modifications involving biomolecules, surface coverage is critically important as is the ability for the immobilized molecules to retain their native conformations and binding profiles.

One extremely useful route to post-synthetic modification of iron oxide nanoparticles is accessed by employing the common organosilane reagent, γ -aminopropyl triethoxy silane (APTES).⁹⁵ This approach has been used to produce polymer grafted magnetic nanoparticles (MNPs)^{89, 93, 96} and to attach proteins to iron oxide nanoparticles.^{94, 125} Studies of bovine serum albumin immobilized in this way on MNPs showed that the coated nanoparticles remain superparamagnetic and that they undergo translocation into human dermal fibroblast cells.⁹⁴ Attachment of the enzyme horseradish peroxidase (HRP) to APTES-modified iron oxide nanoparticles was demonstrated by Ma *et al*¹²⁵ and the immobilized HRP remained enzymatically active with a surface coverage approximately two times greater than with native particles. These previous studies have relied upon thermogravimetric and chemical analysis to evaluate surface modification of nanoparticles prepared at a single protein-nanoparticle stoichiometry. Here this approach is complemented and expanded by

using fluorescence spectroscopy to report a full chemisorption isotherm analysis.

Fluorescence microscopy is also employed to confirm antibody activity.

This chapter reports the characterization of surface coverage, as well as antibody activity, of amine-coated MNPs modified with anti-mouse immunoglobulin G (IgG) antibodies (Scheme 3.1). The results gained from these studies are of obvious importance since the antibody/antigen interaction can be exploited for a variety of target molecules and organisms. APTES provides a common intermediate that is amenable to a wide range of subsequent modifications, particularly with respect to biomolecule immobilization. In principle, any soluble protein can be immobilized using glutaraldehyde as a cross linker between an amine functional group on the protein and the APTES surface groups. However, proteins with amine side chains (i.e. lysine residues) may have multiple points of attachment which introduce a further level of complexity in terms of the possible orientations.^{126, 127} To investigate the applicability of the APTES approach for antibody immobilization on MNPs, the well-characterized anti-IgG antibody has been immobilized. Fluorescence-based assays have provided a quantitative determination of surface coverage and evaluated the activity of the attached antibody. Fluorescence assays provide high sensitivity and avoid problems due to spectral overlap between the iron oxide nanoparticles and fluorophores when both are present since iron oxide is not fluorescent. These methods provide valuable quantitative information and should be applicable to a wide range of ligands.



Scheme 3.1 (a) Surface modification of $\gamma\text{-Fe}_2\text{O}_3$ nanoparticles with APTES for the immobilization of fluorescein-labeled anti-mouse IgG (FL-anti-mouse IgG). (b) Separation of Alexa Fluor 568-labeled mouse IgG (AF-mouse IgG) using the anti-mouse IgG antibody coated MNPs.

3.3 Experimental methods

3.3.1 Materials

The γ -Fe₂O₃ particles were purchased from a commercial source (Alfa Aesar, Ward Hill, MA). The surface area of the particles is 42 m²/g (determined by BET measurement) and the average size is 32 ± 18 nm (from TEM). These values are consistent with published values^{95, 128} and those supplied by the manufacturer. Reagent grade 3-aminopropyltriethoxysilane (APTES) and glutaraldehyde were purchased from Sigma (St. Louis, MO) and polysciences (Warrington, PA), respectively. FL anti-mouse IgG and purified mouse IgG in phosphate buffered saline (PBS; pH 7.4, 0.05 % sodium azide), were purchased from Invitrogen (Carlsbad, CA) and from Zymed (South San Francisco, CA), respectively. Alexa Fluor 568 succinimidyl ester was purchased from Molecular Probes (Eugene,OR). All chemicals were used as received without further purification except mouse IgG which was dialyzed to reduce the concentration of sodium azide prior to the dye-labeling reaction (see below).

3.3.2 APTES modification of magnetic iron oxide nanoparticles

All glassware was soaked in piranha solution (conc. H₂SO₄ and 35% H₂O₂, 3:1 v/v) for one hour and rinsed with distilled water before use. 1.5 g of γ -Fe₂O₃ nanoparticles was dispersed in 45 mL of distilled water using sonication to produce a homogenous suspension. The suspension was then purged with nitrogen in a three-necked flask. 5 mL of APTES was added to the suspension drop-wise for a final

concentration of 10 % APTES (v/v). The solution was refluxed for 3 h at 120 °C under nitrogen atmosphere and with vigorous mechanical stirring. The APTES-modified particles were collected in a centrifuge tube using a neodymium-iron-boron permanent magnet (Arbor Scientific, Ann Arbor, MI) and then washed with double distilled water three times and with ethanol once. The harvested particles were dried in vacuum overnight and stored in a desiccator.

3.3.3 Preparation of antibody-coated iron oxide nanoparticles through crosslinking with glutaraldehyde

Magnetic nanoparticles were coated with the fluorescently labeled secondary antibody, goat anti-mouse IgG. 10 mg of the APTES-modified nanoparticles were added in 0.5 mL of PBS (pH 7.4) and sonicated for 5 min. 1.5 mL of 8 % glutaraldehyde solution in PBS was added to the particle suspension and the mixture was vortexed briefly. The suspended particles were mixed gently for 6 h at room temperature. The activated particles were magnetically collected and washed three times with PBS and then suspended in 4.0 mL of PBS. 80 μ L of the suspension (0.20 mg of particles) was added to a PBS solution of anti mouse IgG for a final volume of 1.0 mL and shaken for 20 h at room temperature. The resulting surface-modified MNPS were harvested and washed four times with 1 mL of PBS. The supernatant and washing solutions were kept to determine the amount of unreacted antibody.

Quantitative determination of the amount of unreacted antibody was used to calculate the degree of surface coverage. This approach was necessary for accurate quantification of antibody binding since absorption and scattering artifacts along with

particle settlement during measurement prevent the direct accurate measurement of conjugation in the actual product. The amount of unreacted dye was fluorometrically determined after first establishing a standard calibration curve (Appendix A). The amount of dye-labeled antibody bound to the nanoparticles was calculated using the following equation:

$$\begin{aligned} &\text{Amount of bound antibody} \\ &= \text{initial quantity of antibody} - \text{unreacted quantity of antibody} \end{aligned}$$

Interestingly, it was found that upon binding of the dye-labeled antibody to the nanoparticle surface, the emission efficiency of the fluorescein label was decreased by ~200 fold. Quenching of the immobilized fluorophore upon surface immobilization is further reason for measuring unreacted antibody to determine surface coverage.

3.3.4 Dye-labeling of target antibody

The dye labeling of mouse IgG was carried out using methods described by the dye supplier. In brief, mouse IgG (2.5 mg/mL) in 10 mM PBS (pH 7.4, 0.05% sodium azide) was dialyzed using a Spectra/Por (Rancho Dominguez, CA) dialysis kit (molecular weight cut-off 50,000) to reduce sodium azide concentration. Next, 0.2 mL of 1 M sodium bicarbonate buffer (pH 8.5) was added to 2 mL of the dialyzed antibody solution to attain the appropriate pH for the attachment of dyes. 1 mg of Alexa Fluor 568 succinimidyl ester dissolved in 0.1 mL of DMSO was added to the antibody solution and mixed for 1 h. Alexa Fluor 568 labeled-mouse IgG (AF-mouse IgG) was separated from the unreacted dye with gel permeation chromatography

using Sephadex G-25 (Amersham Biosciences, Piscataway, NJ). The degree of labeling of the resulting protein-dye conjugate was determined by UV-Vis absorbance at 280 nm and 575 nm to be 0.20 mg/mL for an average of 4.4 attached dye molecules per antibody.

3.3.5 Magnetic immobilization of target antibody (mouse IgG) using the anti-mouse IgG modified MNPs

Antibody coated magnetic nanoparticles (400 μ L of 10 mg MNP/20 mL) were added to 600 μ L of AF-mouse IgG. A range of AF-mouse IgG concentrations were studied. Samples were mixed for 3 h, collected and washed four times each with 1 mL of PBS. Steady-state fluorescence was used to evaluate the amount of bound primary antibody. Fluorescence spectra of the magnetically captured nanoparticle suspensions were taken with excitation wavelength of either 480 nm for excitation of fluorescein or 550 nm for excitation of Alexa Fluor 568.

3.3.6 Fluorescence microscopy and spectroscopy

Steady state fluorescence measurements to evaluate antibody surface coverage and reactivity were conducted with either a Spex Fluorolog-3 fluorometer (Horiba Jobin Yvon Inc, Kyoto, Japan) or a Hitachi F-4500 fluorescence spectrophotometer (Tokyo, Japan). For the quantitative determination of the concentration of fluorescein in washings and supernatant solutions, a calibration curve was first established over the dye concentration range of interest. The fluorescence intensity was linear with dye concentration over the entire calibration curve. Care was taken to conduct the

experiments under the same conditions used to establish the calibration curve to avoid pH and instrument effects when determining the experimental dye concentration.

Fluorescence images and spectroscopic data were acquired using a sample scanning confocal microscope. The microscope was described previously^{129, 130} and consists of a modified Axiovert 200 (Carl Zeiss, Oberkochen, Germany) with a NanoBio-2 (Mad City Labs, Madison, Wisconsin) closed-loop, piezoelectric scanning stage for nanometer precision. The microscope is equipped with a 15 cm monochromator with a 150 g/mm grating (Acton Research Corporation, Acton, MA) for acquisition of emission spectrum from any region of a confocal image with high spatial resolution (300 nm) and positioning accuracy (< 10 nm). For confocal microscopy studies, the particles in PBS were spin coated on a glass slide and imaged with 488 nm laser light (Melles Griot, Carlsbad, CA).

3.3.7 X-ray photoelectron spectroscopy

XPS measurements were performed using an AXIS 165 spectrometer (Kratos Analytical Inc, Chestnut Ridge, NY) with monochromatic Al K α x-ray source (144 W). A sample of powder, loaded onto a conductive carbon tape on a stub, was put into the vacuum chamber under a background pressure of 4×10^{-10} Torr. Wide scan surveys and specific regions (for example, C1s, N1s) were measured in hybrid mode using both electrostatic and magnetic lenses with a step size of 0.1 eV. XPS spectra were recorded in the FAT analyzer mode with pass energy of 80 eV and an average of ten scans. The charge neutralizer was off during the measurements and calibration of binding energy was carried out with respect to C1s at 284.6 eV. Data processing was

done using Vision processing software(Kratos Analytical Inc, Chestnut Ridge, NY). After subtraction of a linear background, all spectra (except Fe2p) are fitted with 60% Gaussian /40% Lorentzian peaks, taking the minimum number of peaks consistent with the best fit.

3.3.7 Transmission Electron Microscopy (TEM)

Nanoparticle size and size distribution for unreacted-, APTES-modified, and FL-anti IgG immobilized MNPs were characterized with TEM using a Zeiss EM10CA microscope. For TEM sample preparation MNPs were suspended in PBS (pH 7.4) and then drop cast on a TEM grid. TEM images are provided in Appendix A.15.

3.4 Results and Discussion

The initial MNP surface modification step, reaction with APTES, was verified using X-ray photoelectron spectroscopy (XPS). The XPS results are summarized in Figure 3.1. Each panel of Figure 3.1 displays a region of the XPS spectrum corresponding to binding energies of an element that is characteristic of APTES or iron oxide. For comparison, the XPS spectrum of bare unmodified MNPs is represented by Trace a in each panel while Trace b corresponds to the MNPs after reaction with APTES.

Comparisons of the peaks in each panel clearly show the appearance of new features at the binding energies of carbon, nitrogen and silicon. The C1s peaks at

284.8 eV and 287.7 eV in Traces a and b are from the carbon tape which is used to introduce the powder samples into the UHV chamber of the XPS. The additional peak at 286.5 eV, appearing in the XPS spectrum of the modified nanoparticles (Trace b), is assigned to the terminal methylenes of the propyl group (i.e. CH₂-N and CH₂-Si). The broad N1s peak appearing at 402 eV is from the amine functional group in both protonated and unprotonated form present in APTES.⁹⁵ There was no change in binding energy or peak shape observed in the Fe2p region for the magnetic particles before and after the silanization reaction with APTES.

XPS measurements of the carbon tape used to mount the samples confirmed the presence of a Si2p peak at 101.5 eV. This peak is evident in the spectrum from the bare nanoparticles and is attributed to silicon impurities in the carbon tape. The Si2p peak broadens significantly after the nanoparticles are reacted with APTES and was fit using a pair of Gaussians as shown in Figure 3.1. One Gaussian represents the peak present in the bare carbon tape spectrum and the second Gaussian, centered at 103.9 eV, is assigned to the APTES silicon atom bound to the iron oxide surface. This peak position, while occurring at a higher energy than previously reported by Finch and coworkers for APTES on γ -Fe₂O₃,⁹⁵ is consistent with values for Si2p in silicates¹³¹ and indicates that the surface bound APTES may be substantially cross linked. The APTES-modified nanoparticles were magnetically isolated and extensively rinsed before preparing XPS samples; therefore, the presence of new carbon, silicon and nitrogen peaks in the XPS spectra must arise from covalently attached, and not simply physisorbed, APTES.

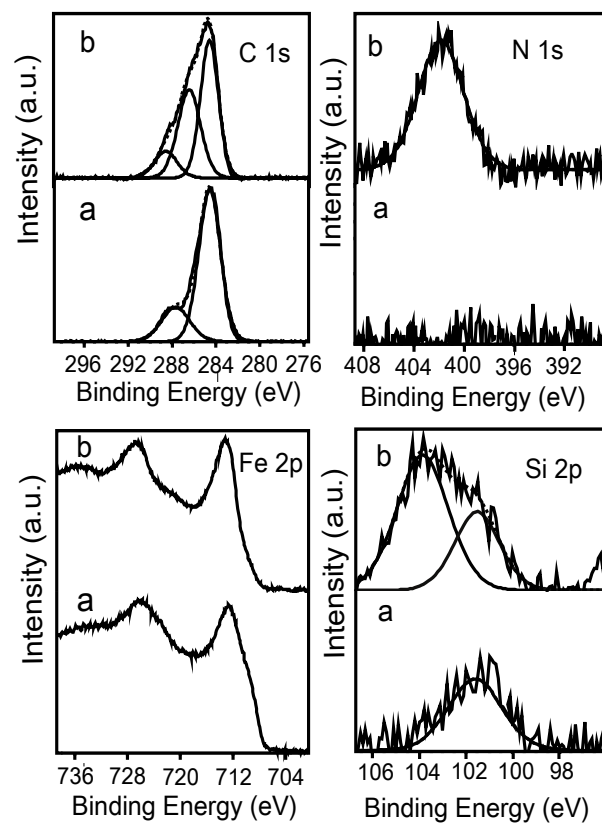


Figure 3.1 XPS spectra of γ -Fe₂O₃ nanoparticles: a) unmodified γ -Fe₂O₃ nanoparticles, b) APTES-modified γ -Fe₂O₃ nanoparticles.

Freshly prepared APTES modified particles were next modified by reaction with glutaraldehyde to activate the amine group for protein conjugation. Protein conjugation was carried out by reacting 1.0 mL aliquots containing a fixed concentration of glutaraldehyde-activated nanoparticles with different concentrations of fluorescently-labeled anti-IgG antibody. Quantitative fluorescence assays were conducted to determine the degree of surface coverage as a function of antibody concentration (described in Experimental Section).

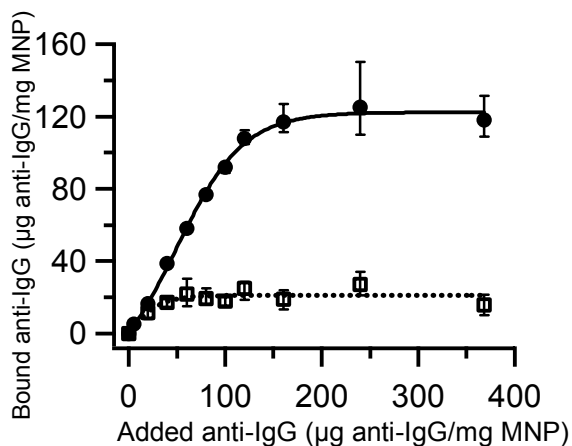


Figure 3.2 Adsorption isotherm of fluorescein-labeled anti-mouse IgG antibody on γ -Fe₂O₃ nanoparticles. ●: glutaraldehyde-activated amino γ -Fe₂O₃ particles, ◻: plain γ -Fe₂O₃ particles.

Figure 3.2 shows the chemisorption isotherm for FL anti-mouse IgG on glutaraldehyde-activated APTES-coated nanoparticles (solid circles) and on bare γ -Fe₂O₃ nanoparticles (empty squares). The bare nanoparticles were used as a control sample for determining the amount of nonspecific binding. In both cases, the surface coverage increases linearly at low antibody concentrations and is followed by a plateau region beginning near 160 μ g of added anti-IgG per mg of APTES-modified MNPs and at 60 μ g of added anti-IgG per mg of bare MNPs. In the case of bare nanoparticles, it is assumed that the saturation concentration is determined by adsorption/desorption kinetics of the antibody and the curve can be well described as a Langmuir isotherm (dotted line). For modified nanoparticles coated with activated APTES, formation of a Schiff base occurs between the free aldehyde group on the nanoparticle and amine groups on the antibody surface. This provides a stable covalent attachment and hence there is no observable desorption of the antibody.^{126, 127} This is shown by the isotherm in which the linear region at low concentrations increases in direct proportion with the antibody in solution until the binding sites are saturated as indicated by the plateau at 160 μ g of added anti-IgG.

The plateau corresponds to the loading capacity of available binding sites on the glutaraldehyde activated particles and extrapolates to 122 μ g anti-IgG per mg MNP. Based upon known antibody molecular dimensions (Y-shape; height = 8.5 nm, width = 14.5 nm, thickness = 4.0 nm)¹³² the antibody footprint on the immobilizing surface can vary from 34 to 120 nm² depending on binding orientation. If the antibody binds to the surface through the F_c domain the per-molecule “footprint” should be 58 nm². The average surface area for the magnetic iron oxide nanoparticles

from BET measurements is $42 \text{ m}^2/\text{g}$. These values indicate that a close-packed monolayer of F_c -bound IgG antibody would correspond to $200 \text{ }\mu\text{g anti-IgG/mg MNP}$. Hence the observed saturation at $122 \text{ }\mu\text{g anti-IgG/mg MNP}$ is 61% of the theoretical monolayer for this orientation. For maximum theoretical surface loading the antibody must bind in an edge-on orientation with the minimum footprint of 34 nm^2 . In this case the observed saturation value would correspond to 36% coverage for this optimal orientation. The calculations assume homogeneous orientation, rectangular footprints and perfect packing of the bound antibodies. In reality the antibodies will have mixed orientations^{126, 127} and a monolayer with surface coverage below the theoretical maximum of $330 \text{ }\mu\text{g anti-IgG/mg MNP}$ (assuming a homogeneous edge-on orientation for all bound IgG) can be expected. Therefore, it is likely that our saturation value represents the maximum level of surface coverage obtainable with mixed orientations.

The fact that 36% of the theoretical maximum coverage is obtained indicates that the activated-APTES surface-modification is a good promoter of efficient coverage by the antibody. In comparison, bare nanoparticles exhibit only nonspecific adsorption which saturates at $20 \text{ }\mu\text{g anti-IgG/mg}$ of the bare nanoparticles and this value corresponds to 6% of the theoretical monolayer. Therefore, a six-fold increase is observed in surface coverage for APTES-modified nanoparticles corresponding to 34 antibody molecules for an average size nanoparticle with 32 nm diameter.

In addition to adequate surface coverage, retention of bioactivity is critical for producing modified MNPs capable of bio-recognition. To investigate whether the immobilized antibody remains active on the nanoparticle surface, magnetic-based

separations were conducted. In these experiments the immobilized antibody (anti-mouse IgG) is used to capture and hold a target antibody (mouse IgG) that is present in solution. The MNPs are then magnetically separated and the amount of captured target antibody is measured and plotted against target antibody solution concentration (Figure 3.3C). The MNPs used in this study were coated with anti-mouse IgG at levels corresponding to the saturation point in Figure 3.2 to ensure that the particle surfaces are initially well coated with anti-mouse IgG. The concentration of MNPs was the same in all separations. The target antibody, mouse IgG, was labeled with Alexa Fluor 568 (AF) as described in the supporting information. The dye-labeling was performed on both the immobilized and the target antibody to enable direct spectroscopic verification of binding, separation and co-localization. In actual applications this is not necessary.

Magnetic separation was performed by manually positioning a permanent magnet for 10 seconds on the side of a 5 mL-capacity vial containing a mixture of MNPs and target antibody in order to concentrate the MNPs so that the supernatant could be removed by pipette. The magnetically captured nanoparticles were rinsed and re-suspended in phosphate buffered saline (PBS, pH 7.4) after which fluorescence emission spectra were acquired to determine the amount of captured AF-mouse IgG. Figure 3.3A shows the emission spectra acquired from the magnetically captured nanoparticles after exposure to four different concentrations of AF-mouse IgG. The dashed lines in Figure 3.3A and 3.3B represent spectra acquired from FL-anti-mouse IgG nanoparticles in the absence of AF-mouse IgG and show no peak at 603 nm as expected.

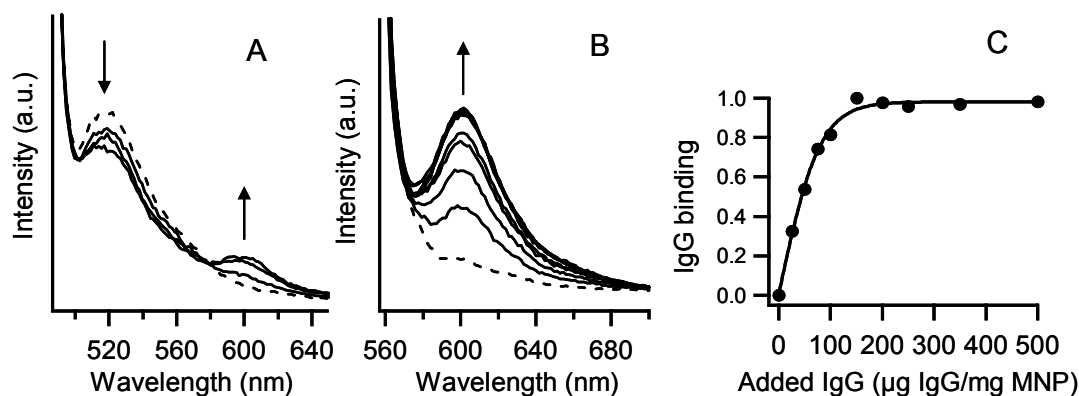


Figure 3.3 Fluorescence analysis of magnetic separations performed on mouse IgG. MNPs were labeled with anti-mouse IgG and used to isolate mouse IgG. To verify the separation, anti-mouse IgG was labeled with fluorescein ($\lambda_{\text{max}}=520$ nm) and mouse IgG was labeled with Alexa Fluor 568 ($\lambda_{\text{max}}=603$ nm). Emission spectra of magnetically isolated MNPs were collected at two excitation wavelengths in panels A and B. (A) Excitation at 480 nm directly excites the fluorescein of anti-mouse IgG. (B) Excitation at 550 nm directly excites the Alexa Fluor label on mouse IgG. The spectra in A and B were acquired from MNPs that were magnetically isolated from solutions of AF-mouse IgG ranging in concentrations from zero (dashed lined) to 500 $\mu\text{g IgG/mg MNP}$. Arrows above the peaks in (A) and (B) indicate the direction of change with increasing concentration of Alexa Fluor-labeled mouse IgG. (C) Amount of magnetically captured Alexa Fluor 568-labeled IgG as monitored by the areas under the fluorescence spectra of (B).

In Figure 3.3A the excitation wavelength used was 480 nm for direct excitation of the FL-anti-mouse IgG. The data show that, as the AF-mouse IgG concentration is increased, a decrease in emission from the immobilized FL-anti-mouse IgG is observed. The decrease in FL emission is accompanied by increasing emission from the AF-mouse IgG. The increasing intensity of the AF fluorescence is due to increased binding in proportion with the added antibody. The quenching of the FL emission with increasing binding is likely due to Förster-type energy transfer in which FL acts as the fluorescence resonance energy transfer (FRET) donor and AF acts as the FRET acceptor. The observed FRET efficiency¹³³ is weak (approx. 15-30%) but indicates that the dyes must be separated by an average distance of less than 10 nm since the calculated Förster distance (dye separation-distance at which energy transfer is 50%) for the dye pair is 6.0 nm. Hence, the presence of energy transfer provides strong evidence that the dyes are co-localized through antibody—antigen interactions.

In Figure 3.3B, emission spectra were acquired from the magnetically isolated particles using direct excitation of the AF dye ($\lambda_{\text{ex}} = 550 \text{ nm}$). Direct excitation of AF-mouse IgG provides better quantification of the amount of captured antibody, and data obtained in this way were used to construct the binding curve shown in Figure 3.3C. The area under the AF peak (590-700 nm) in Figure 3.3B was determined after correction for background and is plotted against the IgG solution concentration in Figure 3.3C to form a binding isotherm. Saturation was reached at 150 μg IgG/mg MNP, nearly the same point as the chemisorption isotherm (160 μg anti-IgG/mg MNP) obtained for the initial immobilization of anti-mouse IgG on the APTES

modified nanoparticles (Figure 3.2). The closely corresponding saturation points of the two isotherms indicate that 1:1 binding is observed between the immobilized anti-mouse IgG and target mouse IgG. If the bound antibody is chemisorbed through a lysine in the F_c domain as suggested in Scheme 3.1, then both F_{ab} regions are available for binding in which case 2:1 binding would be observed. The actual case is presumably more complicated than depicted by Scheme 3.1 since the antibody molecules can react with the surface in a range of orientations due to the occurrence of multiple lysines as suggested by the original chemisorption isotherm in Figure 3.2. Therefore, if multiple orientations exist it may be assumed that some orientations will result in reduced binding, i.e. the ability to bind only one or even zero mouse IgG. The observed 1:1 binding is therefore interpreted as an average value obtained from a distribution of molecular orientations capable of binding zero, one or two IgG molecules and agrees with our proposed model of monolayer coverage composed of randomly oriented anti-mouse IgG. An alternative explanation is that only 50% of the antibody remains active at the surface due to denaturation from surface interactions. A combination of denaturation and packing effects could also be responsible for the diminished activity. The relevant issue, however, is that APTES immobilized antibodies will retain an overall level of 50% activity without the need for extensive surface preparation or biochemical modification of the antibody. Our observation of 50% activity agrees well with values obtained from immobilized antibodies on planar surfaces.¹²⁷ It was noted that nanoparticle precipitation occurs over a period of minutes in the absence of stirring, and this was true for any of our nanoparticle products, regardless of surface chemistry. No change in this behavior

was observed when AF-mouse IgG was captured, indicating that aggregation or solubility is not strongly affected by the changes in surface chemistry used here. Throughout our measurements care was taken to ensure that the samples were well dispersed during acquisition of spectra.

To verify that the antibodies were indeed co-localized, samples were prepared for imaging with confocal microscopy and micro-spectroscopy. In these experiments a drop of magnetically isolated particles were spin coated onto a glass coverslip. Spin coated samples were prepared from magnetically isolated nanoparticles from solutions before and after adding mouse IgG. Figure 3.4A shows a confocal fluorescence micrograph that was acquired from a sample corresponding to the middle of the saturated region in Figure 3.3C (350 μg of added IgG/mg MNP). Spatially-resolved fluorescence spectra were collected from individual points in the fluorescence image by positioning the focal point (370 nm FWHM) of the excitation laser at the desired image locations.

Figure 3.4B shows two spectra that were obtained by averaging individual spectra from 10 different image locations of two different samples. Spectra were averaged to provide an unbiased representation of the sample. The spectrum acquired from nanoparticles in the absence of AF-mouse IgG (green line) shows only the characteristic FL band. The spectrum acquired from nanoparticles that were isolated from mixtures containing AF-mouse IgG (red line), shows emission from both fluorophores indicating that the dye molecules are co-localized. Further evidence for co-localization can be taken from the relative intensities of the two fluorophores. Each of the spectra in Figure 3.4B were acquired with an excitation wavelength of

488 nm and at this wavelength the molar extinction coefficient for FL is approximately 12 times greater than that of AF. Therefore, the enhanced emission of AF relative to FL is noteworthy. A probable explanation for this observation is that the fluorophores undergo energy transfer as suggested by the ensemble spectra of Figure 3.3. The occurrence of energy transfer observed throughout the sample indicates that the two fluorophores are consistently co-localized within 10 nm of each other. This could only occur through specific binding of the immobilized antibody with its target antibody.

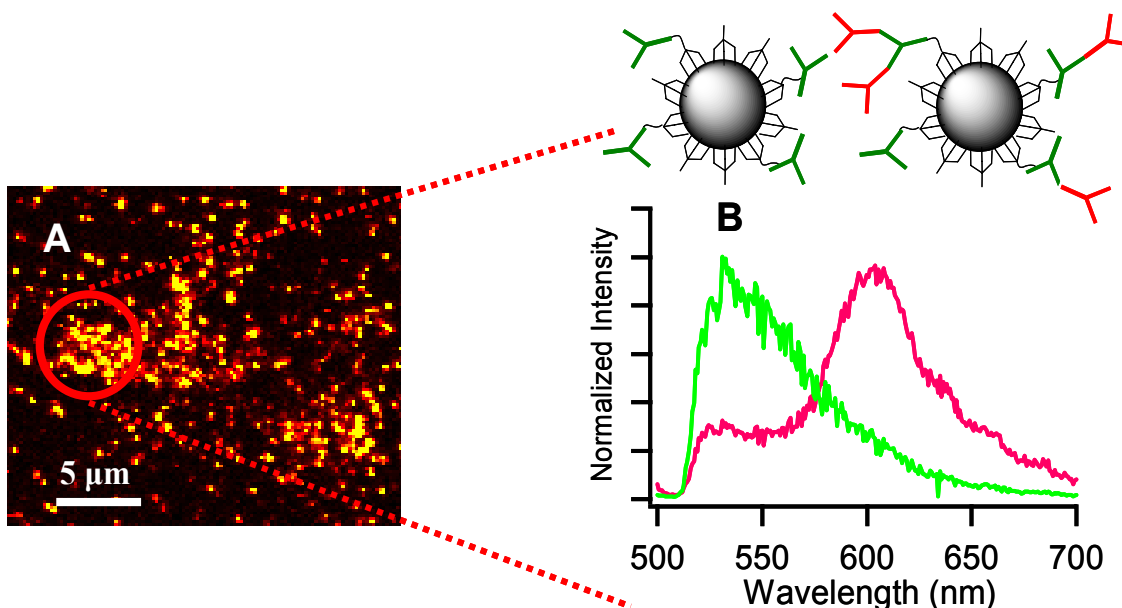


Figure 3.4 Spectra of spin-coated MNPs excited with 488 nm Ar-ion laser. a) Confocal micrograph of spatially segregated fluorescein anti-mouse IgG antibody-immobilized MNPs after mixing with AF-mouse IgG. (b) Normalized emission intensity of fluorescein anti-mouse IgG antibody-immobilized MNPs before (green line; average of 15 spectra from different points of the micrograph) and after (red line; average of 12 spectra) mixing with AF-labeled mouse IgG.

3.5 Conclusion

In this chapter, APTES provides a convenient route for protein immobilization on nanosize iron oxide particles by demonstration of the attachment of anti-IgG antibody on the MNPs. A chemisorption isotherm was acquired using fluorescence-based assays of dye-labeled antibodies. Minimum saturating surface coverage with anti-IgG antibody was determined to be 36%. This corresponds to monolayer coverage by approximately 34 randomly oriented antibodies on an average diameter MNP of 32 nm. Magnetically assisted extraction of the target antibody, mouse IgG, from solution was conducted and results show that the immobilized antibody retains the ability to bind a target antibody. Surface modification of MNPs with activated APTES should provide a convenient platform for sensitive detection and separation of biological entities such as cells,^{123, 134, 135} proteins,^{103, 136, 137} viruses,¹²⁴ and DNA.¹²⁰

Chapter 4: Differential functionalization of SiO₂/TiO₂ mixed nanoparticles: an X-ray photoelectron spectroscopy study

4.1 Abstract

In this chapter differential functionalization of aerosol phase-synthesized SiO₂/TiO₂ mixed nanoparticles is demonstrated via X-ray photoelectron spectroscopy (XPS) analysis. The particles were functionalized using aqueous phase-mediated preferential binding of phenyl phosphonic acids (PPA) to TiO₂ and subsequent binding of trimethyl silyl ((CH₃)₃Si-) groups to the remaining SiO₂ surface. The particles include pure SiO₂ and TiO₂, plus SiO₂/TiO₂ composite nanoparticles with three different mole ratios of Si:Ti = 5:1, 1:1, and 1:5. The analysis of surface chemical components measured via XPS is used to confirm differential functionalization of SiO₂/TiO₂ composite nanoparticles. After aqueous-phase reaction with PPA, SiO₂/TiO₂ mixed nanoparticles and TiO₂ nanoparticles demonstrate 0.05 bound phosphorous molecules per surface Ti molecule, whereas no phosphorous peak is detected on PPA-reacted SiO₂ nanoparticles. 80% ± 10% of the P to Ti ratio is retained after reaction of the PPA-reacted mixed nanoparticles with BSTFA. XPS spectra in C 1s and Ti 2p region indicate the trimethyl silyl group binds to the nanoparticles in the silanation step. PPA bound in tridentate mode may be found not only on the bulk TiO₂ surface but also at the SiO₂-TiO₂ interface.

4.2 Introduction

Differential functionalization of metal-metal,^{4, 5, 39, 88, 138-142} metal-metal oxide,^{3, 12, 37, 38, 112-115} and metal oxide-metal oxide^{6-9, 99} surfaces is useful in biological applications such as the construction of selective molecular assembly patterns^{7, 8, 114} and the fabrication of multifunctional nanostructures^{3-5, 88, 138}. Selective binding of a functional compound to a specific portion of a multi-component surface is crucial to obtain differentially-functionalized heterogeneous surfaces.

Thiol compounds (R-SH) are a typical example of functional molecules which show selectivity in noble metal-metal and noble metal-metal oxide systems due to their specific affinity for noble metals including Au and Ag. In their early pioneering work, Whitesides and collaborators¹¹² demonstrated simultaneous differential functionalization of Au-alumina surface using Au-alkane thiol and alumina-alkane carboxylic acid interaction. Since then, the formation of a self-assembled monolayer of thiols on noble metals has frequently been employed to differentially modify metal-metal^{4, 88, 141} and metal-metal oxide surfaces^{3, 112-115}.

Finding a functionality that can bind selectively to one portion of a metal oxide-metal oxide surface is a highly challenging task, since most functional molecules show a similar binding affinity to different metal oxide surfaces. For example, organosilanes, widely-used inorganic surface-functionalizing compounds, exhibit binding to both areas of SiO₂-metal oxide surfaces.⁶ Recent studies show that organophosphorous compounds are a promising candidate for selective functionalization of SiO₂-metal oxide surfaces¹⁰¹. Textor and collaborators^{7, 8} demonstrated the selective self-assembly of alkane phosphates on the TiO₂ portion of

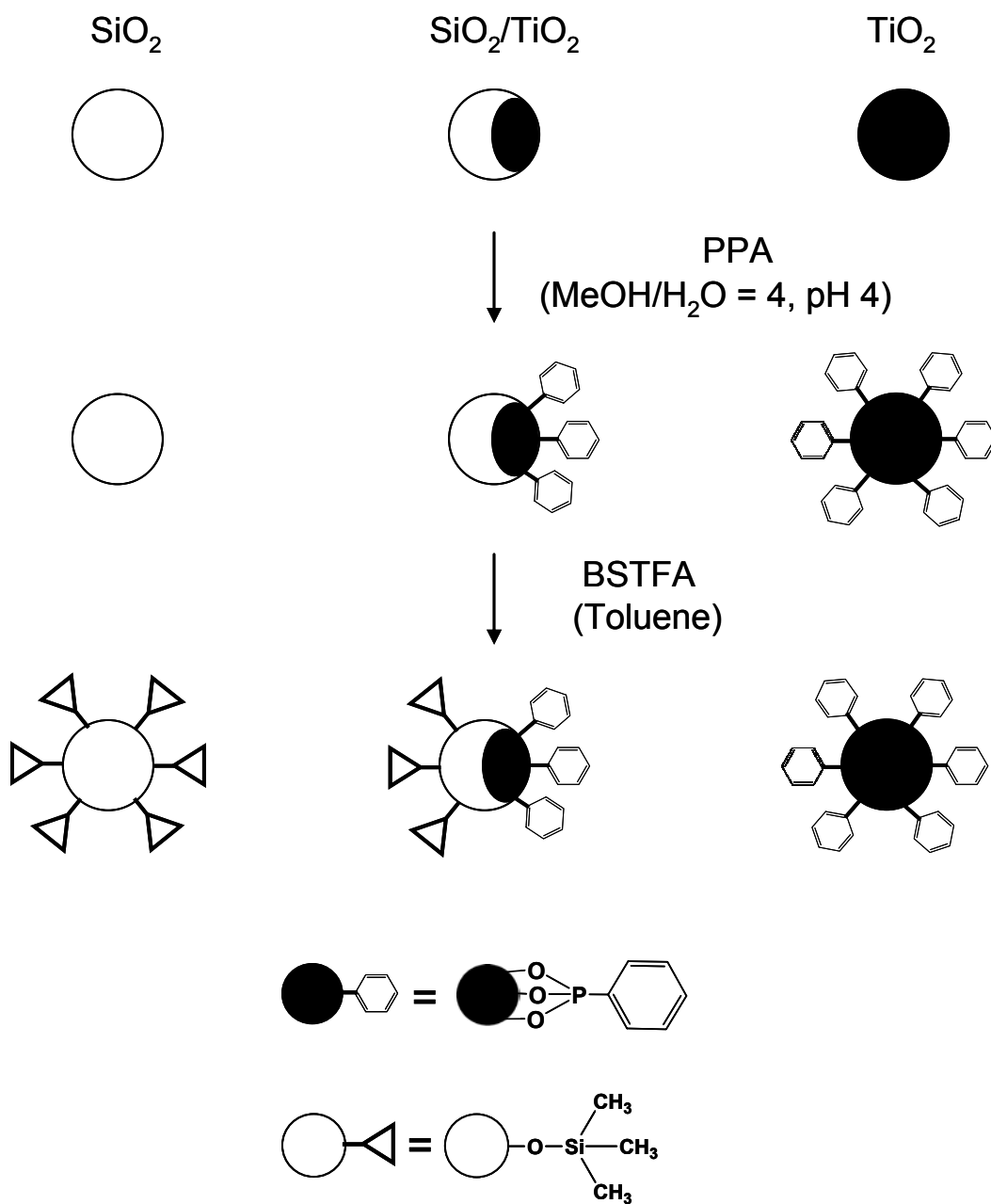
lithographically fabricated TiO₂-SiO₂ surfaces. Subsequent adsorption of poly(L-lysine)-*g*-poly(ethylene glycol) (PLL-*g*-PEG) to the remaining SiO₂ area led to a patterned surface. Proteins were selectively bound to the TiO₂ surface, not to the protein-binding resistant SiO₂ portion by the adsorbed PEG-compounds. Mutin *et al.*^{6,99} illustrated a selective phosphonic acid-binding to the TiO₂ surface of SiO₂-TiO₂ supports. ³¹P solid state nuclear magnetic resonance (NMR) spectra along with scanning Auger electron spectra were consistent, confirming the selective binding between TiO₂ and phosphonic acid. Further treatment of phosphonic acid-bound SiO₂-TiO₂ supports with a trimethylsilyl compound, N,O-bis(trimethylsilyl)trifluoroacetamide (BSTFA), led to formation of Me₃Si-O-Si bonds on the SiO₂ surface according to ²⁹Si solid state NMR spectra.

Multifunctional nanoparticles are desired in many biological applications such as nanoparticle-based cancer treatments¹¹ requiring drug-loading, biobarrier-overcoming, target-recognizing capability and extended stability in the blood stream. Solution-phase synthesized composite nanostructures, such as multi-component metal-metal nanorods,^{4, 5, 88, 141-143} and combined nanoparticles of metal-metal³⁹ and metal-metal oxide^{3, 12}, have been differentially functionalized for biological applications as multifunctional nanoparticles. Research in this Chapter is aimed at differential functionalization of aerosol-phase synthesized SiO₂/TiO₂ mixed nanoparticles via selective binding of phosphonic acids to TiO₂ and subsequent trimethylsilyl group binding to the SiO₂ surface. X-ray photoelectron spectroscopy (XPS) provides both quantitative and qualitative understanding of the sequential differential functionalization process.

4.3 Materials and methods

Phenyl phosphonic acid (PPA; 98%) and N,O-bis(trimethylsilyl)trifluoroacetamide (BSTFA; liquid) were purchased from Aldrich and were used as received. Pure SiO₂ and TiO₂ nanoparticles and SiO₂/TiO₂ mixed nanoparticles with different mole ratios of Si versus Ti were synthesized via an aerosol phase route according to a previously reported method.⁹ Briefly, liquid precursors for SiO₂ and TiO₂, C₆H₁₈OSi₂ (98+%, Aldrich) and TiCl₄ (99.9%, Cerac) respectively, were vaporized by sparging with nitrogen and were carried to a high temperature (~2300 K) premixed methane, nitrogen/ oxygen flame reactor to generate the metal oxide nanoparticles. In the flame, the precursors rapidly oxidize and the particles form by gas-to-particles conversion. The flow rates of the two precursors were controlled for the generation of SiO₂/TiO₂ mixed nanoparticles at a mole ratio of Si versus Ti being roughly 5:1, 1:1, and 1:5. In each flame synthesis of the pure and composite particles, the total concentration of Ti and Si in the flame was maintained at 1.3×10^{-4} mol/L of flame gas at standard temperature and pressure.

Scheme 4.1 demonstrates reaction schemes for reactions of SiO₂ and TiO₂ nanoparticles, and SiO₂/TiO₂ mixed nanoparticles. The metal oxide nanoparticles (MONPs) were reacted first with phenyl phosphonic acids (PPA) in an aqueous solution (MeOH:H₂O = 4:1, v/v; pH 4) using the reported preferential binding of phosphonic acids on TiO₂ versus SiO₂.⁶⁻⁸ BSTFA, a mild silylating agent, was used in the next step of silanation of the PPA-reacted MONPs (MONP-PPA).



Scheme 4.1 Scheme of differential functionalization of SiO_2 , TiO_2 , and $\text{SiO}_2/\text{TiO}_2$ mixed nanoparticles.

Selective modification of SiO₂/TiO₂ mixed nanoparticles with PPA: An aqueous PPA solution was prepared by adding PPA to a mixture of methanol and water (MeOH:H₂O = 4:1 v/v) at 4 mM concentration and adjusting the pH to pH 4. SiO₂, TiO₂ and SiO₂/TiO₂ mixed nanoparticles were added to the PPA solution at 1.0 mg/mL concentration.

After sonication for 10 minutes, the particle-suspended PPA solution was stirred for 15 hours at room temperature. The PPA-reacted MONPs were collected by centrifugation and washed several times thoroughly with mixed solvent of methanol and water (4:1, v/v). The washed nanoparticles were dried at 120 °C for 15 hours in vacuum.

Silanation with BSTFA: Nanoparticles were added to a round bottomed flask and nitrogen was purged to create an inert environment for silanation reaction. Dried toluene was added at 10 mg nanoparticle/ mL toluene. Nanoparticles were suspended by sonicating for 10 minutes. Then, BSTFA was added at a tenth of the added toluene volume. The particle-suspended BSTFA solution in toluene was stirred for 2 hours at room temperature. The reacted nanoparticles were centrifuged and washed five times with toluene. The washed particles were dried at 120 °C overnight in vacuum.

XPS analysis: XPS analysis is described in the methods section of Chapter 3.

Nanoparticles were made in pellet form without any additives for XPS scans to minimize background interference from carbon tape.

4.4 Results and discussion

Figure 4.1 shows morphologies of SiO₂, TiO₂, and SiO₂/TiO₂ mixed nanoparticles at a mole ratio of Si to Ti being 5:1, 1:1, and 1:5 and a TEM image of SiO₂/TiO₂ mixed nanoparticles (Si:Ti = 1:1). The interface between Ti-rich and Si-rich domain shows curvature arising from the difference in surface energies of SiO₂ and TiO₂, 0.3 and 0.5 J m⁻² respectively.⁹ In a previous report on SiO₂/TiO₂ mixed particle synthesis, evidence of Si-O-Ti bonding was detected at 960 cm⁻¹ in Fourier transform infrared spectra of the mixed nanoparticles.⁹ TEM images of SiO₂/TiO₂ nanocomposites with three different mole ratio between Si and Ti are shown in Figure 4.2. The particle size is in the range between 10 and 50 nm.⁹

Figure 4.3 displays XPS-scanned atomic concentrations (%) of Si and Ti, and the ratio of atomic concentration of Si/Ti of bare unreacted MONP, MONP-PPA, and BSTFA-reacted MONP-PPA (MONP-PPA-BSTFA). Mole ratios of Si vs. Ti of SiO₂ nanoparticles, SiO₂/TiO₂ mixed nanoparticles, and TiO₂ nanoparticles are controlled in the particle synthesis step as Si:Ti = 1:0, 5:1, 1:1, 1:5, and 0:1 respectively. XPS-mediated Si atomic concentration (%) of nanoparticles from SiO₂, via SiO₂/TiO₂, to TiO₂ nanoparticles is decreased from 27 to 18, 17, 3.7, and 0, while Ti atomic concentration (%) is increased from 0 to 2.6, 5.9, 10, and 19 respectively. The corresponding XPS-determined atomic concentration ratio of Si vs. Ti is 3.9:1, 2.4:1, and 1:2.9 in the order of increased Ti portion in the mixed nanoparticles. This ratio is roughly maintained in the XPS analysis of MONP-PPA and MONP-PPA-BSTFA (Figure 4.3).

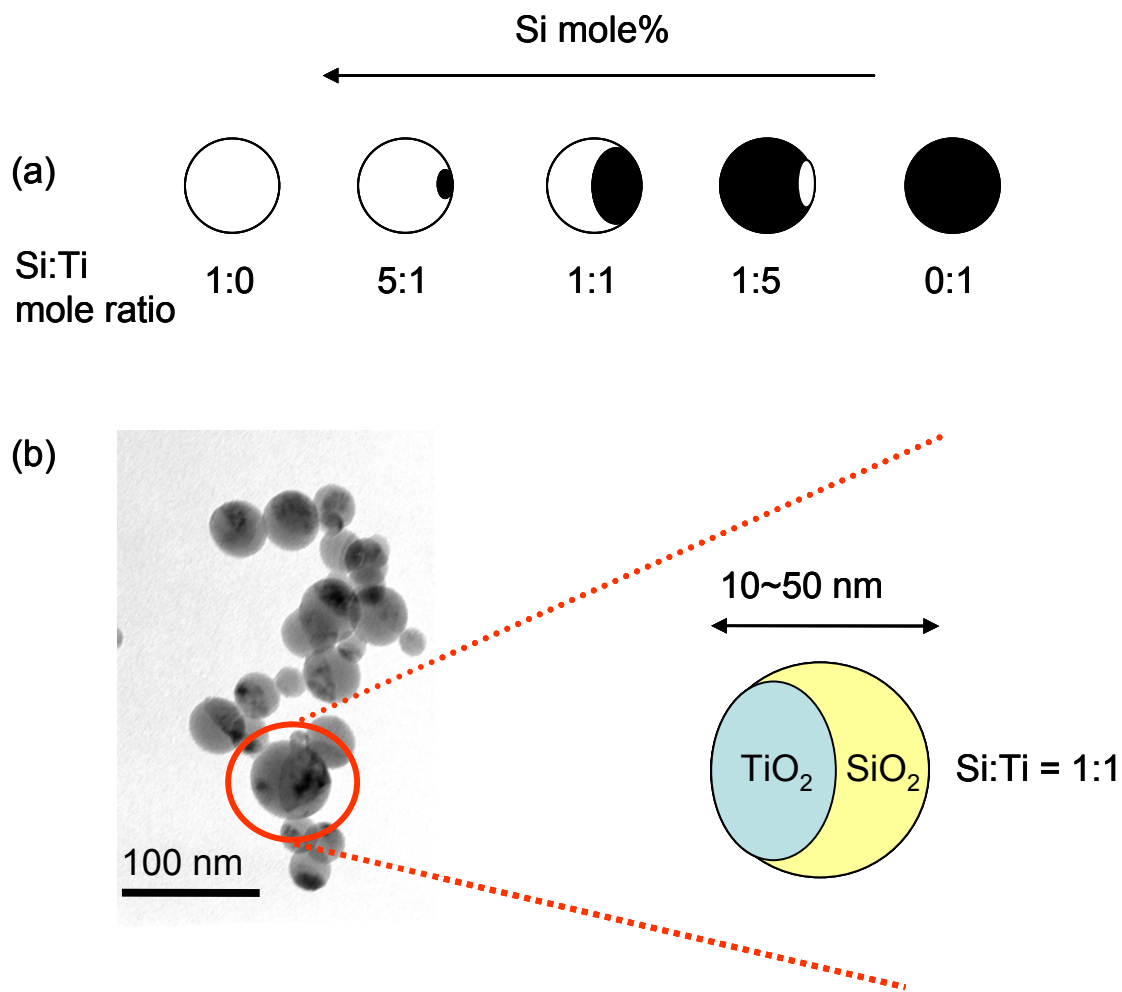


Figure 4.1 (a) Morphologies of SiO₂, TiO₂, and SiO₂/TiO₂ mixed nanoparticles used in this work. (b) TEM of SiO₂/TiO₂ (Si:Ti = 1:1) mixed nanoparticles.

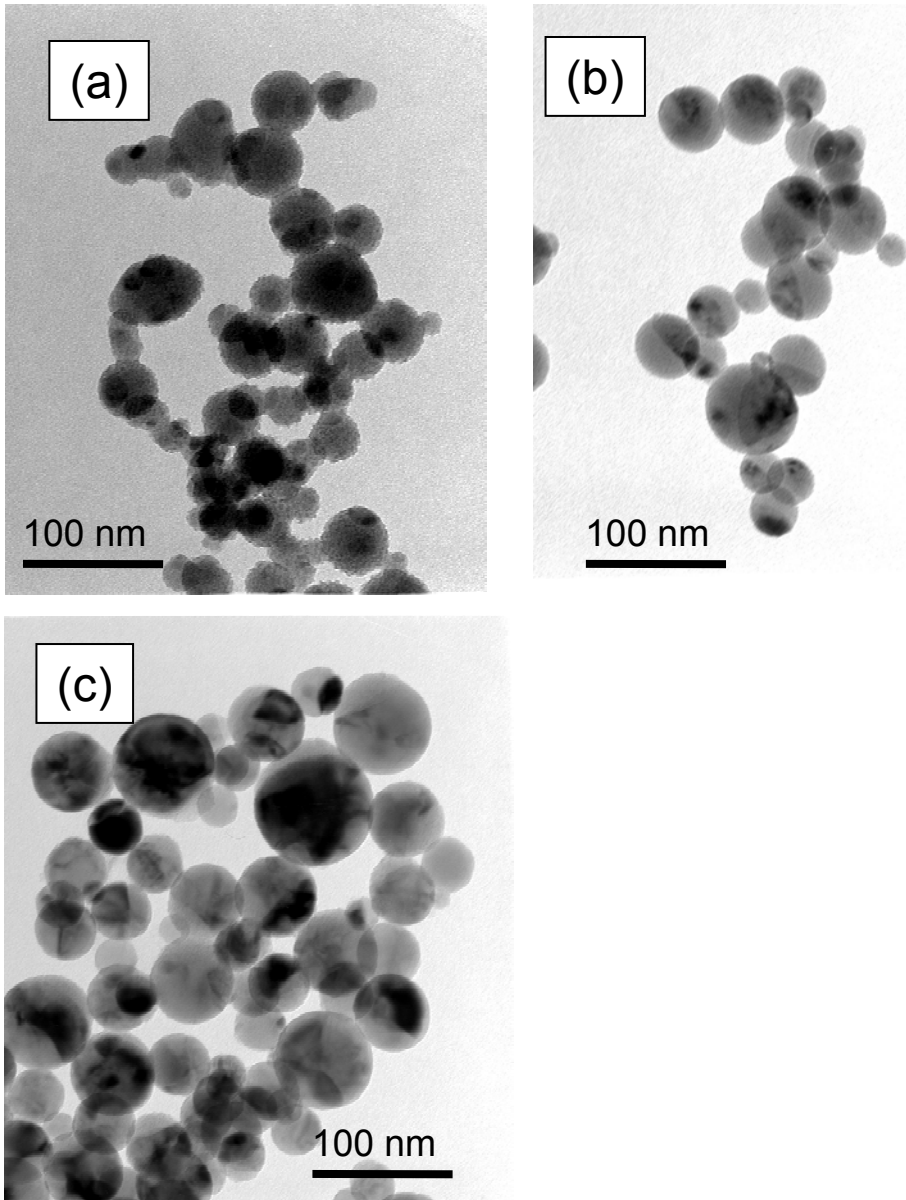


Figure 4.2 TEM of SiO₂/TiO₂ nanocomposites at different ratios of Si and Ti. The dark portion is TiO₂. (a) Si:Ti = 5:1, (b) Si:Ti = 1:1, (c) Si:Ti = 1:5.

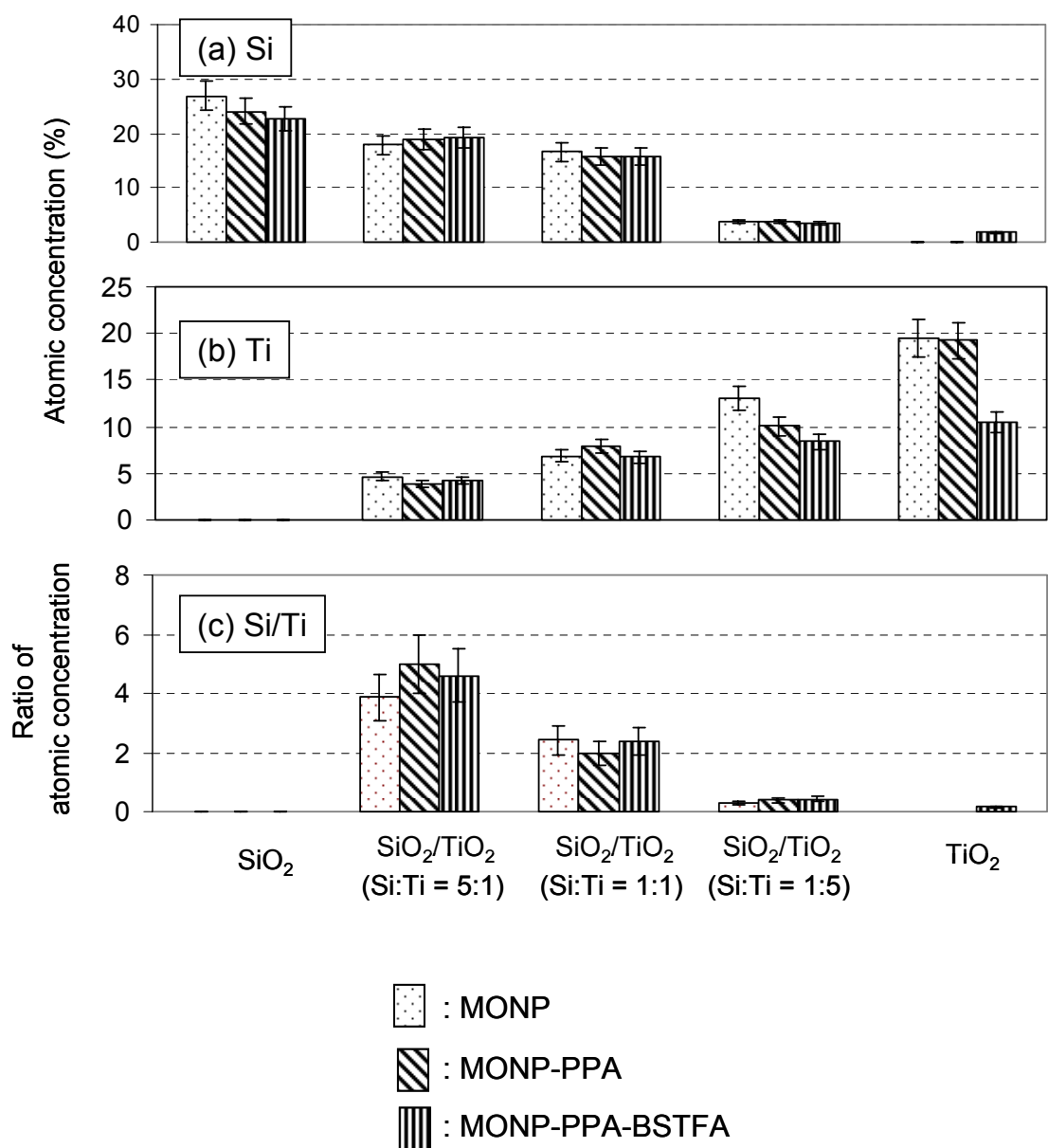


Figure 4.3 Atomic concentration (%) of (a) Si and (b) Ti, and (c) the ratio of Ti versus Si atomic concentration in the XPS based upon analysis of SiO_2 , TiO_2 , and $\text{SiO}_2/\text{TiO}_2$ mixed nanoparticles.

The discrepancies of the XPS-determined ratios from the mole ratios in particle synthesis step are likely coming from three factors: i) In the particle synthesis process, there is some uncertainty in the flow rates of the precursors. Since the precursor delivery rate was measured gravimetrically, 5-10% of uncertainty is involved in determination of the precursor flow rates. ii) As the TEM image in Figure 4.1(b) shows, SiO₂/TiO₂ mixed nanoparticles with a mole ratio of Si:Ti = 1:1 do not display a perfect hemispherical-split but rather a bigger surface area of SiO₂. Since SiO₂ (0.3 J m⁻²) has lower surface tension than TiO₂ (0.5 J m⁻²), SiO₂ may wet and have more surface area. iii) Because of the surface-sensitive character of XPS, XPS-mediated determination of the Si/Ti ratio is likely to be different from the bulk ratio. When the XPS signal detector is normal to the sampling surface as the case in this research, the escape depth of photoelectrons is given as three times the photoelectron mean free path. The photoelectron mean free path is ~1.5 nm for both Si and Ti, which leads to the value of the escape depth being ~4.5 nm. Considering the size range of the nanocomposites between 10 and 50 nm, the XPS results can be considered to be surface-specific rather than a determination of the bulk chemical composition of the nanocomposites.

Figure 4.4 shows the phosphorous 2p region of bare MONPs and MONPs-PPA. Phosphorous can be used as an indicator of PPA binding to MONPs, since phosphorous does not exist on bare MONPs used in this work. As expected, phosphorous of bare unreacted MONPs is not detected in the P 2p region of XPS.

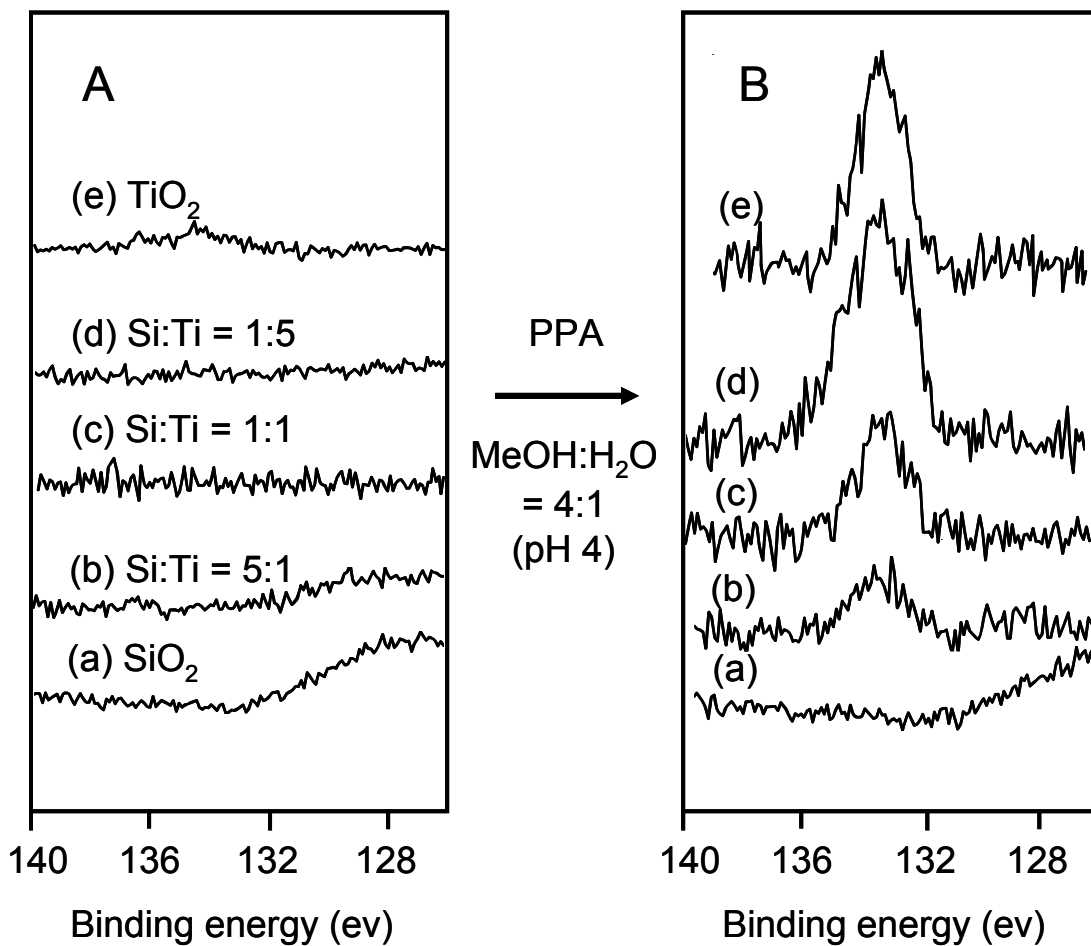


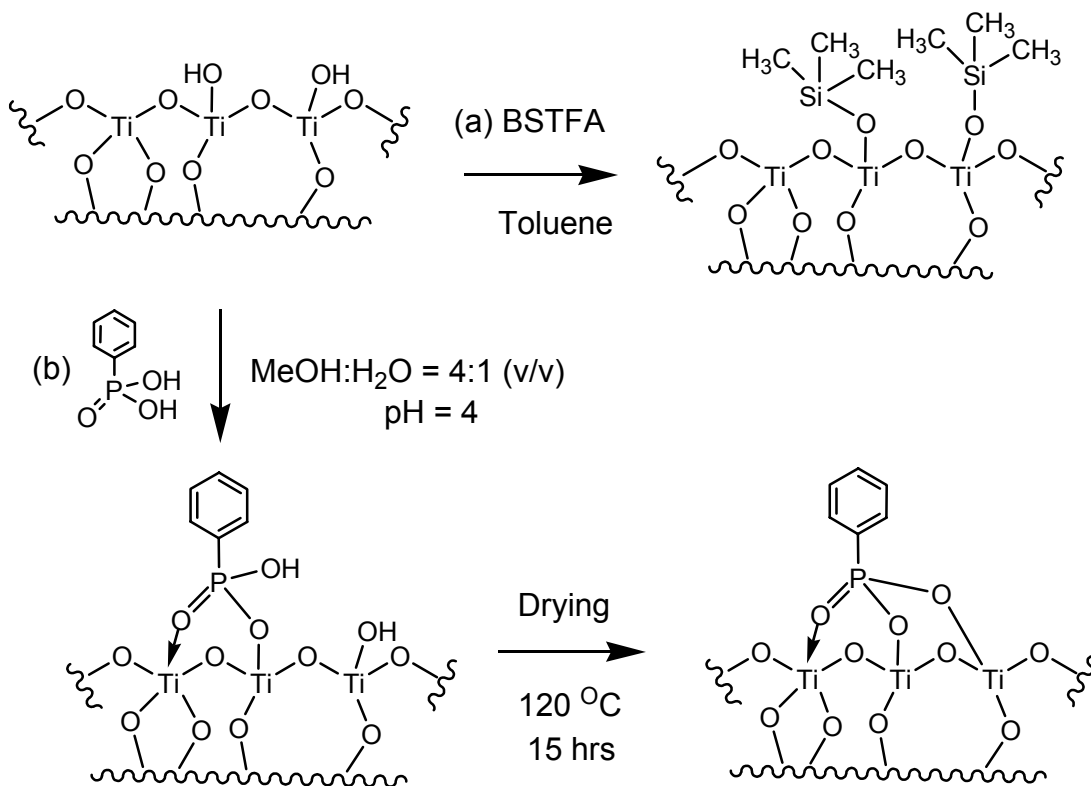
Figure 4.4 Phosphorous 2p region of XPS scan of (a) SiO₂ nanoparticles, (b)-(d) SiO₂/TiO₂ mixed nanoparticles, and (e) TiO₂ nanoparticles. A: Bare unreacted nanoparticles, B: Nanoparticles after reaction with phenyl phosphonic acid (PPA).

After reaction of SiO₂ nanoparticles with PPA, no peak in the P 2p region of XPS is seen. However, when mixed SiO₂/TiO₂ nanoparticles were reacted with PPA, a distinctive P 2p peak appeared at around 134 eV.^{100, 144} In general, the P 2p peak grows in intensity and signal to noise ratio as the mole ratio of Ti versus Si is increased. Comparison of the P 2p XPS spectra before versus after PPA reaction clearly demonstrates selective phosphonic acid-binding to TiO₂ of the mixed surfaces under aqueous reaction conditions. This preferential binding is due to the higher stability of Ti-O-P bonds to hydrolysis than Si-O-P bonds in an aqueous environment.^{6, 99, 101} Si-O-P bonds are formed in organic solvents. In previously published reports, SiO₂-phosphonic acid peaks were detected in ³¹P solid-state NMR spectra in an organic aprotic solvent such as hexane¹⁴⁵ or toluene⁶. However, the phosphorous peaks disappeared under aqueous reaction conditions due to the labile nature of Si-O-P bonds to hydrolysis.^{6, 99} Schematic representations of PPA reaction with TiO₂ and SiO₂ surfaces are given in Schemes 4.2 (b) and 4.3 (b). The TiO₂-PPA binding mode is described as predominantly tridentate (RP(OTi)₃ species) by ¹⁷O solid-state NMR spectra¹⁴⁶ and ³¹P solid state NMR spectra study⁶. The tridentate binding of PPA to TiO₂ surface modifies coordination number of Ti atoms on the surface, whereas trimethyl silyl group-binding by BSTFA reaction does not (Scheme 4.2). In a report of the use of PPA to modify TiO₂ surfaces, this modified coordination number of Ti led to a reduced catalytic activity of the PPA-bound TiO₂ surface due to decreased Lewis acid character.⁶

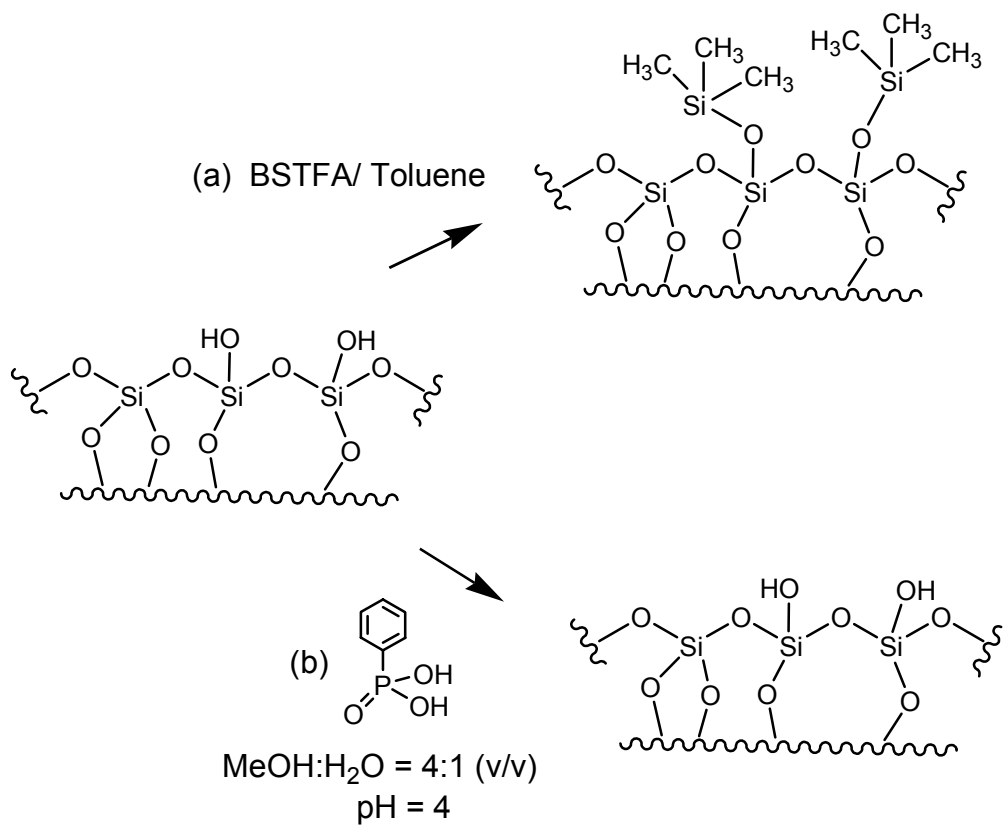
A minor peak of ³¹P solid state NMR spectra of TiO₂-PPA was assigned to the presence of the surface-bound phosphonic acids with other binding modes or in a

distorted geometry.^{6, 146} These features likely lead to the appearance of another pair of Ti 2p peak of small intensity in XPS of TiO₂-PPA, while trimethyl silyl group binding to TiO₂ nanoparticles does not change the shape and the position of Ti 2p peaks (Figure 4.5).

Figure 4.6 shows the atomic concentration (%) of the P 2p peaks and the ratio of atomic concentration of P 2p peak/Ti 2p peaks of MONP-PPA and MONP-PPA-BSTFA respectively. The atomic concentration (%) of P of MONP-PPA grows from 0 for pure SiO₂ nanoparticles to 0.19, 0.17, and 0.99 with the increasing percentage of surface Ti atoms of the mixed nanoparticles (Figure 4.6(a)). The P atomic concentration of pure TiO₂ nanoparticles is 0.84%.



Scheme 4.2 Schematic representation of surface modification of TiO₂ nanoparticles with (a) BSTFA and (b) PPA.



Scheme 4.3 Schematic representation of surface modification of SiO₂ nanoparticles with (a) BSTFA and (b) PPA.

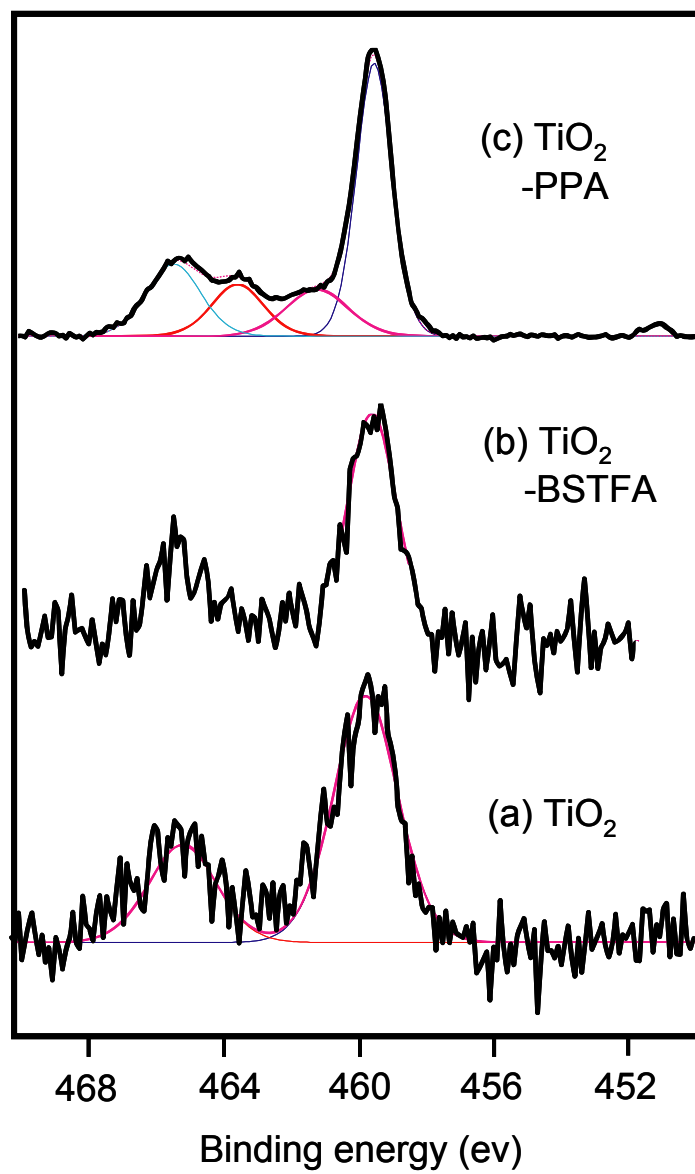


Figure 4.5 Ti 2p XPS spectra of (a) bare unreacted TiO₂, (b) BSTFA-reacted TiO₂, and (c) PPA-reacted TiO₂ nanoparticles.

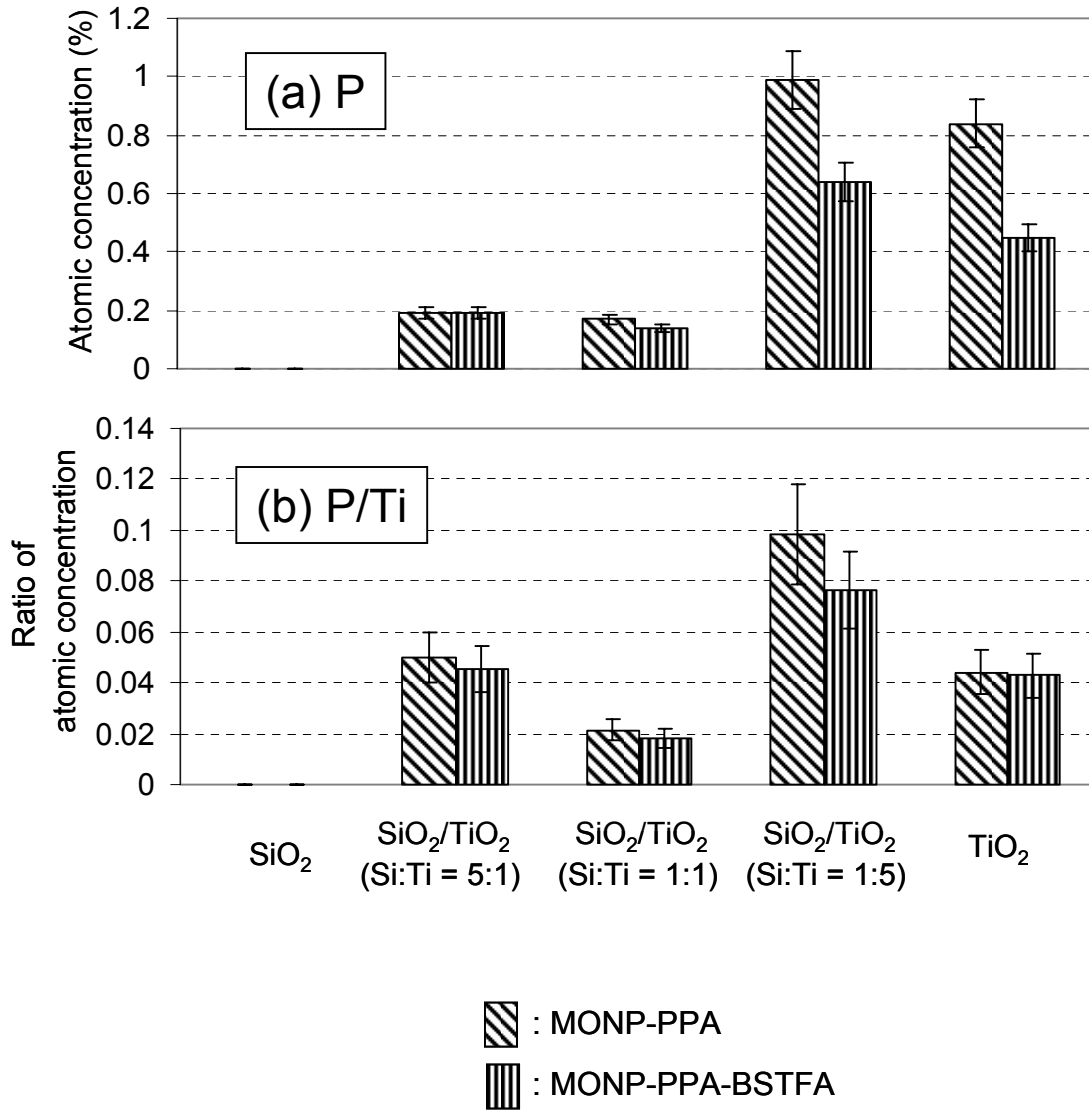


Figure 4.6 (a) Atomic concentration (%) of phosphorous 2p (P 2p) peaks and (b) the ratio of atomic concentration of P peaks versus atomic concentration of Ti peaks.

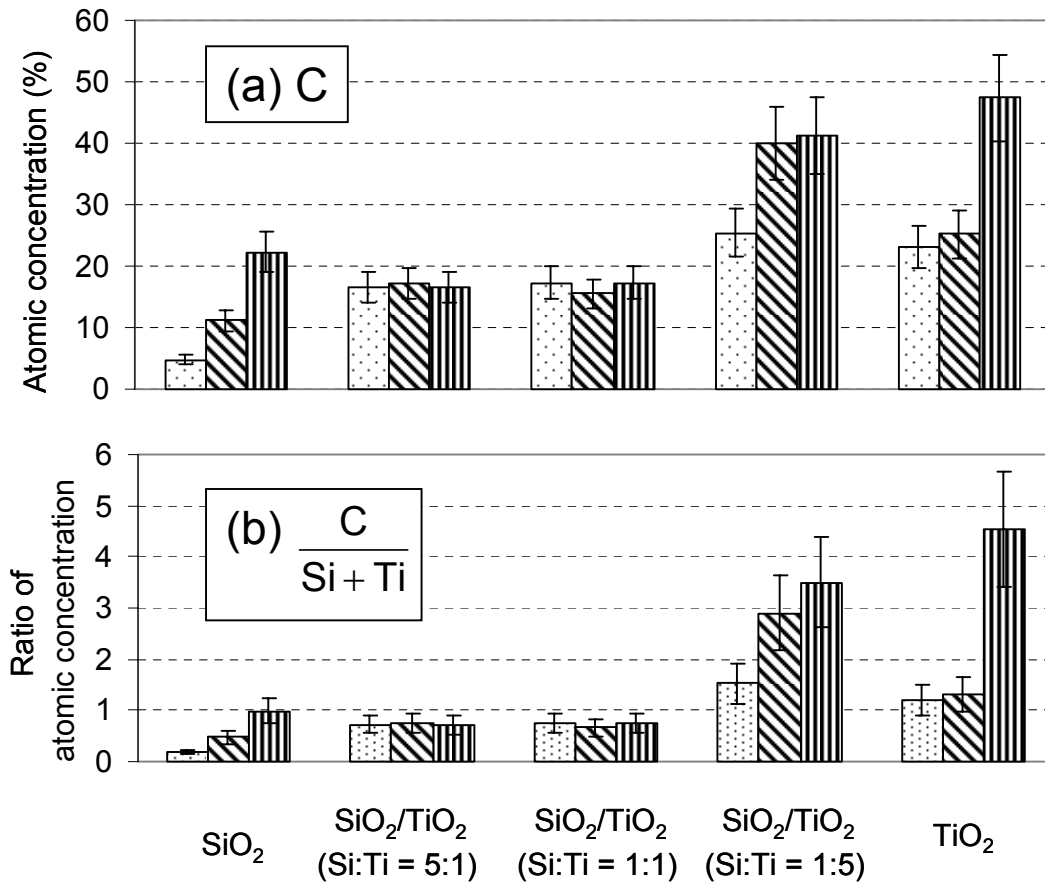
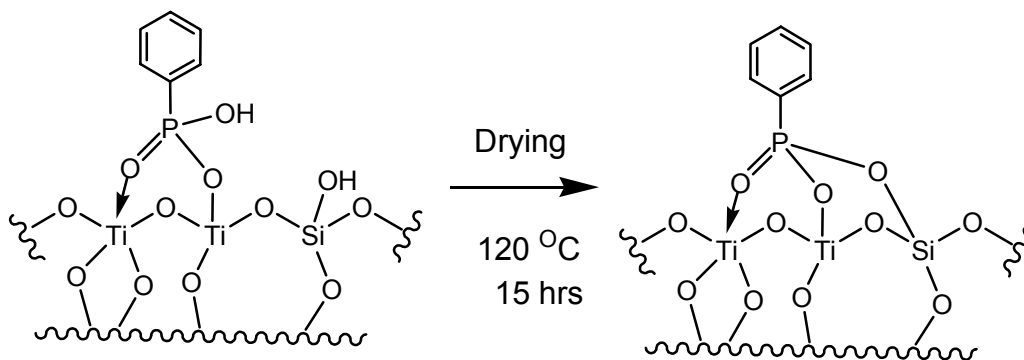


Figure 4.7 (a) Atomic concentration (%) of carbon 1s (C 1s) peaks and (b) the atomic concentration ratio of C 1s peaks versus (Si 2p + Ti 2p) peaks.

When the atomic concentration of the P 2p peak is divided by the atomic concentration of the Ti 2p peak, the XPS data in scanning of phosphorous are more comparable with each other as the Ti 2p peak can be used as an internal standard. On average, 0.05 phosphorous atoms are bound per one Ti atom (Figure 4.6(b)). The binding number of P per Ti is 0, 0.050, 0.021, 0.099, and 0.044 as the presence of Ti on the nanoparticles is increased from SiO₂ to SiO₂/TiO₂ and TiO₂ nanoparticles. Considering the dominant tridentate binding nature of PPA to TiO₂ and the binding ratio of P/Ti being 0.044, the percentage of Ti occupied by PPA is 13% on TiO₂-PPA. Fluctuation of the ratio is likely from different initial conditions of the particles, for example different amount of carbon contamination on bare unreacted nanoparticles (Figure 4.7(a)). In the case of mixed nanoparticles of mole ratio of Si:Ti = 5:1 and 1:5, the binding ratio of P/Ti (0.050 and 0.099) is greater than the ratio of pure TiO₂ nanoparticles (0.044). This observed phenomena can be partially ascribed to the formation of P-O-Si bonds at the SiO₂-TiO₂ interface of SiO₂/TiO₂ mixed nanoparticles (Scheme 4.4).⁶



Scheme 4.4 Formation of phenyl-P(OTi)₂(OSi) bonds at the interface of TiO₂ and SiO₂ portion of SiO₂/TiO₂ mixed nanoparticles.

Mutin *et al.*⁶ reported a significant increase of peak width from TiO₂-PPA surface to SiO₂/TiO₂-PPA surface in their ³¹P solid state NMR spectra. In their hypothesis, the increased peak width was explained by the formation of P-O-Si bonds during the drying process at the boundary between SiO₂ and TiO₂ in addition to the formation of P-O-Ti bonds (Scheme 4.4). This hypothesis was proved by a significant suppression of the ³¹P NMR peak due to hydrolysis of some of the P-O-Si bonds, when the phosphonic acid-bound SiO₂/TiO₂ surface was immersed in a mixture of methanol and water. The presence of P-O-Si bonds was also used to explain larger surface coverage (25%) by phosphonic acids on phosphonic acid-reacted SiO₂-TiO₂ surface than the actual mole percentage of Ti (10 mole %) on the mixed surface.

The phosphorous peak is maintained after silanation reaction with BSTFA, though atomic concentration ratio of P/Ti is decreased by 20% ± 10% on mixed nanoparticles (Figure 4.6(b)). This decrease can be explained by the combined effect of the following: (i) The hydrolysis of the Ti-O-Si bond may lead to instability and even destruction of PPA binding at the interface between SiO₂ and TiO₂ and elimination of PPA on the surface of TiO₂. The higher retention of PPA binding to pure TiO₂ nanoparticles after the BSTFA treatment demonstrates that the tridentate binding mode between PPA and the TiO₂ surface contributes to the stability of the bonds. (ii) Suspension in an organic solvent, toluene, can displace the phosphorous bonding. The effect of toluene in the step of BSTFA reaction was investigated. TiO₂-PPA particles were suspended in toluene without the addition of BSFTA for the

same time as in the case of BSTFA reaction and characterized with XPS. The results are shown in Table 4.1.

Table 4.1 Effect of solvent (toluene) in the BSTFA reaction step: atomic concentration (%).

	Before toluene treatment	After toluene treatment
Ti	14.2 ± 1.4	14.8 ± 1.5
P	0.66 ± 0.07	0.61 ± 0.06
P/Ti	0.047 ± 0.005	0.041 ± 0.004

Phosphorous binding was decreased 12% after suspension in toluene.

Loosely-bound PPA in mono- and bi-dentate binding mode and in distorted tri-dentate binding mode was likely displaced in suspension in an organic solvent.

Organosilanes such as BSTFA bind to both SiO₂ and TiO₂ surfaces. Si was not detected on bare TiO₂ and TiO₂-PPA in XPS spectra (Figure 4.3). Trimethyl silyl group binding to TiO₂-PPA in BSTFA reaction led to the appearance of Si 2p peaks at a Si/Ti ratio of 0.16.

Figure 4.7 demonstrates XPS results for the carbon 1s region of MONP, MONP-PPA, and MONP-PPA-BSTFA. Bare MONPs display carbon

contaminations.^{100, 108, 147} Intensive cleaning of the TiO₂ surface did not remove carbon contamination completely in a previous report of XPS characterization, since carbon contamination is unavoidable in practice on ambient air-exposed inorganic surfaces.¹⁰⁰ In general, the amount of carbon contamination increases from 4.8% of atomic concentration up to 25%, as the Ti portion increases from SiO₂ to SiO₂/TiO₂, and to TiO₂ nanoparticles. Increase of surface-bound carbon is evident in PPA-reacted SiO₂/TiO₂ (Si:Ti = 1:5) mixed nanoparticles because of the largest amount of P at a ratio of P/Ti being 0.099 (Figure 4.6(b)). Binding of PPA accounts for the increase of 0.6 carbons per Ti out of the observed increase of 1.4 carbons per Ti. The other portion of carbon increase on the mixed particles along with increase of carbon from 0.18 to 0.47 carbons per Si on SiO₂ nanoparticles is likely from adsorption of methanol from solution. The lack of a distinctive increase in carbon on the surface of other particles may be attributed to the uncertainty involved with different amounts of carbon contamination. Pure nanoparticles demonstrate noticeable trimethyl silyl group binding to MONP-PPA, as the C/Si ratio is increased from 0.47 to 0.99 on SiO₂ nanoparticles and from 1.3 to 4.5 on TiO₂ nanoparticles. 0.5 out of the 3.2 carbon number increase per Ti on TiO₂ nanoparticles is attributed to the presence of trimethyl silyl binding, since the Si/Ti ratio was increased from 0 to 0.17 (Figure 4.3). The other portion of the increase may be related to physisorption of BSTFA, degraded parts of BSTFA, and toluene.

Note that a minor pair of peaks appears on a Ti 2p peak scan of TiO₂-PPA compared with the peak of bare TiO₂, while XPS spectra of TiO₂-BSTFA in the Ti 2p region does not exhibit any change in peak shape. (Figure 4.5) A similar trend is

observed with Ti 2p spectra of SiO₂/TiO₂-PPA and SiO₂/TiO₂-PPA-BSTFA (Figure 4.8). A pair of minor peaks, a 2p 3/2 peak and a 1/2 peak of Ti, vanishes with BSTFA reaction. In addition to the partial hydrolysis of P-O-Si bonds addressed previously in the text, this phenomenon likely accounts for the displacement of loosely bound PPA molecules with bond modes other than undistorted tridentate binding and with distorted bonds, as discussed in the description of the 12% decrease of P/Ti ratio by suspension of TiO₂-PPA in toluene.

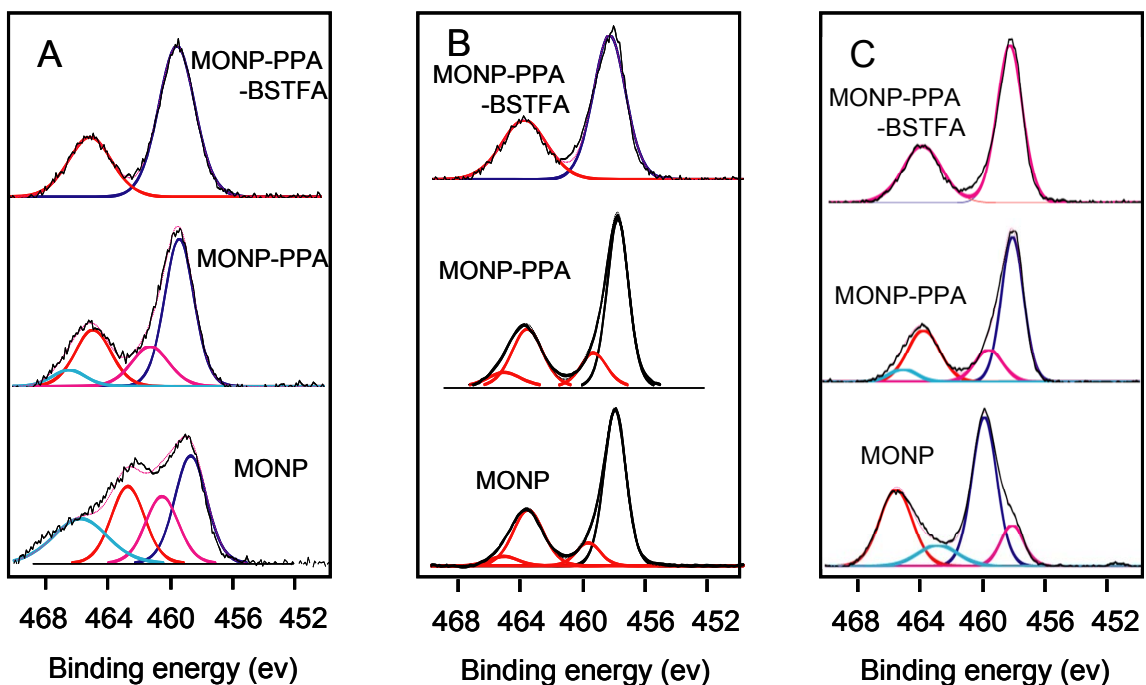


Figure 4.8 Ti 2p spectra of SiO₂/TiO₂ mixed nanoparticles. Si:Ti = 5:1 (A), 1:1 (B), and 1:5 (C).

4.5 Conclusions

This study demonstrates differential functionalization of SiO₂/TiO₂ mixed nanoparticles via a preferential binding of PPA to TiO₂ portion in an aqueous solution and a subsequent reaction of trimethyl silyl groups to the remaining surface. For understanding of the effect of surface portion of TiO₂ on differential functionalization, three different SiO₂/TiO₂ mixed nanoparticles were used with approximate mole ratios of Si:Ti = 5:1, 1:1, and 1:5. XPS analysis of Si 2p and Ti 2p region displays mole ratios of Si:Ti = 3.9:1, 2.4:1, and 1:2.9 respectively. The differences likely arise from uncertainties in determination of mole ratios in particle generation step, the fact that XPS investigates surface rather than bulk chemical compositions of the materials, and possibility of interferences from carbon tape background. Detection of a P 2p peak after PPA reaction can be convincing evidence of PPA binding to the surface, since a P 2p peak does not appear in bare unreacted particles. PPA-reacted SiO₂ particles do not exhibit a P 2p peak, whereas all the other TiO₂-included particles display the appearance of a P 2p peak in XPS spectra after the reaction with PPA. This preferential binding of PPA to TiO₂ vs. SiO₂ surface derives from the much higher stability of Ti-O-P bond to hydrolysis than Si-O-P bond. The averaged number of binding of P per Ti is 0.05, which is accountable for 0.15 carbon binding per Ti in consideration for previously reported tridentate binding mode of PPA to TiO₂. After trimethyl silyl group binding to the surface, the P/Ti ratio is retained at 80% ± 10% for SiO₂/TiO₂ mixed nanoparticles, while 98% of P/Ti ratio of TiO₂ nanoparticles is maintained. The displacement of P at 20% ± 10% level for the mixed nanoparticles is likely due to existence of Si-O-P bonds at the interface between SiO₂

and TiO₂ and hydrolysis of the labile bond in silanation, along with removal of loosely bound PPA. Si 2p XPS spectra of TiO₂ nanoparticles demonstrates trimethyl silyl group binding to PPA-reacted TiO₂. In addition to this silanation to TiO₂, C 1s spectra and Ti 2p spectra are indicative of trimethyl silyl group binding to the mixed nanoparticles. A variety of phosphorous compounds containing terminal functional groups such as –OH,^{100, 101} –SH,¹⁴⁸ and –COOH^{149, 150} are available. The demonstrated differential functionalization of SiO₂/TiO₂ nanoparticles herein and the presence of diverse functional phosphorous compounds together with well-established silanation chemistry provide a promising opportunity for the use of the mixed nanoparticles as multifunctional nanoparticles for biological applications.

Chapter 5: X-ray scattering study of the interactions between magnetic nanoparticles and living cell membranes

5.1 Abstract

Magnetic nanoparticles (MNPs) have found increased applicability in drug delivery, cancer treatment, and immunoassays. There is a need for an improved understanding of how MNPs interact with living cell membranes in applied magnetic fields to use them effectively. The interactions between *Escherichia coli* (*E. coli*) and SiO₂/γ-Fe₂O₃ composite particles in magnetic fields were studied using X-ray scattering (XRS). Magnetic field strengths up to 423 mT were applied to the samples to see the effects of the magnetic fields on the *E. coli* membranes in the presence of the magnetic particles in the cell cultures. X-ray scattering results from continuous cultures of *E. coli* showed two peaks, a sharp peak at $q = 0.528 \text{ \AA}^{-1}$ (1.189 nm) up to 362 mT of magnetic field strength and a diffuse one at $q = 0.612 \text{ \AA}^{-1}$ (1.027 nm). The sharp peak was shifted to the smaller side of q when magnetic particles were added and the magnitude of the applied magnetic field strength was increased from 227 mT to 298 mT, to 362 mT, whereas the diffuse peak did not change. A critical magnetic field strength at which the sharp peak disappears was found at 362 mT.

5.2 Introduction

The interactions between magnetic nanoparticles (MNPs) and cells in magnetic fields must be understood to learn to control technologies important to the fields of medicine and biotechnology.^{122, 134, 135, 151-156} Such applications include the ability of the MNPs to be used to deliver drugs effectively or to kill tumor cells by local heating from an alternating current magnetic field.^{122, 152-154} Physical model systems using phospholipid bilayers mimicking a cellular membrane have been investigated to understand the interactions between MNPs and the lipid bilayers.^{10, 157-161} In studies using a lyotropic lamellar phase, a periodic stack, which ranged from 20 to 40 nm in thickness with water and a suspension of γ -Fe₂O₃ nanoparticles in cyclohexane, was observed.^{157-159, 161} Particles adsorbed on the membranes rotated in the presence of a magnetic field, which resulted in a distortion of the lamellar structure. A change in birefringence was determined using a polarizing microscope¹⁵⁷ or a polarized He-Ne laser,¹⁶¹ whereas X-ray scattering was used to measure the layer separation and the rotation angle of the layer molecules in the changing magnetic field.¹⁰ This rotation of the lipid layers could potentially be done with the lipid layers that constitute the cell membranes or walls.

Escherichia coli (*E. coli*) belongs to the class of gram negative bacteria, which have an outer membrane as well as a plasma membrane. The lipid membranes extracted from *E. coli* cellular membranes have been of great interest, and have been used as a model system to test different interactions. X-ray scattering (XRS) was one of the important tools to investigate the property of the lipid membranes extracted from *E. coli*.¹⁶²⁻¹⁶⁸ In their paper, Esfahani *et al.*¹⁶² found that studies of extracted

lipid membranes give results that are different from those of the lipid components of intact membranes due to the presence of proteins and other structural molecules in intact membranes. Recently, the interaction of gramicidin, an antimicrobial peptide, with the lipid bilayers membranes generated from *E. coli* membrane lipids was investigated using X-ray scattering along with ^{31}P -NMR.^{169, 170} A study of the interactions between MNPs and *E. coli* cellular membranes has not been reported to date. A study of living cells is needed to determine the effectiveness of using MNPs to deliver drugs or to kill tumor cells.^{122, 152-154} In this work, the cellular membranes of living cells, *E. coli*, were studied instead of artificial phospholipid bilayers or membranes of lipids extracted from the cells. X-rays were employed as a tool to understand changes in the *E. coli* membrane bilayers with $\text{SiO}_2/\gamma\text{-Fe}_2\text{O}_3$ composite nanoparticles under the influence of the applied magnetic fields.

5.3 Methods

5.3.1 Magnetic nanoparticles

The unagglomerated $\text{SiO}_2/\gamma\text{-Fe}_2\text{O}_3$ particles were synthesized from hexamethyl disiloxane and iron pentacarbonyl via a gas phase approach in a premixed aerosol flame reactor, where Si and Fe were mixed at a 1:1 mole ratio.⁹ A transmission electron microscope image of a typical particle is shown in Figure 5.1.

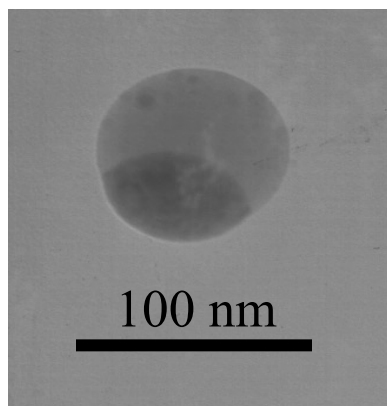


Figure 5.1 Transmission electron microscope image of a $\text{SiO}_2/\gamma\text{-Fe}_2\text{O}_3$ particle. The dark region of the particle corresponds to $\gamma\text{-Fe}_2\text{O}_3$ and the light region is amorphous silica.

The dark region corresponds to iron oxide ($\gamma\text{-Fe}_2\text{O}_3$) whereas the light region is amorphous silica. The iron oxide portion of the particle imparts magnetic properties, whereas the silica surface provides the particle with the potential for surface modification. $\text{SiO}_2/\gamma\text{-Fe}_2\text{O}_3$ composite particles were used as MNPs, ranging from 20 to 100 nm in particle size. The distribution of particle sizes as measured by TEM can be seen in Figure 5.2a. The particles were sonicated to reduce agglomeration before being added to the growth medium of *E. coli*. According to dynamic light scattering, they likely agglomerate again as a function of time during the course of the experiment (see Figure 5.2b). Scattering from the cell in the region between 9 and 20 nm due to the presence of the particles is investigated. The experiments do not measure interactions at the 400 nm level.

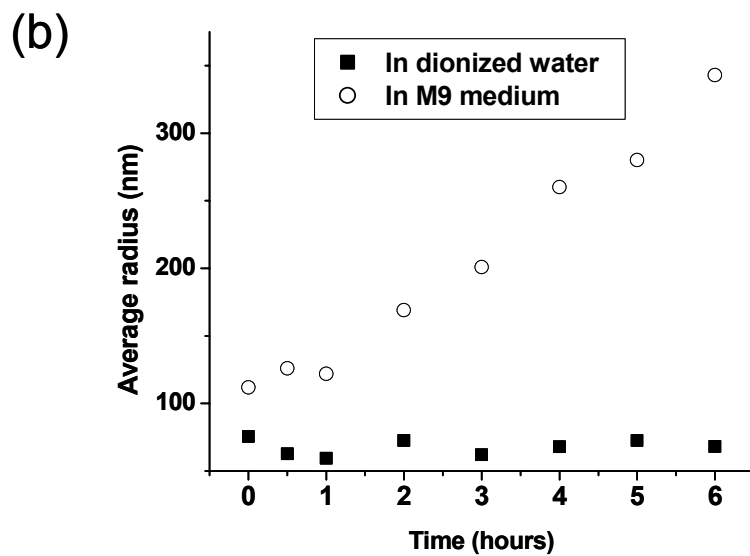
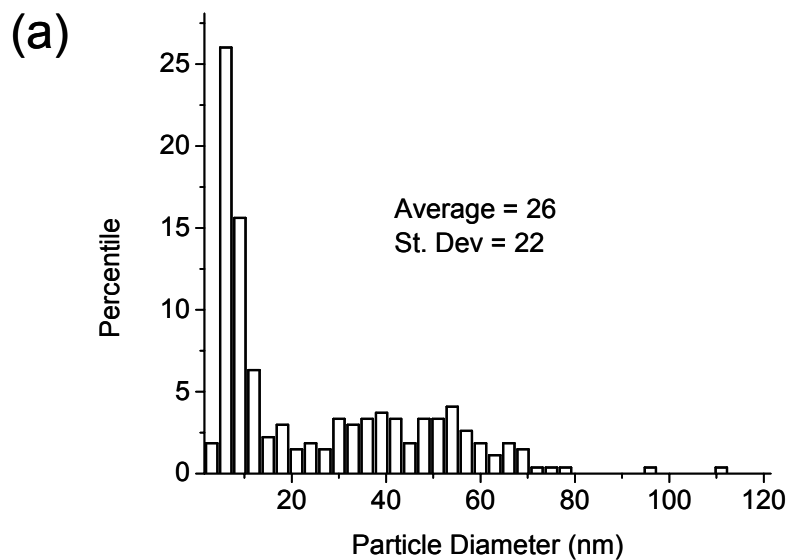


Figure 5.2 (a) Distribution of particle sizes as measured using TEM. (b) Agglomeration of the particles as a function of time in the M9 medium.

Batch cultures of *E. coli* were performed in our group to see if the SiO₂/γ-Fe₂O₃ particles have any inhibitory effect on the growth of the cells. According to the results¹⁷¹ not presented here, these particles have no measurable effect on the growth of *E. coli* up to the particle concentration of 44 mg l⁻¹. The final concentration of the particles in this report was 40 mg l⁻¹ in *E. coli* growth medium, taken under the maximum particle concentration in the toxicity test of the particles upon *E. coli*.

5.3.2 Biological system

The bacteria were grown at 37 °C in modified M9 medium, where amounts of Ca and Mg in the medium were doubled to those in M9 medium, in both batch and continuous cultures.¹⁷² Ampicillin was added to each medium at the final concentration of 100 µg ml⁻¹ to keep the sterility of the culture.¹⁷² The optical density (Absorbance reading at 600 nm) of *E. coli* was 1.8 ± 0.5 both in batch and continuous cultures, when samples were taken for the X-ray scattering. For the continuous cultures of *E. coli*, the cells were grown in a working volume of 250 ml in a 500 ml three necked round bottomed flask. A batch culture of the *E. coli* was performed for the purpose of attaining the maximum specific growth rate of the strain. The maximum rate was determined to be 0.90 hr⁻¹. A dilution rate of 0.4 hr⁻¹ (flow rate of 100 ml hr⁻¹) was used below the maximum specific growth rate in the continuous growth of the *E. coli* to avoid washout of the cells.¹¹⁶ This amplitude of flow rate in continuous cultures and in situ X-ray scatterings is enough to give a mixing effect to the mixture in the vial so that the cells are kept in suspension and in homogeneous condition in the vial. An overhead mechanical stirrer with a Teflon blade

(Chemglass, Vineland, New Jersey) was used as an agitator rotating at 300 rpm. Filtered air was provided at 3 vvm. pH remained at 7, not changing much during the cultures. The exiting culture out of the reactor was pumped to a glass vial to take an XRS. A schematic diagram of the continuous cultures of *E. coli* and in situ measurement of XRS is shown in Figure 5.3. Growth studies on *E. coli* after exposure to the X-rays are given in Appendix C.5. In brief, no adverse effects of the X-rays on cell culture health were observed.

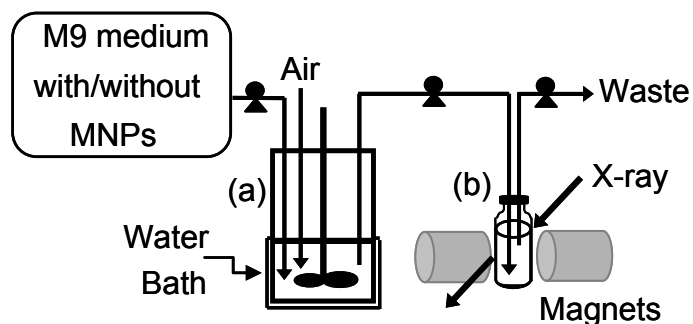


Figure 5.3 A schematic diagram of (a) the continuous culture of *E. coli* and (b) the *in situ* x-ray scattering.

5.3.3 X-ray scattering system

The X-ray machine is a Rigaku 18 kW rotating anode source with a Cu source. The 1.54 Å line was chosen by a bent graphite monochromator, which has a resolution of $\Delta q = 0.017 q_0$ at FWHM. The beam was controllable by shutters, which were set at $1 \times 0.2 \text{ cm}^2$. The power used was the maximum at 60 kV times 300 mA in in-situ X-ray scattering from continuous cultures of *E. coli* in the presence of the magnetic particles. A power of 50 kV times 100 mA was used in the other cases. It

took forty seconds to obtain one scattering measurement. A silicon standard was used to center the sample and make sure that the differences observed were due to the magnetic particles and not to a slide in the X-ray motors.

The X-ray scattering study was performed on a glass vial (Kimble glass, Vineland, NJ; 13.4 mm in diameter and 45 mm high) containing *E. coli* culture samples. A permanent magnet, made of neodymium-iron-boron (Arbor Scientific, Ann Arbor, MI), in cylindrical shape, 2.2 cm in diameter and 2.6 cm in length, was placed on each side of the vial to apply a magnetic field to the system. A holder was devised to fix the position of the vial and the two magnets, where the long axis of the vial and the directions of the magnetic field were orthogonal. The position of the magnets could be adjusted to change the distance between the magnets and thus the magnetic field strength. The distance between the two magnets was set using an aluminum bar with a predetermined width corresponding to a magnetic field strength (Figure 5.4). 227, 298, 362 and 423 mT were employed in batch and continuous cultures of *E. coli*. Before each XRS scan was started, the magnetic holder was adjusted into a position such that the magnetic field lines between the two magnets were perpendicular to the X-ray beam line when the two theta angle is zero.

Four types of XRS results were obtained depending on whether or not *E. coli* was cultured with MNPs and whether or not the XRS of a sample was measured in a magnetic field, which are as follows: (1) XRS of an *E. coli* culture, (2) XRS of *E. coli* cultured with MNPs, (3) XRS in a magnetic field of an *E. coli* culture, and (4) XRS in a magnetic field of *E. coli* cultured with MNPs.

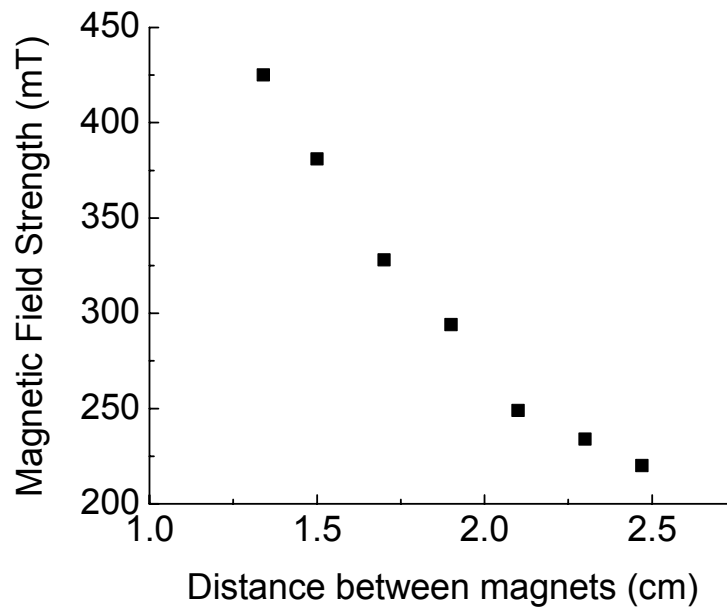


Figure 5.4 Magnetic field strength as a function of the distance between the two magnets. Field strengths of 227, 298, 362, and 423 mT were used in the experiments.

5.3.4 Transmission electron microscope (TEM) images

The interactions between the cells and the nanoparticles were observed using a Zeiss EM10 CA microscope at the University of Maryland Biological Ultrastructure Facility. Samples of *E. coli* were withdrawn at points during late exponential phase, where the optical density at 600 nm was about 0.6. After collection, they were centrifuged and suspended at room temperature in 0.12M Millonig's phosphate buffer at pH 7.3 and later with 2% glutaraldehyde. The cell pellets were then washed again with the buffer, and then the secondary fixation of the cells was performed with 1% OsO₄. At this point, they were washed with distilled water and then postfixed with 2% uranyl acetate, rinsed in the buffer and double distilled water, dehydrated in a series of ethanol and propylene oxide immersions, and embedded in Spurr's resin. A diamond knife was used to section the embedded cells. The sections were post-stained with 2.5% aqueous uranyl acetate and 0.2% aqueous lead citrate.

5.4 Results and Discussion

Two X-ray scattering studies were performed: one in batch grown *E. coli* and one in continuous cultures. The results from the batch grown sample were difficult to assess, because the sample tended to settle at the bottom of the vial, introducing a non-homogeneity in the solution. A solution measured with no magnetic field varied from one measured for example at 362 mT, and one measured without MNPs differed from one with MNPs but it could not be determined if it was due to the

inhomogeneity or the presence of the MNPs. Therefore, the changes could not be exactly measured from one magnetic field to another or from one sample to the next.

In situ measurement of X-ray scattering using continuous cultures of *E. coli* was tried as an alternate to the batch cultures, for continuous cultures make it easier to maintain steady state growth conditions including the cell concentration among the measurements by controlling the dilution rate. Reproducible results were obtained using this approach. Because the *E. coli* sample is being continuously renewed, the MNP's are not allowed much time to agglomerate.

Figure 5.5a shows the X-ray scattering taken of the *E. coli* corresponding to the continuous cell culture alone, without the MNPs. In a study of *E. coli* membranes, Esfahani *et al.*¹⁶² identified a diffuse band at 0.34 nm (3.4 Å), a sharp band at 0.42 nm (4.2 Å) and a diffuse band at 1.05 nm (10.5 Å). The low angle (1.05 nm) corresponds to the long range organization¹⁷³ of the hydrocarbon chains that make up the membrane. From Figure 5.4a, two peaks are resolved in this region, a sharp peak corresponding to $q = 0.528 \text{ \AA}^{-1}$, which corresponds to a separation of 1.189 nm (11.89 Å), and a diffuse one at 0.612 \AA^{-1} , which corresponds to the diffuse peak reported by Esfahani *et al.*¹⁶² The peak at 0.528 \AA^{-1} or 1.189 nm probably corresponds to a lower reflection of the 0.42 nm sharp peak which corresponds to the lipid membrane. Figure 5.5a shows the four different magnetic fields applied in the experiments: 227, 298, 362 and 423 mT. None of the peaks are affected by the application of the magnetic fields, except the one at $q = 0.534 \text{ \AA}^{-1}$ at 423 mT.

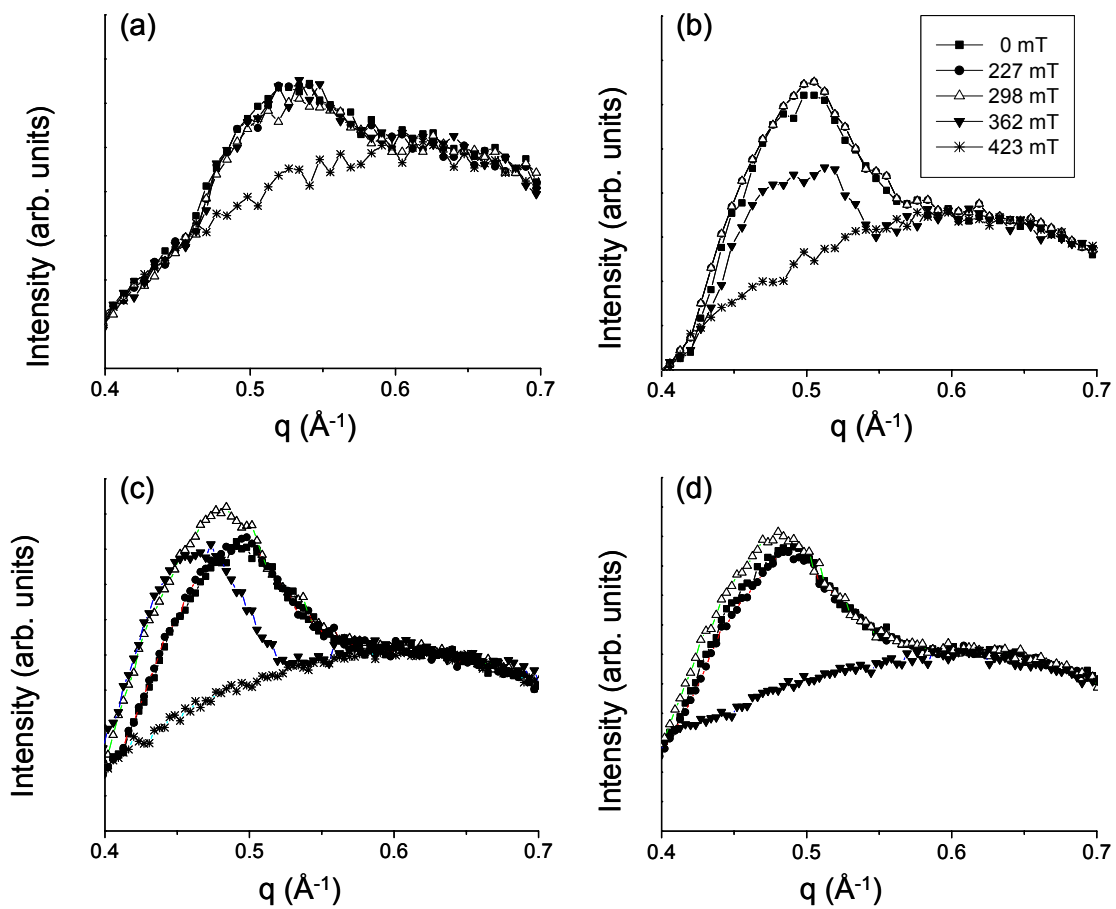


Figure 5.5 *In situ* X-ray scattering results from *E. coli* continuous cultures (a) in the absence and (b)-(d) in the presence of the magnetic particles (three repeated experiments). $q = 4\pi \sin \theta/\lambda$.

Figure 5.5 b-d show the effect of adding the magnetic nanoparticles to the cultures. Figures 5.5c and 5.5d are repeats of the same experiment in Figure 5.5b. The peak at 0.528 \AA^{-1} shifts to 0.485 \AA^{-1} , which corresponds to 1.296 nm (12.96 \AA). This suggests an interaction of the cell and the magnetic particles, because of the magnetic field produced by the particles, without the application of the magnetic field. Note that the 0.612 \AA^{-1} peak does not change position. The effect of the magnetic particles is summarized in Table 5.1 and Figure 5.6. At 362 mT , the peak oscillates in value as seen in Figure 5.6, whereas the peaks for the other magnetic fields remains constant, as seen from Figure 5.5 b–d. Therefore, it is a conclusion that 362 mT represents a critical field. The 0.612 \AA^{-1} peak does not change, probably because it is not a signal due to the lipids in the membranes.¹⁶²

Figure 5.7 shows two TEM images of *E. coli* and the magnetic nanoparticles. Note that not all the cells have magnetic particles in the vicinity, but the ones that have show that the particles are in contact with the cells. Figure 5.7b suggests that maybe the particles are attaching themselves through the SiO_2 portion, which is the more biologically compatible part of the nanoparticles. The TEM images confirm that the X-ray scattering is looking at the particle-cell interactions. The fact that the magnetic nanoparticles are not functionalized suggests that surface modification of the MNPs may have a greater impact on the structure and the interactions with the cellular membrane. An indication that this is the case happens when the *E. coli* was mixed with 10 nm FeCo particles that have been functionalized with polyethylene glycol. A new peak corresponding to 1.672 nm (16.72 \AA) appeared.¹⁷⁴ Fe_3O_4 particles covered with gum arabic and mixed with *E. coli* also indicate this.¹⁷¹

Table 5.1 Peak positions as a function of the presence of the particles and applied magnetic field strengths.

	Peak 1		Peak 2	
	q (\AA^{-1})	d (\AA)	q (\AA^{-1})	d (\AA)
<i>E. coli</i> , 0 mT	0.528	11.89	0.612	10.27
<i>E. coli</i> and MNPs, 0 mT	0.485	12.96	0.612	10.27
<i>E. coli</i> and MNPs, 227 mT	0.485	12.96	0.612	10.27
<i>E. coli</i> and MNPs, 298 mT	0.485	12.96	0.612	10.27
	0.481	13.09		
<i>E. coli</i> and MNPs, 362 mT	0.485	12.96		
	0.459	13.68		
	N/A	N/A	0.612	10.27
<i>E. coli</i> and MNPs, 423 mT	N/A	N/A	0.612	10.27

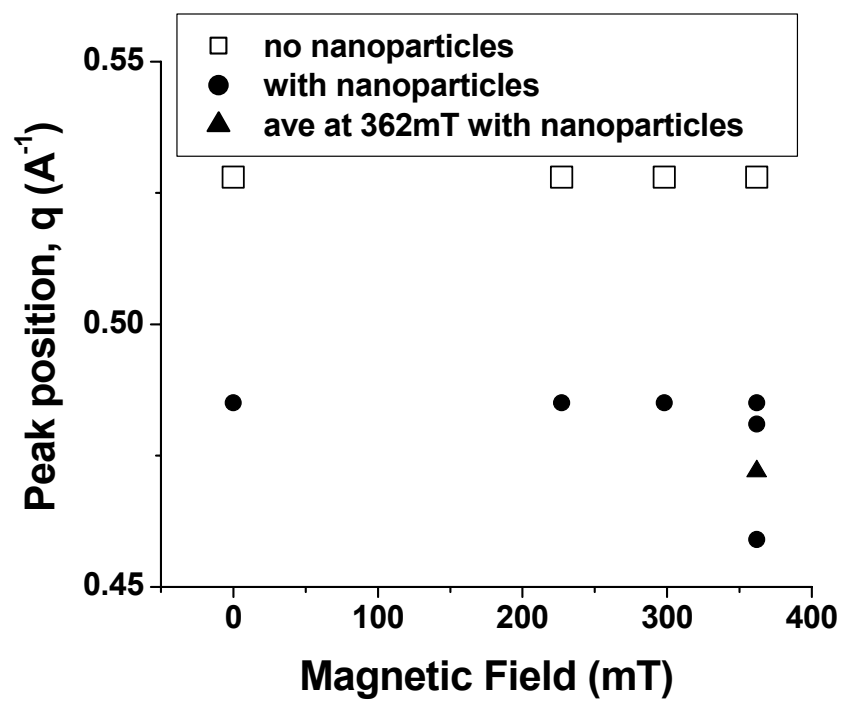


Figure 5.6 Peak position as a function of the applied magnetic field strengths.

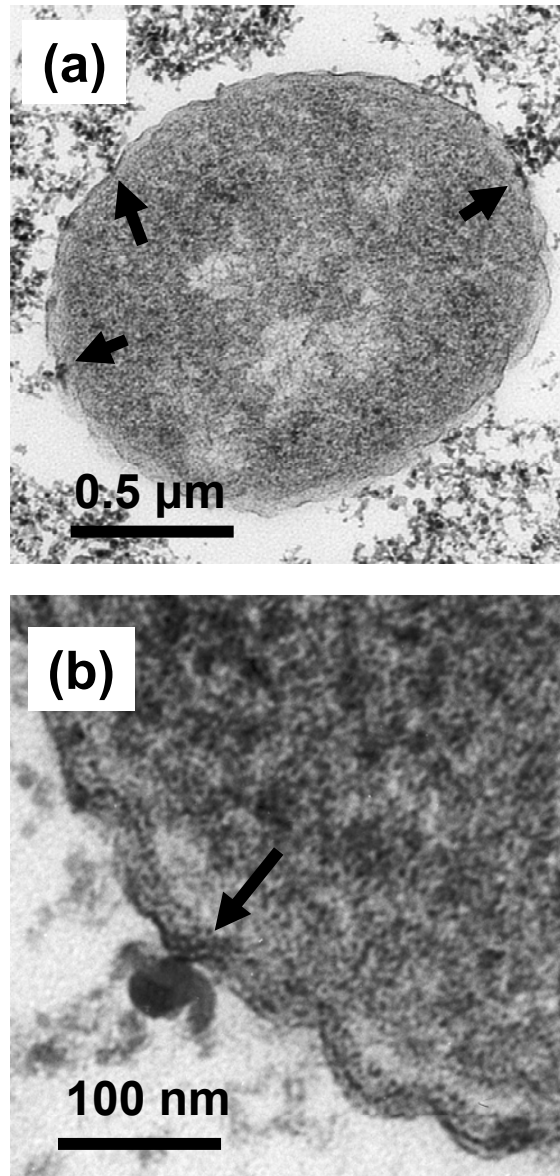


Figure 5.7 Transmission electron micrograph images showing that *E. coli* have contacts with the $\text{SiO}_2/\gamma\text{-Fe}_2\text{O}_3$ particles. Arrows point out contacting parts between the cell and the particles. (a) An *E. coli* cell surrounded by the magnetic particles. (b) A magnetic particle is in contact with the *E. coli* membrane.

An XRS study was conducted to investigate the effect of MNP concentration up to 100 mg l⁻¹ to the peak shifts. Effects of divalent ions such as Ca²⁺, Mg²⁺, and SO₄²⁻ in cell culture medium on XRS-detected peak shifts were also studied. The XRS data are presented in Appendix C.6 with a brief discussion of the results.

5.4 Conclusions

X-ray scattering was performed on continuous cultures of *E. coli* cells, which are grown in the absence/presence of SiO₂/γ-Fe₂O₃ composite particles which are magnetic particles. This study of the interactions between *E. coli* and the MNPs using XRS provides insight on how the MNPs affect the membrane structure in the applied magnetic fields. Magnetic fields up to 423 mT were applied on the cells, to observe the effect of the magnetic particles and the magnetic field strengths. In situ X-ray scattering from continuous cultures gave significant differences, depending on whether or not the particles were included in the cell cultures. Two peaks were observed in the in situ X-ray scatterings from continuous cultures of *E. coli*, a sharp peak at $q = 0.528 \text{ \AA}^{-1}$ up to 362 mT of magnetic field strength and a broad one at $q = 0.612 \text{ \AA}^{-1}$ when the particles were not added to the cultures. The sharp peak showed a change from $q = 0.53284 \text{ \AA}^{-1}$ to $q = 0.485 \text{ \AA}^{-1}$ when the particles were added, due to the effect of the magnetic field of the particles. A critical magnetic field strength was observed at 362 mT, at which the value for the peak oscillates every time the experiment is repeated. Beyond this field the sharp peak disappears and only the peak at 0.512 \AA^{-1} remains. TEM images of the cells grown in the presence of the particles showed that some cells had the magnetic particles in contact with the

membranes, which supports the suggestion that the changes in X-ray scattering comes from the interactions between the particles and the cell membranes. Non-functionalized particles were used in these experiments. Modifying the particles with biofunctional molecules may cause larger differences in the X-ray scattering since the particles may be able to penetrate the *E. coli*.

Chapter 6: Conclusions and recommendations

6.1 Conclusions

Systematic studies of the functionalization of metal oxide nanoparticles for biological applications were conducted. Hybridization of anti-mouse IgG on magnetic $\gamma\text{-Fe}_2\text{O}_3$ nanoparticles was achieved via silane chemistry with 3-aminopropyl triethoxy silane and glutaraldehyde activation. The bio-activity of immobilized anti-mouse IgG was evaluated by magnetic-field assisted sequestration of mouse IgG in solution with the anti-mouse IgG immobilized MNPs. A chemisorption isotherm, obtained via fluorescence-based assays, provides a quantitative evaluation of anti-mouse IgG binding to the magnetic nanoparticles (MNPs). The results show that anti-IgG binding is controlled stoichiometrically and the saturated surface coverage is $\sim 36\%$ of the theoretical limit. This saturated binding corresponds to 34 randomly oriented anti-mouse IgGs per average size MNP with 32 nm diameter. Fluorescence spectroscopy analysis of magnetic field assisted-sequestration of mouse IgG indicates that the hybridized anti-mouse IgG retains $\sim 50\%$ of its bio-activity at saturation.

Differential functionalization of aerosol-phase synthesized $\text{SiO}_2/\text{TiO}_2$ mixed nanoparticles was demonstrated via an X-ray photoelectron spectroscopy study. Differential functionalization of the composite metal oxide-metal oxide nanoparticles was achieved using a sequential reaction of preferential binding of phenyl phosphonic acids (PPA) to TiO_2 and subsequent binding of trimethyl silyl group to the remaining

SiO₂ surface. For comparative understanding of differential functionalization, SiO₂/TiO₂ mixed nanoparticles with three approximate mole ratios of Si:Ti = 5:1, 1:1, and 1:5 as well as pure SiO₂ and TiO₂ nanoparticles were used. XPS results in the P 2p region demonstrate that aqueous phase reaction of the nanoparticles with PPA leads to preferential binding of PPA to TiO₂ vs. SiO₂ surfaces. This preferential binding of PPA to TiO₂ is presumably due to much higher stability of the Ti-O-P bond to hydrolysis than the Si-O-P bond. Tridentate binding mode of PPA on the bulk TiO₂ is described as PhP(OTi)₃, while the tridentate binding of PPA to the interface of SiO₂-TiO₂ is suggested as PhP(OTi)_x(OSi)_y (here, x + y = 3, and x = 1 or 2). XPS analysis infers that PPA binds to a surface of TiO₂ at an averaged atomic ratio of 0.05 P/Ti. The atomic ratio of P/Ti is retained at 80% ± 10% for SiO₂/TiO₂ mixed nanoparticles after silanation reaction with a trimethyl silyl group binding. XPS spectra in the C 1s and Ti 2p regions are indicative of trimethyl silyl group binding to PPA-reacted nanoparticles.

An X-ray scattering (XRS)-mediated technique for the study of interactions between *E. coli* cell membranes and magnetic nanoparticles was developed. *In situ* XRS of *E. coli* in a magnetic field up 423 mT displays two peaks, a sharp peak at $q = 0.528 \text{ \AA}^{-1}$ (1.189 nm) up to 362 mT of magnetic field strength and a diffuse one at $q = 0.612 \text{ \AA}^{-1}$ (1.027 nm). The presence of SiO₂/γ-Fe₂O₃ magnetic nanoparticles at a concentration of 40 mg/L shifted the sharp peak to a smaller side of q as applied magnetic field is increased from 227 mT to 298 mT and up to 362 mT, whereas the diffuse peak did not change. A critical magnetic field strength was 362 mT, at which the peak disappears.

These three research topics mentioned above are related to each other in the sense that these studies have advanced our knowledge of nanoparticle functionalization and biological applications of the nanoparticles. The quantitative understanding of antibody immobilization on magnetic nanoparticles based on fluorescence assays can be applied to construct multifunctional nanocomposites with biological functional groups using Fe_2O_3 , $\text{SiO}_2/\text{Fe}_2\text{O}_3$ or $\text{SiO}_2/\text{TiO}_2$ nanoparticles. The detailed study of surface modification adopting XPS characterization in Chapter 4 is helpful for better understanding APTES modification of magnetic iron oxide nanoparticles in Chapter 3 and future surface modification of the magnetic nanoparticles. These particles are aimed at applications in biological systems in the presence of biological cells such as *E. coli*., such as for a sensitive detection of biological cells and for drug delivery purposes. The improved understanding of interactions between *E. coli* and $\text{SiO}_2/\gamma\text{-Fe}_2\text{O}_3$ nanoparticles obtained via the X-ray scattering study in Chapter 5 will be helpful in engineering specific interactions between biological cells and the nanoparticles in those biological applications.

6.2 Recommendations

The technique described in Chapter 3 to evaluate surface coverage and bio-activity of dye-labeled antibodies bound on MNPs is a general method and can be applied to any dye-labeled proteins of interest to quantify their surface coverage on MNPs after hybridization.

The quantitative understanding of antibody hybridization with magnetic iron oxide nanoparticles opens the possibilities for the use of these nanoparticles in biological applications such as magnetic resonance imaging and sensitive bio-separation. Control of antibody immobilization on magnetic nanoparticles may lead to the formation of multifunctional nanoparticles by attachment of other functionalities such as a poly(ethylene glycol) (PEG) moiety for an extended blood circulation in cancer therapy (Figure 6.1).¹¹ Monodisperse magnetic nanoparticles (MNPs) with diameters less than 10 nm are effective in MRI^{25, 26} and can be synthesized following recently reported methods²⁷⁻²⁹. Zhang and collaborators used cancer-specific functionalities such as folic acid and chlorotoxin in their MRI studies.^{89, 90} Cancer-recognizing antibodies more readily available than specific binding moieties are suggested to be bound on MNPs for their MRI studies. Cheon and collaborators attached cancer-specific antibodies on MNPs in their application for MRI.^{25, 26} However, the functionality for enhancing circulation in blood and overcoming biobarriers is absent in their MNP-antibody system. Attachment of PEGs on the surface of MNPs by adding a controlled amount of activated PEG derivative such as mPEG-succinimidyl propionate (mPEG-SPA; Nektar, San Carlos, CA) is recommended as shown in Figure 6.1. For the use of intraoperative optical devices, dye molecules can be attached, either directly on MNPs or indirectly via the binding of dye-labeled antibodies.

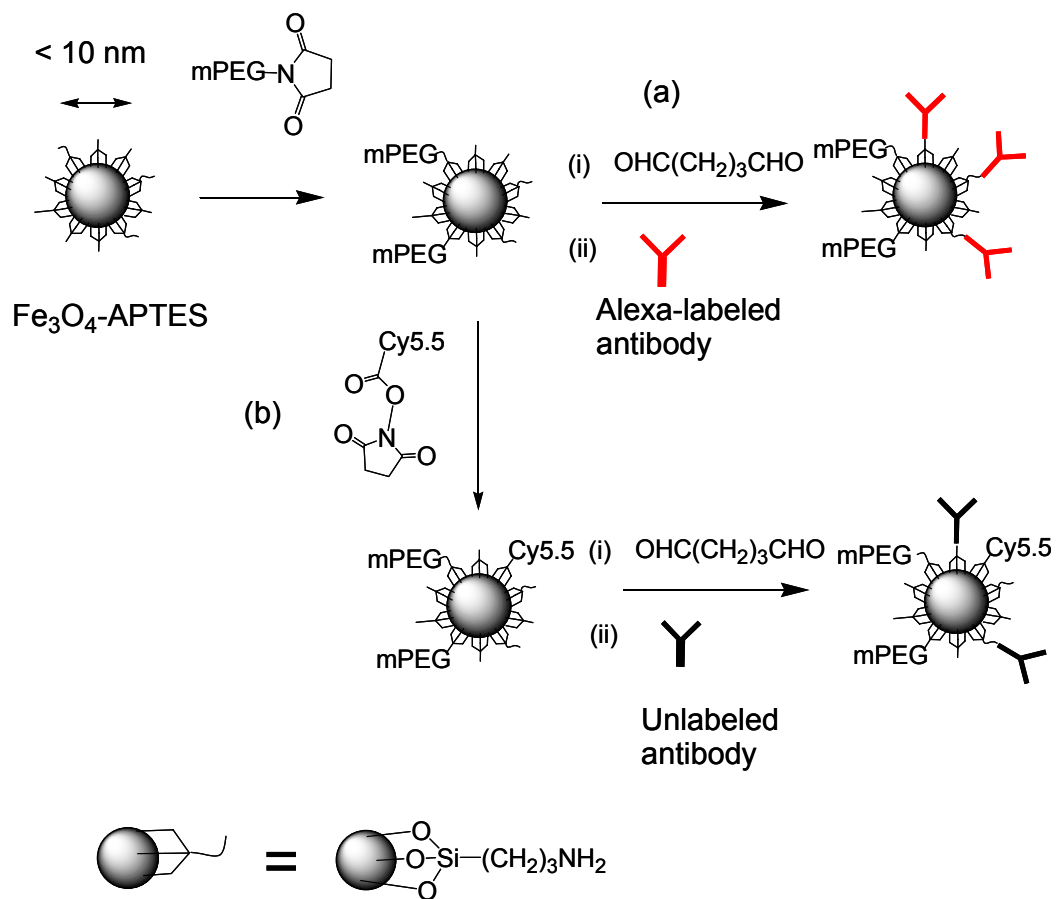


Figure 6.1 Proposed reactions to build multifunctional magnetic nanoparticles for MR imaging.

Kim and collaborators² reported peptide-mediated intracellular uptake of MNP-peptide hybrids and identified target proteins inside living cells using movement of intracellular MNPs in applied magnetic fields. They probed the movement and localization of MNPs by fluorescence-based confocal microscopy study. Attachment of transducible peptide, TAT-HA2, on MNPs helped the MNP conjugates to be taken inside the cells. For the application in cancer treatment via hyperthermia, it is suggested to hybridize MNPs with cancer-specific antibodies, TAT-H2, and dye molecules as described in the previous section. Confocal microscopy-based study of hyperthermia will elucidate the effectiveness of the suggested methodology.

Monitoring expression of cell surface-bound proteins can be a target for future study using MNPs hybridized with the protein-specific molecules. Magnetic field-assisted separation of MNP-biological cell conjugates will confirm the existence of cell surface-expressed proteins.

Differential functionalization of SiO₂/TiO₂ nanoparticles by the sequential reaction with organophosphorous compounds and silane reagents can be an effective route to the fabrication of multifunctional nanoparticles. The availability of phosphorous compounds containing terminal functional groups such as –OH,^{100, 101} –SH,¹⁴⁸ and –COOH^{149, 150} and the well-established silane chemistry provide a number of ways to attach different functionalities on the mixed nanoparticles. Functionalization of SiO₂/TiO₂ by a surface-specific approach with different reaction groups is suggested as shown in Figure 6.2. This differential functionalization with

both –SH and –NH₂ functional groups on the surface will increase applicability of the mixed nanoparticles.

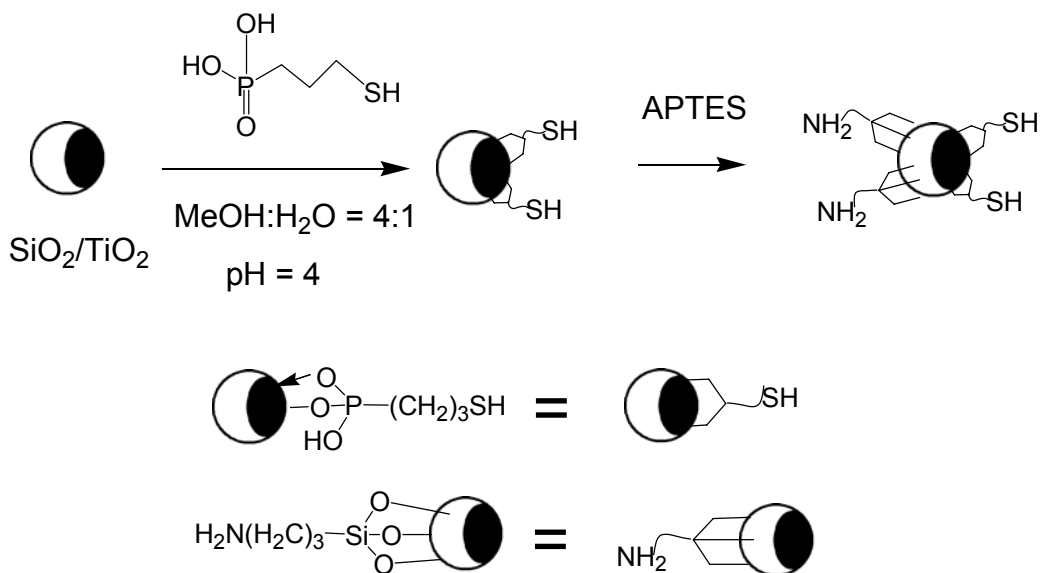


Figure 6.2 Suggested scheme of differential functionalization.

Recently, synthesis of metal-metal oxide particles has been reported.^{3, 12, 37, 38,}
¹⁷⁵ Nanosize Au-metal oxide dimers have been made via metal oxide nanoparticle assembly at a liquid-liquid interface³ and decomposition of metal oxide precursors on Au surfaces¹². Asymmetric binding between metal and metal oxide nanoparticles may have advantages over spherical nanoparticles in an attempt to construct multifunctional nanoparticles and applications requiring higher complexities and lower symmetries.^{37, 38} The differential functionalization demonstrated in Chapter 4 provides a novel way to construct Au-composite metal oxide nanostructures. A

variety of composites of Au-SiO₂/TiO₂ mixed nanoparticles can be made via selective binding of Au nanoparticles on a specific portion of differentially functionalized SiO₂/TiO₂ mixed nanoparticles using affinity of Au nanoparticles to thiolated- and amine-functionalized surface. First, Au nanoparticles can be attached only onto a specific surface of the mixed nanoparticles (Figure 6.3).

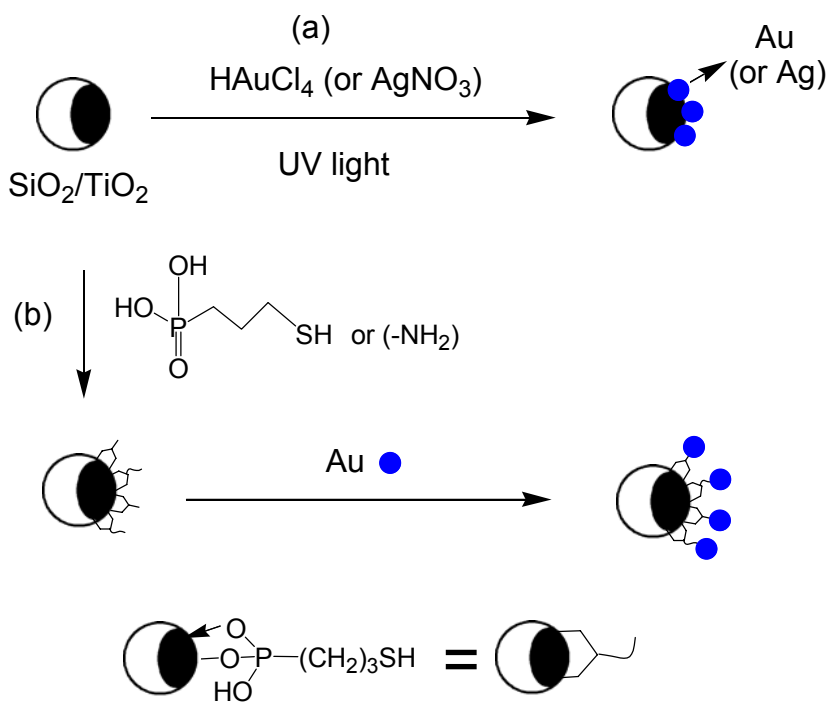


Figure 6.3 Methodologies to attach noble metal nanoparticles only to TiO₂ surfaces of SiO₂/TiO₂ nanoparticles. (a) Generation of Au (Ag) nanoparticles on a TiO₂ surface by a photocatalytic route. (b) Selective attachment of Au nanoparticles to TiO₂ via preferential binding of phosphonic acids with thiol (or amine) functional group and affinity of Au nanoparticles to TiO₂-specific thiol (or amine) functional groups.

TiO₂ is well known for its photocatalytic activity. Noble metals are deposited on TiO₂ surface via a photocatalytic route.^{45-48, 50, 176-179} This property can be applied to prepare TiO₂-specific generation and binding of Au (Ag) nanoparticles (Figure 6.3(a)). The other way to preferentially bind Au nanoparticles is via selective binding of phosphonic acids in aqueous environment. Phosphonic acids with a thiol or an amine functional group are first bound selectively on TiO₂ surfaces. Au nanoparticles prepared in another reaction can be applied to the thiol (amine) functionalized surfaces and are attached to them by Au-thiol group and Au-amine group affinity.

It is suggested that Au nanoparticles can be attached selectively on SiO₂ portion of SiO₂/TiO₂ mixed nanoparticles (Figure 6.4). TiO₂ surfaces are passivated by reaction with PPA. Subsequent silane reaction with APTES renders Au-attracting amine functional groups on silica surfaces. Addition of Au nanoparticles to the surface-functionalized particles leads to asymmetric binding of Au to SiO₂ portion of the mixed nanoparticles.

Asymmetric binding of two different size-Au nanoparticles is suggested (Figure 6.5). Preferential binding of Au nanoparticles to the SiO₂ surfaces (Figure 6.3(b)) is followed by passivation of the attached Au surfaces by the reaction with thiolated molecules and silanization of the SiO₂ surfaces by the reaction with APTES. Larger Au nanoparticles are mixed with the functionalized nanocomposite particles leading to asymmetric binding of two different size-Au nanoparticles. This will serve as visual evidence of differential functionalization of the mixed nanoparticles. Various thiol compounds can be used to react with the attached Au surfaces.

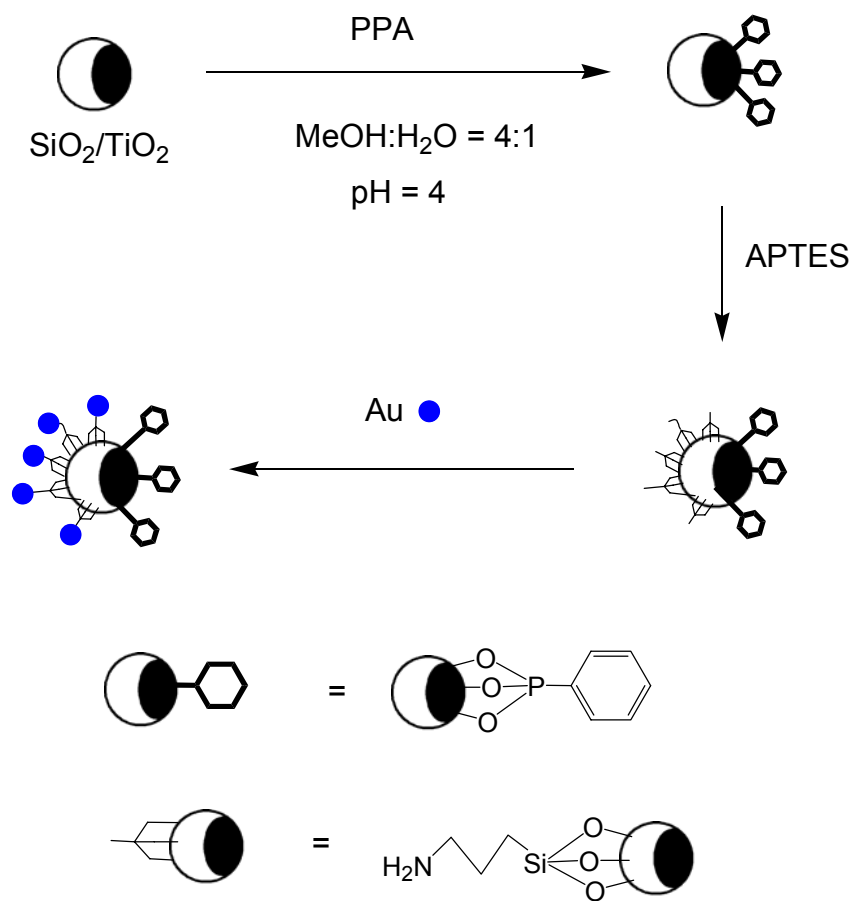


Figure 6.4 Selective binding of Au nanoparticles to the SiO_2 portion of $\text{SiO}_2/\text{TiO}_2$ mixed nanoparticles. PPA: phenyl phosphonic acid.

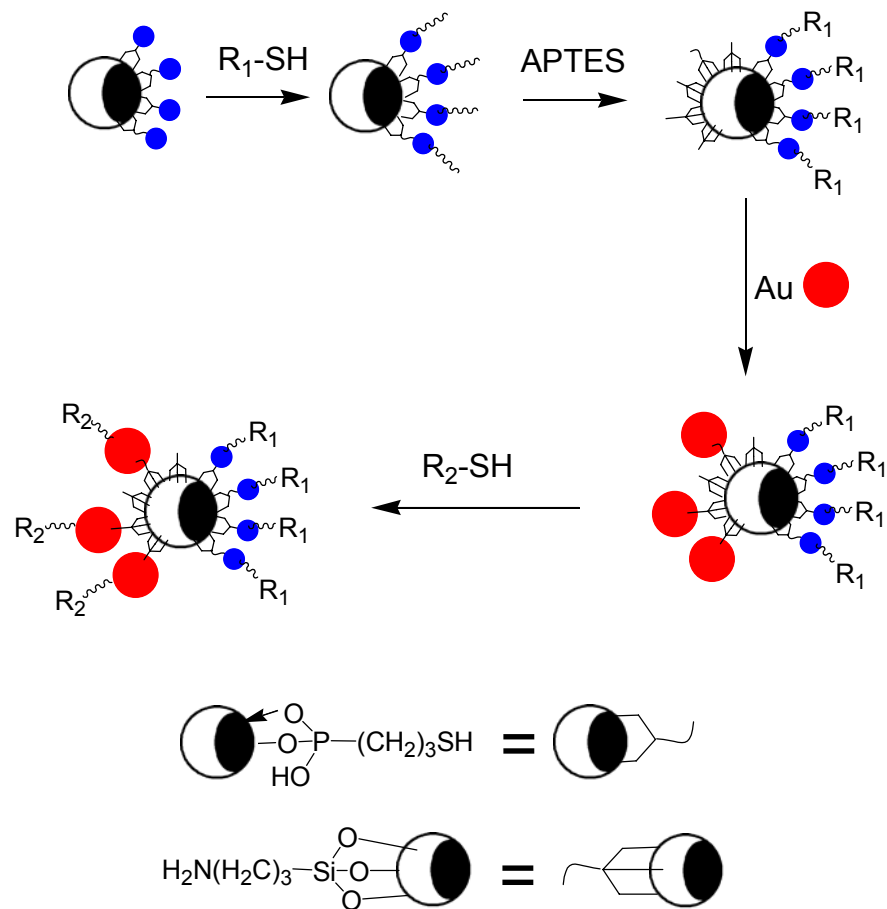


Figure 6.5 Asymmetric binding of two different size-Au nanoparticles to SiO₂/TiO₂ mixed nanoparticles.

Finding a functionality, that binds preferentially to $\text{SiO}_2/\text{Fe}_2\text{O}_3$ mixed nanoparticles, is the next task. Since Si-O-P bonds are readily hydrolysable, the first trial can be to apply organophosphorous compounds to the mixed nanoparticles in an aqueous solution.

The synthesis methodology of Fe_3O_4 -Au dimmers at a liquid-liquid interface can be applied to prepare Au- $\text{SiO}_2/\text{Fe}_2\text{O}_3$ dimers, where Au nanoparticles are attached to the Fe_2O_3 portion by making Fe^{2+} surface ions as catalytic sites.^{3, 9}

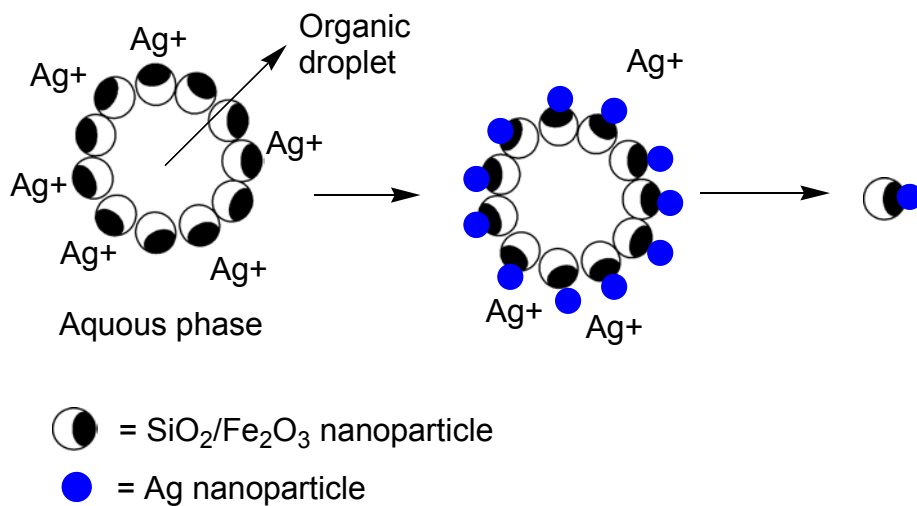


Figure 6.6 Synthesis of Au- $\text{SiO}_2/\text{Fe}_2\text{O}_3$ dimers via nanoparticle assembly at a liquid-liquid interface.

Effects of concentrations of $\text{SiO}_2/\gamma\text{-Fe}_2\text{O}_3$ MNP up to 100 mg MNP/L and concentrations of divalent ions such as Ca^{2+} , Mg^{2+} , and SO_4^{2-} on XRS scattering are discussed in Appendix C.6. The nanoparticles used in the XRS study were bare unmodified particles. Additional XRS studies using functionalized MNPs such as MNPs coated with a PEG layer and those suggested in Figure 6.6 need to be done to see if the functionalized particles are more lipophilic and can penetrate the cellular membrane.

Appendices

Appendix A

Appendix A covers protocols and experimental data related to Chapter 3.

A.1 Protocol for APTES modification of magnetic iron oxide nanoparticles

1. Set up a 500 mL-capacity three neck round bottomed (RB) flask with a stirring rod combined with a Teflon blade (Chemglass, Vineland, NJ). Apply vacuum grease at the junction between the RB flask and the stirring rod.

--- Cleaning of the glassware---

2. Clean the glassware with piranha solution (conc H_2SO_4 and 35% H_2O_2 , 3:1 v/v) in the following order. Operate in a chemical hood.

2a. Add 150 mL of Con H_2SO_4 to the RB flask.

2b. Add 50 mL of 35% H_2O_2 to the H_2SO_4 in the RB flask.

Note: Be careful because of a large amount of heat generation during this process.

2c. Wait for 1 hour.

2d. Decant the piranha solution to a waste bottle. Wash thoroughly the glassware ten times with 20 mL of fresh double distilled water each time.

---APTES reaction---

3. Add 45 mL of double distilled water in the RB flask.
4. Add 1.5 g of $\gamma\text{-Fe}_2\text{O}_3$ particles (Alfa Aesar, Ward Hill, MA).

5. Suspend the γ -Fe₂O₃ particles in aqueous solution with 20 minute sonication in a bath sonicator.
 6. Set up the RB flask with a condenser linked to a nitrogen source. Put the glassware in an oil bath on a heating plate. Connect the stirring rod with a mechanical stirrer. Turn on water, nitrogen, and heat.
 7. Add 5 mL APTES drop by drop to the solution while vigorous mechanical stirring.
 8. Control heat so that the temperature of the oil bath can be maintained at 120 °C.
 9. Maintain this reflux condition for 3 hours.
 10. Turn off the heater and cool down the reaction system.
 11. Decant the reacted suspension of γ -Fe₂O₃ particles to a 50 mL-capacity centrifuge tube.
 12. Separate the magnetic nanoparticles using a neodymium-iron-boron permanent magnet.
- Washing---
13. Add 20 mL of double distilled water to the separated magnetic particles.
 14. Suspend and mix the particles for 3 minutes on a vortexer.
 15. Repeat steps 12-14 twice more.
 16. Repeat steps 12-14 once. This time use 20 mL of 95% ethanol instead of water in step 12. Separate the particles with the permanent magnet and remove the supernatant.
 17. Remove the remnant ethanol as much as possible by centrifugation at 4500 rpm for 5 minutes.
- Drying and storing---

18. Dry the resulting magnetic nanoparticles overnight in vacuum.
19. Store the dried particles in a desiccator until further usage.

A.2 Protocol for glutaraldehyde activation

Glutaraldehyde kit was purchased from Polysciences (Warrington, PA)

1. Place 10 mg of APTES-modified iron oxide in a glass vial.
2. Add 1 mL of PBS to the vial and sonicate for 10 minutes in a bath sonicator.
3. Add 3 mL of 8 % glutaraldehyde in PBS (Polysciences, Warrington, PA) to the vial.

Note: This step makes the final glutaraldehyde concentration 6 %.

4. Mix for 5-6 hours at room temperature on a rocker table, rotary shaker, or any kind of shaker which provides end-to-end mixing.
5. Discard the supernatant while holding the particles using a magnet.
6. Resuspend particles in 2 mL of PBS (Washing step).
7. Vortex until the particles are completely dispersed.
8. Discard the supernatant while holding the particles using a permanent magnet.
9. Repeat steps 6-8 twice more.
10. Suspend the particles in a desired amount of PBS.

(Ex) 4.0 mL of PBS was added to 10 mg MNPs in the method of Chapter 3.

11. Use the glutaraldehyde-activated MNPs right away for immobilization of anti-mouse IgG.

A.3 Protocol for immobilization of Fluorescein-labeled anti-mouse IgG on the MNPs

1. Prepare a PBS solution containing anti-mouse IgG at a desired concentration.
2. Add 80 μL of 4.0 mL of PBS solution containing 10 mg of glutaraldehyde-activated MNPs (step A.2.10) to 920 μL of an anti-IgG solution in PBS. The amount of MNPs in 1 mL of the mixture is 0.20 mg.
3. Shake at room temperature for 20 hours.
4. Separate the MNPs with a permanent magnet.
5. Take the supernatant and keep it separate for determination of amount of anti-IgG in the supernatant.
6. Add 1 mL of PBS (pH 7.4) and vortex briefly.
7. Repeat steps 4-6 twice.
8. Suspend 0.20 mg of the MNPs in 1.0 mL of PBS and store them in a refrigerator until further usage.

A.4 Protocol for labeling antibodies with reactive dyes with succinimidyl ester group

Succinimidyl ester-functionalized dyes (Molecular probes, Eugene, OR) form a stable amide bond with amine groups of antibodies such as lysine.

1. Dialyze antibody solution containing sodium azide as preservatives for 2 hours in PBS solution, using Spectra/Por (Rancho Dominguez, CA) dialysis kit (molecular weight cut-off 50,000).

2. Dissolve succinimidyl ester-linked dyes in dimethyl sulfoxide (DMSO) right before a labeling reaction at 10 mg dye/mL DMSO.

(Ex) Add 1 mg dye to 0.1 mL DMSO.

3. Add 0.1 mL sodium bicarbonate buffer (pH 8.3-9.0) for each mL of antibody solution, since succinimidyl ester-dyes react with ϵ -amino groups in a slightly basic buffer.

4. While stirring an antibody solution, add the reactive dye solution slowly. Stir the mixture of antibody and dye for 1 hour at room temperature in protection from light.

5. Separate the conjugates from unreacted free dyes in a PBS-equilibrated Sephadex G-25 column. The first excluded fraction to elution is the dye-antibody conjugate.

6. Store the dye-antibody conjugates at 4 °C in 2 mM sodium azide as preservative.

7. Determine the degree of labeling.

- 7a. Dilute the protein-dye conjugate to approximately 0.1 mg/mL. Measure the absorbance of the protein-dye conjugate at 280 nm and at λ_{\max} (λ_{\max} of Alexa 568 = 578 nm) of the dye.

- 7b. Correct the contribution of the dye in the absorbance at 280 nm.

$$A_{\text{protein}} = A_{280} - A_{\text{max}} \times \text{CF} \quad (\text{A.1})$$

(CF = $A_{280 \text{ free dye}}/A_{\text{max free dye}}$; CF is given by the dye vendor)

7c. Calculate the protein concentration.

$$1.4: A_{\text{protein}} = 1 \text{ mg/mL} : \text{Protein concentration (mg/mL)} \quad (\text{A.2})$$

This equation is correct for IgG antibodies.

7d. Calculate the degree of labeling (DOL).

DOL is defined as the dye concentration in the antibody-dye conjugates divided by the antibody concentration in the conjugates.

$$\text{DOL} = \frac{C_{\text{dye}}}{C_{\text{antibody}}} \quad (\text{A.3})$$

The Beer-Lambert Law is given as equation A.4.

$$A = \epsilon \times C \times l \quad (\text{A.4})$$

A: absorbance

ϵ : the extinction coefficient, $\text{cm}^{-1}\text{M}^{-1}$

C: mole concentration; mol/L

l : light pathway length, 1 cm

Combining Equation A.3 with the Beer-Lambert law leads to Equation A.5.

$$\text{DOL} = \frac{\frac{A_{\lambda \text{ max, dye}}}{\epsilon_{\text{dye}} \times 1 \text{ cm}}}{\frac{[\text{Antibody}]}{MW_{\text{antibody}}}} \quad (\text{A.5})$$

where $[\text{Antibody}]$ = mass concentration of antibody (g/L).

Rearranging Equation A.5 gives Equation A.6.

$$\text{DOL} = \frac{A_{578,\text{dye}} \times MW_{\text{antibody}}}{[\text{Antibody}] \times \epsilon_{\text{dye}}} \quad (\text{A.6})$$

Because antibody does not have absorbance at 578 nm, $A_{578,\text{dye}}$ is the same with $A_{578,\text{conjugate}}$. Therefore,

$$\text{DOL} = \frac{A_{578,\text{conjugate}} \times MW_{\text{antibody}}}{[\text{Antibody}] \times \epsilon_{\text{dye}}} \quad (\text{A.7})$$

where MW_{antibody} : 150-170 kDa,

[Antibody]: given by equation A.2, and

$\epsilon_{\text{Alexa 568}}$: 91,300 $\text{cm}^{-1}\text{M}^{-1}$.

Therefore a measured absorbance of the mouse IgG-Alexa 568 conjugate at 578 nm provides DOL from Equation A.7.

A.5 Sequestration of Alexa 568-labeled mouse IgGs from solution

1. Separate 0.20 mg of MNP-anti-mouse IgG conjugates from solution (A.3.8) with a neodymium-iron-boron permanent magnet.
2. Add 1.0 mL of PBS containing a desired amount of Alexa 568-labeled mouse IgG.
3. Mix for 2-3 hours in room temperature.
4. Separate the MNPs using a permanent magnet and discard the supernatant.
5. Add 1.0 mL of fresh PBS.
6. Vortex briefly.
7. Repeat steps 4-6 three times.
8. Keep the suspended particles in PBS in a refrigerator for later characterization.

A.6 Phosphate buffered saline (PBS; pH 7.4)

NaCl	9.00 g
Na ₂ HPO ₄	0.80 g
KH ₂ PO ₄	0.14 g
dH ₂ O (distilled water)	1000 mL
Adjust pH to 7.4	

A.7 Maximum absorbance and emission wavelength of dyes used
in Chapter 3

Table A.1 Maximum absorbance/emission wavelength of dyes.

	Maximum Absorbance Wavelength (nm)	Maximum. Emission Wavelength (nm)
Fluorescein	495	520
Alexa Fluor 568	578	603

A.8 Spex Fluorolog-3 fluorometer (Dr. Robert Walker's Laboratory)

A.8.1 Operation protocol

1. Turn on the power switch.
2. Turn on the main lamp switch.
3. Turn on the SpectACQ computer.
4. Turn on the Dell Optiplex computer.
5. Turn on the monitor screen. Wait for 15 minutes for warming up.
6. Double click "shortcut to datamax_32" icon.
7. Click "OK" and then "Yes".
8. Run "visual setup", the third square icon.
9. Click on "sample chamber" in visual set up.
10. Click on image.
11. Take both polarizers "OUT" and then close window.
12. Close polarizer window.
13. Click on "run experiment" icon in "instrumental control center".
14. Go to "collect" and click on "experiment".
15. Double click "dtfl.exp".
16. Click on "data file".
17. Choose "1.spc" under file name.
18. Go to "visual setup" window.
19. Under "options", choose "units" and change "slits" to "millimeters". Click OK.
20. In "main experiment" window, click on "slits" and change "excitation" to 0.5 (nm) and emission to 0.

21. Click “OK” and “run”.
22. Click “Yes”.
23. Record wavelength, intensity, date and name in log book.
24. Click on “experiment”
25. Control slit width.
(Ex) Slits: Excitation: 3.00 nm, Emission: 3.00 nm
26. Set the excitation wavelength and emission scanning range.
(Ex) Fluorescence-labeled anti-mouse IgG:
Excitation at 495 nm, emission scan range: 500 – 700 nm
27. Save the set up condition as **.exp.
28. Load a sample in a quartz cuvette and put it into the Fluorometer.
29. Run the sample.
30. Save the plot as *.spc file.
31. After running all the samples, turn everything off in the reverse order.
Note: Wait 15 minutes before turning off power in order to cool down the lamp before shut off.
32. Turn off the power switch.
Note: Make sure to turn off the power switch, since it is easy to forget it after waiting for a while.

A.8.2 Data processing

1. Turn on the Dell Optiplex computer.
2. Turn on the monitor screen.
3. Double click “shortcut to datamax_32” icon.
4. Open “file” and “import/export”. Click “export” without changing settings.
Choose a file(s) to transfer.
5. Retrieve through right click, start, and explore.
6. Turn off the computer.
7. Process the data with a data processing program such as Igor Pro 4.0
(Wavemetrics, Lake Oswego, Oregon).

A.9 Hitachi F-4500 fluorescence spectrophotometer (Dr. Lyle Isaacs' lab)

1. Turn on the computer, the monitor and the spectrophotometer.
2. Wait for 15 minutes for warming up.
3. Click on the spectrophotometer icon.
4. Set up a scan condition.
 - (Ex) Excitation/Emission slit: 5.0 nm/5.0 nm
 - PMT voltage: 950
 - Scan speed: 240 nm/min
5. Run the scan of antibody-MNP conjugates suspended in PBS (pH 7.4).
 - 5a. Fluorescein-labeled anti-mouse IgG on the MNPs:
 - Excitation at 480 nm; emission scan: 490- 700 nm
 - 5b. Alexa 568-labeled mouse IgG on the MNPs:
 - Excitation at 550 nm; emission scan: 560 – 800 nm
 - Note: Alexa 568-mouse IgGs caught by MNP-anti-mouse IgG conjugates were excited at 550 nm instead of 578 nm to evade scattering from the MNPs.
6. Turn off the computer and the spectrophotometer.

A.10 A standard calibration curve for quantification of Fluorescein-labeled anti-mouse IgG

A standard calibration curve of Fluorescein-labeled anti-mouse IgG is given in Figure A.1.

A.10.1 Method

-Spex Fluorolog-3 fluorometer in Dr. Robert Walker's Laboratory

-Slits: Excitation/Emission: 3.00 nm/3.00 nm

-Excitation at 495 nm, emission scan range: 500 – 700 nm

-Maximum emission intensity was measured at 520 nm.

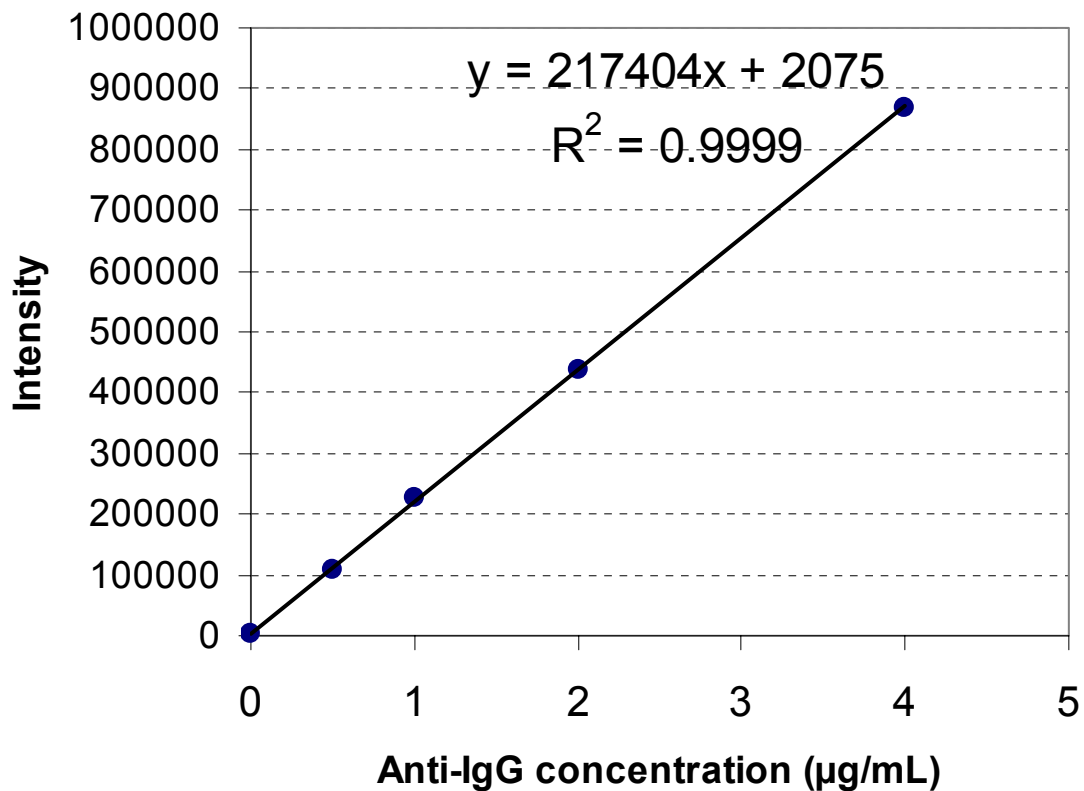


Figure A.1 Standard calibration curve of fluorescein-labeled anti-mouse IgG.

A.11 Washing effect of MNPs after reaction with Fluorescein-labeled anti mouse-IgG

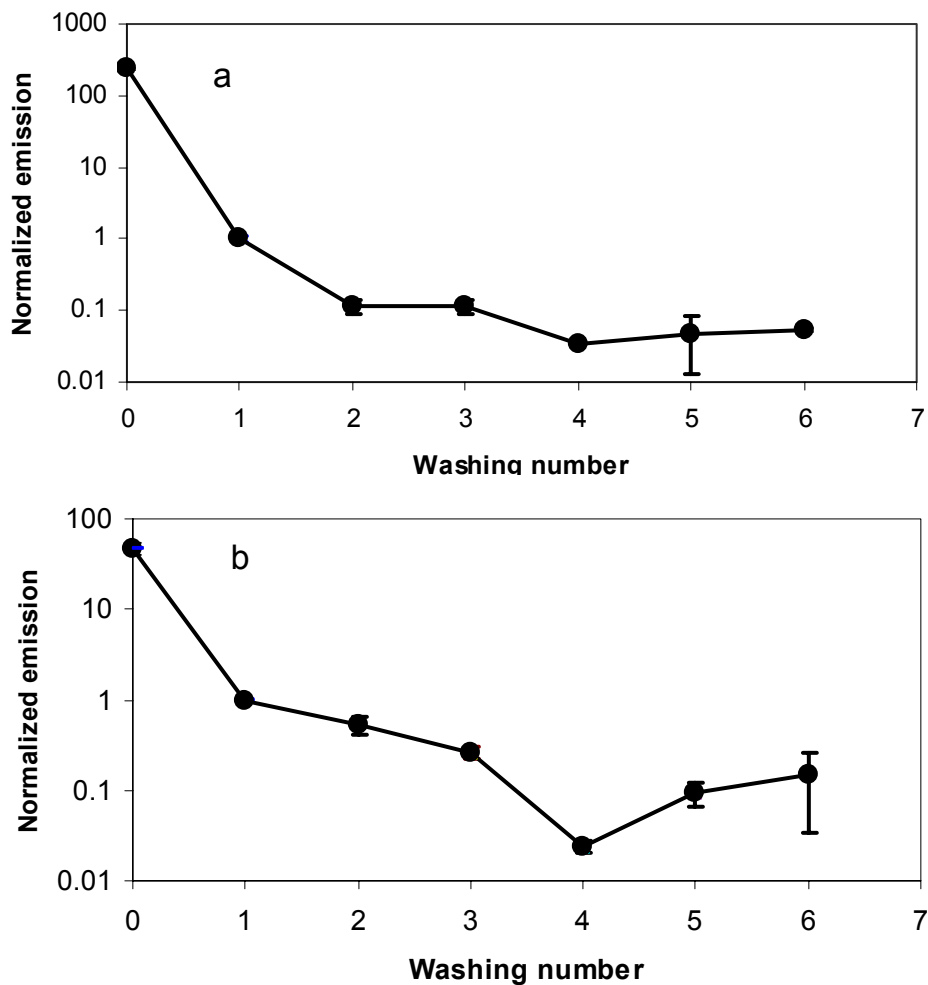


Figure A.2 Washing effect of MNPs treated with fluorescein-labeled anti-mouse IgG. (a) Bare $\gamma\text{-Fe}_2\text{O}_3$ nanoparticles (the amount of added anti-mouse IgG = 160 $\mu\text{g}/\text{mg}$ MNP), (b) APTES-modified and glutaraldehyde-activated $\gamma\text{-Fe}_2\text{O}_3$ nanoparticles (the amount of added anti-mouse IgG = 100 $\mu\text{g}/\text{mg}$ MNP).

Figure A.2 shows that three washing steps in Chapter 3 are reasonable for a quantitative analysis of anti-mouse IgG binding on the MNPs.

A.12 Calculation of anti-mouse IgG binding on MNPs

MNPs interfere in a direct measurement of fluorescence and tend to settle during a fluorescence measurement. The amount of anti-mouse IgG binding on MNPs was measured in an indirect way using the following equation.

$$\begin{aligned} & \text{The amount of bound anti-IgG} \\ &= (\text{Initial quantity of anti-IgG}) - (\text{unreacted quantity of anti-IgG}) \end{aligned} \quad (\text{A.8})$$

An example of calculation is given as follows. 24 μL of the anti-mouse IgG stock (Invitrogen; 2 μg IgG/ μL) was added to a MNP solution. After a reaction following the procedure in Appendix A.3, the MNPs were washed four times with 1 mL of PBS each time. The supernatant of reacting solution along with washing solution was collected. The volume of the combined supernatant solution was measured with a graduated cylinder. It was 4.95 mL. After diluting 2.5 times, the anti-IgG concentration in the diluted solution was determined to be 1.45 μg anti-IgG/mL following the procedure of Appendix A.8 and the standard curve in Figure A.1.

Equation A.8 is rewritten in terms of concentration and volume.

$$\begin{aligned} & \text{The amount of anti-IgG bound on MNPs} \\ &= C_{\text{before}} \times V_{\text{before}} - \text{dilution factor} \times C_{\text{after}} \times V_{\text{after}} \end{aligned} \quad (\text{A.9})$$

where C_{before} : the concentration of the anti-IgG stock solution

V_{before} : the added volume of the anti-IgG stock solution

dilution factor: 2.5 in this example

C_{after} : the concentration of anti-IgG in supernatants after the reaction

V_{after} : the volume of the supernatants after the binding reaction

Therefore,

$$\begin{aligned} & \text{The amount of anti-IgG bound on MNPs} \\ &= 2 \times 24 - (2.5 \times 1.45) \times 4.95 \\ &= 30 \mu\text{g anti-IgG} \end{aligned} \tag{A.10}$$

The amount of MNPs in the solution is 0.20 mg (step 2 of Appendix A.3). Therefore,

$$\begin{aligned} & \text{The concentration of anti-IgG bound on MNPs} \\ &= 30 \mu\text{g anti-IgG}/0.20 \text{ mg MNP} \\ &= 150 \mu\text{g anti-IgG}/\text{mg MNP} \end{aligned} \tag{A.11}$$

150 $\mu\text{g anti-IgG per mg MNPs}$ was calculated to be bound in this way.

A.13 Calculation of MNP-coverage by anti-mouse IgG

Based upon known antibody molecular dimensions (Y-shape; height = 8.5 nm, width = 14.5 nm, thickness = 4.0 nm),¹³² and the surface area of the MNPs being 42.2 m²/g measured by BET method, the MNP-surface coverage by anti-mouse IgG is calculated below. If the anti-IgG has the binding conformation on the side as in Figure A.3, the per-molecule “footprint” should be 34 nm².

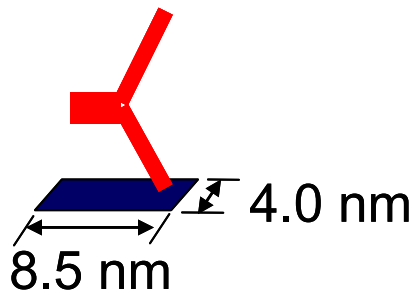


Figure A.3 A schematic configuration of anti-IgG binding on the MNP surface. The footprint is 34 nm² in this case.

Under the assumption of close packing and all surface bound anti-IgGs taking the same conformation as in Figure A.3, division of the particle surface area with the per-molecule footprint provides a maximum number of anti-IgG bound on the MNPs as in Equation A.12.

$$\frac{42.2 \frac{m^2}{g}}{34nm^2} = \frac{1.2 \times 10^{18}}{g} \quad (A.12)$$

The number of anti-IgG molecules is converted to a number of moles number using Avogadro’s number.

$$\frac{1.2 \times 10^{18}}{g} = 2.1 \times 10^{-6} \text{ mole anti-IgG/g MNP} \quad (\text{A.13})$$

Using the molar weight of anti-IgG of 160 kDa,




$$\begin{aligned} & 2.1 \times 10^{-6} \text{ mole anti-IgG/g MNP} \\ &= 3.3 \times 10^{-1} \text{ g anti-IgG/g MNP} \\ &= 3.3 \times 10^2 \text{ } \mu\text{g anti-IgG/mg MNP} \end{aligned} \quad (\text{A.14})$$

Division of the saturated anti-IgG binding in the experiment, 122 μg anti-IgG/mg MNP, with the maximum theoretical value in Equation A.14 provides a MNP-surface coverage by anti-mouse IgG.

$$\begin{aligned} & \text{Max. experimental saturated anti-IgG binding/Max. theoretical anti-IgG binding} \\ &= (1.22 \times 10^2) / (3.3 \times 10^2) \\ &= 0.36 \end{aligned} \quad (\text{A.15})$$

Therefore, a MNP surface coverage by the anti-mouse IgG is 36% under the assumptions. Table 8.2 represents typical configurations of anti-IgGs on the MNP surface and the MNP-surface coverages in each case.

Table A.2 Surface coverage of MNPs as a function of the anti-IgG orientation.

Anti-IgG orientation	Case I 	Case II 	Case III 
Foot print area (nm ²)	34	58	120
Saturated surface coverage (%)	36	61	130

A.14 Calculation of the number of anti-IgGs bound on MNPs

at saturation

Under the assumption that all MNPs have the same size of 32 nm, the number of anti-IgGs bound per MNP at saturation can be calculated as below.

The saturated binding of anti-mouse IgG is 122 μg anti-IgG/mg MNP in Chapter 3. Using the molecular weight of antibody of approx..160 kDa and Avogadro's number, the amount of anti-IgG is converted to a number of anti-IgGs.

$$122 \mu\text{g anti-IgG} = 4.59 \times 10^{14} \text{ anti-IgG} \quad (\text{A.16})$$

The measured surface area (42.2 m^2/g MNP) and the MNP-diameter (32 nm) are used to convert 1 mg of MNPs to a number of MNPs.

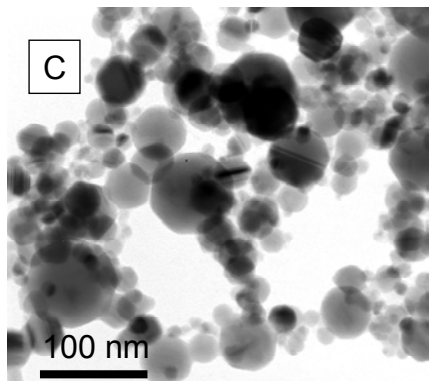
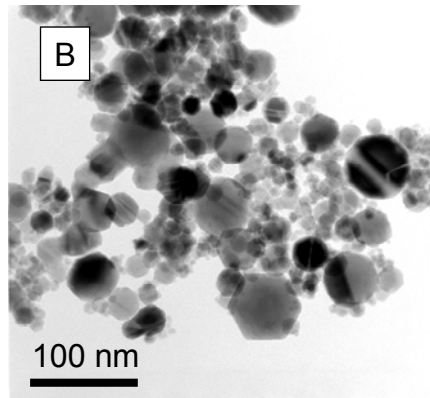
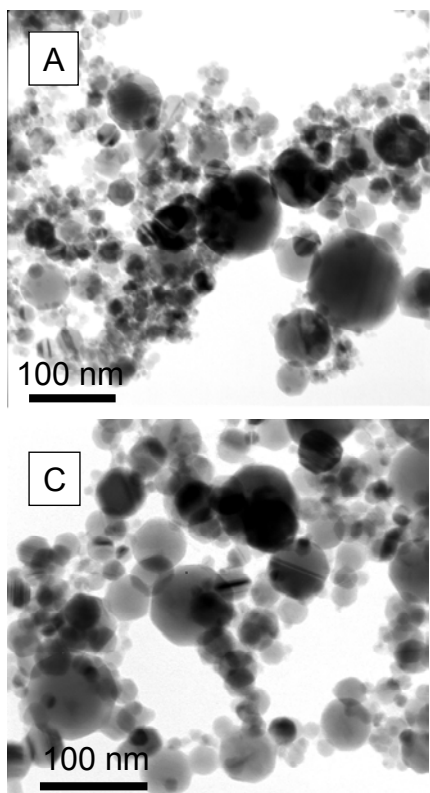
$$1 \text{ mg MNP} = 1.3 \times 10^{13} \text{ MNP} \quad (\text{A.17})$$

Therefore, the saturated binding of anti-IgGs is converted to a number of anti-IgGs per MNP.

$$\begin{aligned} & 122 \mu\text{g anti-IgG/mg MNP} \\ &= 4.59 \times 10^{14} \text{ anti-IgG} / 1.3 \times 10^{13} \text{ MNP} \\ &= 35 \text{ anti-IgG/MNP} \end{aligned} \quad (\text{A.18})$$

Therefore, 35 anti-IgGs are bound per average-size MNP (diameter = 32 nm) in saturated binding.

A.15 TEM images and particle size distributions of iron oxide MNPs



Particles were suspended in PBS (pH 7.4) before being loaded on a TEM grid
A: bare $\gamma\text{-Fe}_2\text{O}_3$
B: APTES-modified $\gamma\text{-Fe}_2\text{O}_3$
C: $\gamma\text{-Fe}_2\text{O}_3$ immobilized with anti-mouse IgG

Figure A.4 Transmission electron microscopy images for bare $\gamma\text{-Fe}_2\text{O}_3$ nanoparticles (A), APTES modified nanoparticles (B), and anti-mouse IgG modified nanoparticles (C) were acquired and are shown below.

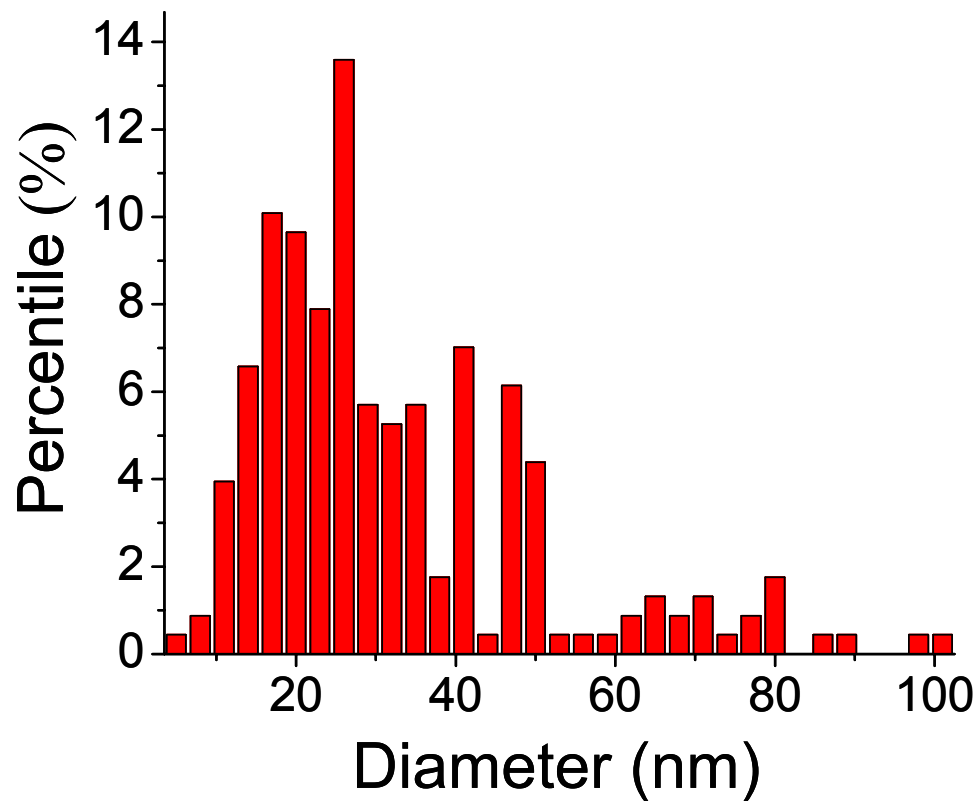


Figure A.5 Particle size distribution of bare $\gamma\text{-Fe}_2\text{O}_3$ nanoparticles. Particle size distributions were created from the TEM images and were invariant with surface preparation. The size distribution constructed from TEM images of bare nanoparticles is shown above.

Appendix B

Appendix B contains protocols for sample preparations in Chapter 4.

B.1 Protocol for phosphonic acid modification

1. Mix methanol and double distilled water with 4:1 ratio.
2. Add phenyl phosphonic acid (PPA) to be 4 mM in the mixed solvent.
(Ex) PPA 0.632 g in 1.0 L of the mixed solvent
3. Adjust the pH of the PPA solution to be 4.
4. Add metal oxide nanoparticles at a concentration of 1.0 mg per 1.0 mL of the solvent.
5. Stir in room temperature for 15 hours.
6. Centrifuge the reacted nanoparticles.
(Ex) Centrifuge for 10 min at $10,000 \times g$ (approx. 7000 rpm) using a 300 mL-capacity Nalgene (Rochester, NY) tube in a centrifuge (Dr. Nam Sun Wang's lab).
Note: Be careful not to break the centrifuge tube. Centrifuge tubes tend to be broken by either loading too much sample in a centrifuge tube or setting up too high centrifugation speed.
7. Add 5-10 mL of pure mixed solvent (Methanaol:Water = 4:1 v/v) not containing PPA. Resuspend the centrifuge particles by vortexing.
8. Transfer the particle suspension in 1.5 mL-centrifuge tubes.
9. Centrifuge for 4 minutes at 13,400 rpm in a centrifuge (Minispin, Eppendorf, Hamburg, Germany; Dr. Doug English's Lab).

10. Discard the supernatant.
11. Add 1 mL of the pure mixed solvent.
12. Vortex briefly to suspend the particles.
13. Repeat steps 9-12 seven times.
14. Discard the supernatant. Dry the particles in a vacuum oven (1 mbar, 120 °C) for 15 hours.
15. Store the dried particles in a desiccator.
Characterize the particles with XPS.

B.2 Protocol for reaction with N,O-bis(trimethylsilyl)trifluoroacetamide (BSTFA)

1. Add metal oxide nanoparticles in a RB flask.
2. Purge air in the flask with nitrogen.
3. Add dry toluene to the particles at a concentration of 10 mg/mL.
4. Sonicate the particles in a bath sonicator for 10 minutes.
5. Add BSTFA in one tenth volume of dry toluene.
(Ex) Add 0.2 mL BSTFA to particle-suspended 2 mL dry toluene.
6. Stir for 2 hours.
7. Transfer the particle suspension in 1.5 mL-centrifuge tubes.
8. Centrifuge for 4 minutes at 13,400 rpm in a centrifuge (Minispin, Eppendorf, Hamburg, Germany; Dr. Doug English's Lab).
10. Discard the supernatant.
11. Add 1 mL of the pure dry toluene.
12. Vortex briefly to suspend the particles.
13. Repeat steps 9-12 four times.
14. Discard the supernatant. Dry the particles in a vacuum oven (1 mbar, 120 °C) overnight.
15. Store the dried particles in a desiccator.
Characterize the particles with XPS.

Appendix C

Appendix C describes protocols in Chapters 5. Operate in a Laminar flow bench to maintain sterility.

C.1 Cell culture medium compositions

C.1.1 Ampicillin

Ampicillin is an antibiotics used to keep sterility in the cell culture. *E. coli* 105 harboring pBR 322 (Ap^R) is ampicillin-resistant. The final concentration of ampicillin in a typical cell culture medium in Chapters 5 and 6 was 100 µg ampicillin/mL of medium. One thousand time concentrated (1000 X; 100 mg/mL) ampicillin stock solution is prepared for afterward applications.

1. Dissolve 2.5 g of ampicillin powder in 25 mL of autoclaved distilled water.
2. Sterilize the ampicillin solution by filtering through a 0.20 µm pore size filter (Millipore, Billerica, MA).

Note: Ampicillin is heat sensitive. Do not sterilize an ampicillin solution by autoclaving.

3. Divide the 25 mL filter-sterilized ampicillin solution into 1 mL aliquots. Put each aliquot in an autoclaved 1.5 mL-capacity centrifuge tube.
4. Label the ampicillin aliquots in the centrifuge tubes. (Ex) 1000X Ap
5. Store the ampicillin aliquots in a -20 °C refrigerator until further usage.

C.1.2 Luria Bertani (LB) medium

Bacto tryptone	10 g
Bacto yeast extract	5 g
NaCl	10 g
dH ₂ O (distilled water)	1 liter volume

1. Mix all ingredients together and adjust pH to 7.0 with 5 N NaOH (approx. 0.4 mL/liter).
2. Autoclave for 20 min.
3. After cooling down the autoclaved medium, add 1 mL of 1000X antibiotics (ampicillin) solution.

For agar plates,

1. In addition to the ingredients mentioned for liquid LB medium, add 15 g (for a harder agar plate, 20 g) agar to the liquid LB medium.
2. Autoclave for 20 minutes. Keep in mind to leave a magnetic bar in the medium.
3. Cool down the medium to about 45 OC. Then, add 1 mL of 1000X ampicillin solution.
4. Mix the antibiotics-added LB medium for a minute on a magnetic stirring plate.
5. Pour out the LB-agar medium to a 10 cm diameter petri dish. You can make about forty agar plates using 1 L LB-agar medium.
6. Let the LB-agar medium in petri dishes cooled down and solidified overnight.
7. Store the solidified agar plates in a refrigerator until further usage.

C.1.3 M9 medium

Medium composition

Sterile 10X Salt*	100 mL
20% glucose	20 mL
0.01 M CaCl ₂ ^a	10 mL
0.1 M MgSO ₄ ^a	10 mL
20% Casamino acids	20 mL
dH ₂ O ^a	840 mL

Note: Autoclave each ingredients separately, since sediments may form when they are mixed together and autoclaved. Mix the ingredients to make M9 medium after cooling down the separately-autoclaved ingredients.

^aNote: These ingredients may be changed in accordance with the different kind of M9 medium in Table 6.1 of Chapter 6.

* Salt Mix 10X

Na ₂ HPO ₄	70 g
or (Na ₂ HPO ₄ ·7H ₂ O)	(132 g)
KH ₂ PO ₄	30 g
NaCl	5 g
NH ₄ Cl	10 g
H ₂ O	1000 mL

C.1.4 Preparation of a MNP solution

1. Add a desired amount of MNPs in a glass vial. Add distilled water.
2. Sonicate the particles in the solution using a tip sonicator (Dr. Nam Sun Wang's lab) or a bath sonicator (Dr. Doug English's lab or Dr. Lyle Isaacs' lab) for several minutes.
3. Autoclave for 20 minutes.
4. Add the autoclaved MNP solution to cell culture medium (M9 medium) between step 4 and 5 in Appendix C.2 (*E. coli* cell culture).

C.2 *E. coli* cell culture

1 mL of 30% glycerol stock of *E. coli* JM 105 harboring pBR 322 (Ap^R) was a gift from the laboratory of Dr. William Bentley at the Department of Chemical and Biomolecular Engineering, University of Maryland. Divide the 1 mL glycerol stock into ten 100 mL aliquots and store the aliquots in a -80 °C refrigerator. Thaw and use one aliquot each time for a series of X-ray scattering experiments.

1. Sterilize a wire loop in a flame for about 10 seconds. Cool down the hot wire in the air. Dip the loop into the glycerol stock. Streak the loop on solid agar of LB medium including 100 µg ampicillin/L in a petri dish (diameter = 10 cm).
Note: Record the date of incubation, *E. coli* strain name, and the researcher name on the bottom of the petri dish near the rim.
2. Put the agar plate upside down in a 37 °C incubator. Let the *E. coli* grow for a day or two in the incubator. Store the agar plate in a refrigerator after the incubation. *E. coli* on an agar plate are viable up to a few weeks in a refrigerator. It is recommended to use *E. coli* on an agar plate within one week from preparation time.
Note: You can transfer *E. coli* to another fresh agar plate by taking a colony of *E. coli* with a wire loop and streaking it on the fresh agar plate.
3. Take a colony with a flame-sterilized wire loop from an agar plate and inoculate it to a 5 mL LB medium in a 15 mL-capacity centrifuge tube.
4. Incubate the inoculated LB medium at 100 rpm for 6 hours in a 37 °C incubator.

5. Inoculate 250 mL M9 medium in a 500 mL-capacity flask with the grown *E. coli* (5 mL) in a centrifuge tube.
6. Incubate the inoculated 250 mL M9 medium at 100 rpm for 12 hours in a 37 °C incubator.
7. Decant the grown *E. coli* to 500 mL or 1000 mL-capacity three necked flask.
8. Start an X-ray scattering experiment.

C.3 Continuous *E. coli* growth and *in situ* X-ray scattering

Continuous *E. coli* culture is used for *in situ* X-ray scattering. A detailed procedure is described as follows.

1. Apply vacuum grease at the junction between the RB flask and the stirring rod to prevent overheating by shear force during stirring.
2. Autoclave all the equipments including a 500 mL-capacity three neck RB flask, a glass vial for X-ray scattering, tubings, and an air filter.
3. Set up all the equipment for continuous growth of *E. coli* and *in situ* X-ray scattering. Check the inlet and outlet pump flow rate to be the same at approximately 100 mL per hour.
4. Check the air flow rate to be approx. 3 vvm (vessel volume per minute; 3 vvm = 750 mL per minute) using a bubble flowmeter.
5. Set up a motor for stirring and a water bath for keeping 37 °C during the *E. coli* culture.
6. Decant *E. coli* grown in 250 mL M9 medium to the three neck RB flask.
7. Start continuous growth of *E. coli* and *in situ* X-ray scattering.

C.4 Washout condition in continuous culture of *E. coli*

A steady state CSTR (continuous-flow stirred tank reactor) material balance is given as equation C.1.¹¹⁶

$$Dx_f = (D - \mu)x \quad (\text{C.1})$$

where, D = the dilution rate, F/V_R

F = volumetric flow rate of feed and effluent liquid streams

V_R = total volume of culture within the reactor

μ = specific grow rate of the cells

x = mass concentration of the cells within the reactor

x_f = mass concentration of the cells in the feed

The prepared feed stream is a sterile cell growth medium, so that $x_f = 0$.

Non-zero cell concentration can be maintained only when,

$$D = \mu \quad (\text{C.2})$$

Equation C.2 reveals that the specific cell growth rate is equal to the dilution rate in a steady state CSTR condition. Equation C.2 also displays that the dilution rate should not exceed the maximum specific cell growth rate.

The maximum specific cell growth rate was determined in a batch culture of *E. coli* in M9 medium. The growth curve is given in Figure C.1.

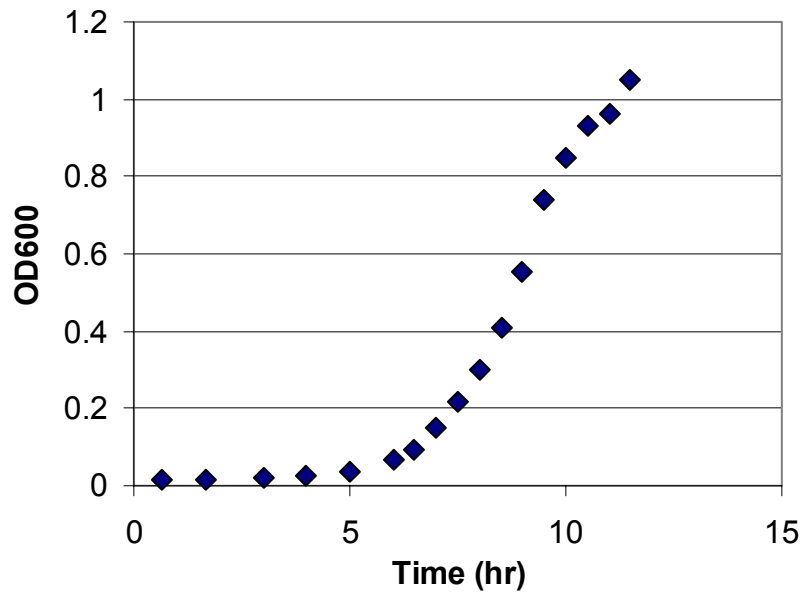


Figure C.1 Growth curve of *E. coli* in M9 medium in a batch culture. OD₆₀₀ is optical density of cells at 600 nm.

The specific growth rate (μ) is defined as follows.

$$\mu = \frac{1}{x} \frac{dx}{dt} = \frac{d \ln x}{dt} \quad (\text{C.3})$$

where x = mass concentration of the cells within the reactor

The application of Equation C.3 to the growth curve results in Figure C.2.

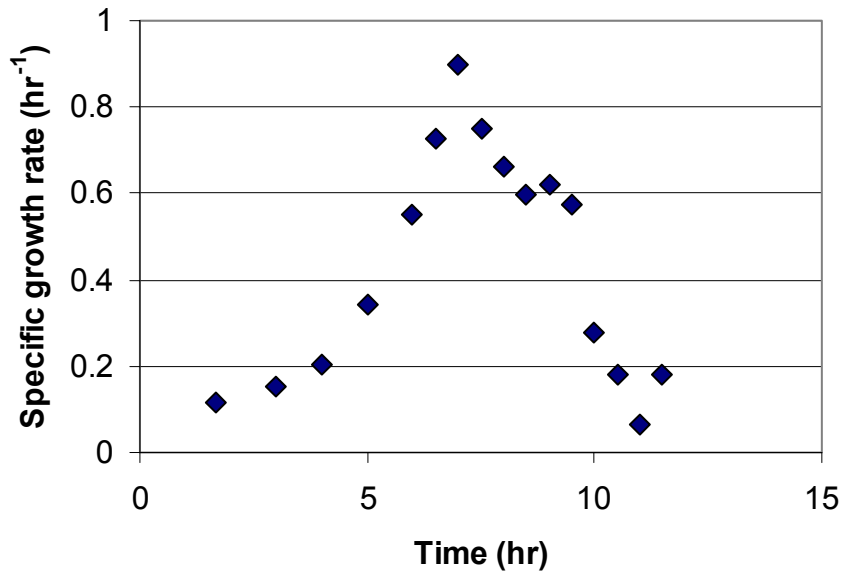


Figure C.2 Specific growth rate as a function of the *E. coli* culture time.

The maximum specific growth rate from Figure C.3 is 0.90 hr^{-1} . The maximum dilution rate is the same with 0.90 hr^{-1} in accordance to Equation C.2. Considering the definition of the dilution rate and the total volume of culture in the reactor of 250 mL, the maximum dilution rate 0.90 hr^{-1} corresponds to the maximum flow rate of 225 mL/hr. This analysis displays that the continuous growth of *E. coli* should be operated within 225 mL/hr of the volumetric flow rate. The procedures described in operations of Chapter 5 used a volumetric flow rate of 100 mL per hour within the limit of 225 mL/hr.

C.4 X-ray scattering

C.4.1 Bragg's Law

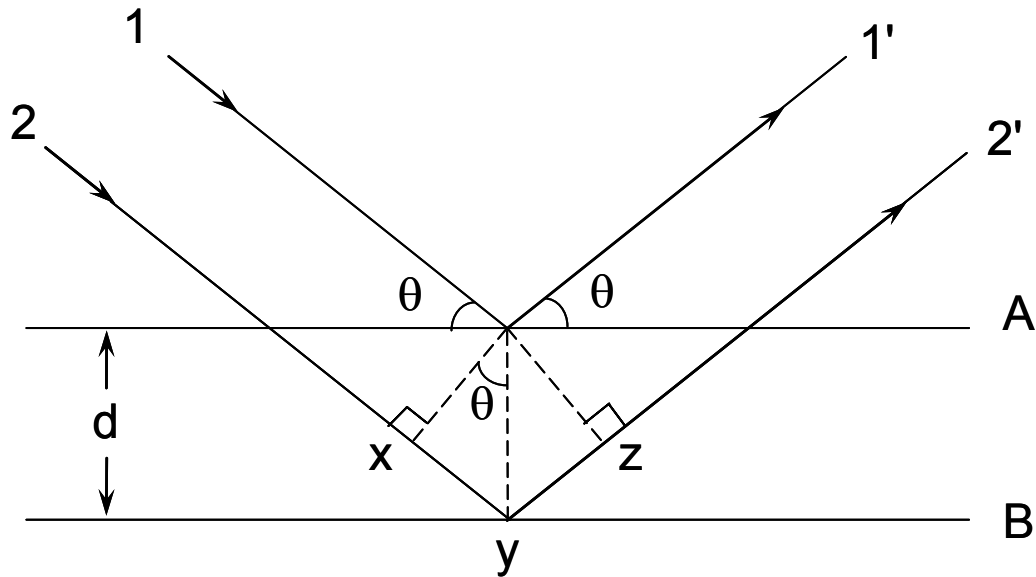


Figure C.3 Derivation of Bragg's law for X-ray scattering.¹⁸⁰

A,B: planes of a crystal structure

d : d-spacing, the perpendicular spacing between two adjacent planes of a crystal structure.

θ : incident angle of the X-rays, same as the reflection angle of the X-rays

xy: distance between x and y

yz: distance between y and z

xyz: added value of xy and yz

1, 2: incident beams of the X-rays

1', 2': reflected beams of the X-rays

Some of the X-rays are reflected from the plane A at the same angle of reflection with the angle of incidence, θ . The rest are reflected from the adjacent plane, B. A constructive interference between the two reflected beams occurs if and only if the following equations are satisfied. From Figure C.3

$$xy = yz = d \sin \theta \quad (\text{C.4})$$

where d : d-spacing, the perpendicular spacing between two adjacent planes of a crystal structure.

θ : incident angle of the X-rays

Thus,

$$xyz = 2d \sin \theta \quad (\text{C.5})$$

For a constructive interference,

$$xyz = n\lambda \quad (\because n = 1, 2, 3 \dots) \quad (\text{C.6})$$

where λ : wavelength of the X-rays, 1.5418 Å in $K\alpha$ radiation

Therefore,

$$n\lambda = 2d \sin \theta \quad (\text{C.7})$$

Customarily, n is set to one. So, Bragg's Law is given in the final form as such:

$$\lambda = 2d \sin \theta \quad (\text{C.8})$$

The q vector is often used in description of X-ray scattering results instead of the incident angle θ . The q vector has an inverse relationship with the d-spacing according to the following definition.

$$q = \frac{2\pi}{d} = \frac{4\pi \sin \theta}{\lambda} \quad (\text{C.9})$$

Rigaku in Room 2219, James Patterson Building (Dr. Luz Martínez-Miranda)

Check the power of X-rays from the control panel and record the condition and time on a Log book.

(Ex) Nov 18 2004 50 kV 100 mA 0.502 mPa

C.4.1 Increasing and decreasing the X-ray power

When you increase the power to the operation power in Chapters 5 and 6 of 60 kV and 150 mA, follow these steps. When you decrease the power, you can follow the reverse way.

20 kV 10 mA 5 min

30 kV 10 mA 5 min

30 kV 50 mA 5 min

30 kV 100 mA 5 min

40 kV 100 mA 5 min

50 kV 100 mA 5 min

60 kV 100 mA 5 min

60 kV 150 mA 5 min

Note: Make sure the pressure gauge in the control panel does not exceed 0.11 mPa.

C.4.2 Calibration

X-ray machine is calibrated using silicon standard (peak at $2\theta = 28.4^\circ$).

Useful commands:

ctrl-c = stop scanning

resume=resume scanning

Calibration example

(Ex) a2scan tth 25 30 phi 12.5 15 50 20

Note: tth = two theta scan

25 30 = scan range of two theta

phi = phi scan

12.5 15 = scan range of phi, half of the two theta scan range

50 = number of data points in the scan range

20 = time (second) taken for each data acquisition

If a peak is found other than at $2\theta = 28.4^\circ$, correct the X-ray machine.

(Ex) When a peak was found at $2\theta = 27.9^\circ$,

mv tth 27.9

set tth 28.4

Note: mv tth 27.9 = move the two theta arm to 27.9°

set tth 28.4 = set the present two theta value as 28.4°

C.4.3 Scanning protocol

1. Close the shutter of the X-ray control panel (Red light of the shutter control panel is OFF now).

Note: When you open the door of the X-ray room without closing the shutter, X-rays will be shut down automatically.

2. Open the door of the X-ray room and go inside.
3. Adjust the sample loading plate all the way down.
4. Load the sample holder in the sample loading plate.
5. Load the permanent magnets if necessary.

Adjust the distance between the permanent magnets by inserting an aluminum bar which has a thickness corresponding to a specific magnetic field strength.

6. Load the vial connected with the tubing inside the sample holder.
7. Start pumping *E. coli* culture in and out from the sample vial.
8. Wait for approximately 20 minutes until a steady state is reached.
9. Go out of the X-ray room and shut the door of the X-ray operation room.
10. Open the shutter of the X-ray control panel (Red light of the shutter control panel is ON now).
11. Name the file you are about to scan, so that you can recognize it easily later.

(Ex) newfile SiFe40_0mT-CaMg_120804

Note: SiFe40: 40 mg of SiO₂/Fe₂O₃ per L of M9 medium

0 mT: magnetic field strength of 0 mT

CaMg: Ca and Mg are doubled in M9 medium

120804: running date is Dec 18 2004

12. Run the scan.

(Ex) a2scan tth 3.0 12.0 phi 1.5 6.0 90 40

Note: tth = two theta scan

3.0 12.0 = scan range of two theta

phi = phi scan

1.5 6.0 = scan range of phi, half of the two theta scan range

90 = number of data points in the scan range

40 = time (second) taken for each data acquisition

13. Record the name of the file and the scanning condition on a logbook.

14. When one run is finished, repeat steps 1-2. If necessary, adjust the magnetic field strength by changing the distance between the two magnets in the sample holder.

Repeat Steps 8-12.

15. When all the scans are finished, clean the X-ray area. Bring the X-ray power all the down to 20 kV and 10 mA following the order in Appendix C.4.1.

C.4.4 X-ray scattering data processing

1. Click open FTP.
2. In session properties window, type in “jmpatt-209.umd.edu” in Host name/address, “guest” in user ID, and a password. Click “OK”.
3. Enter into the user’s directory.
4. Transfer a file(s) to the user’s own computer.
5. Open Origin 6.0.
6. File > Import > Single ASCII
7. Import a file(s) into Origin 6.0 by choosing the file(s).
8. In the data file, the first column contains two theta value and the last column includes.

X-ray scattering intensity. Neglect the other columns.

Copy the first column and the last column to a new data sheet.

9. Two theta values can be converted to q values as follows.
 - 9a. Change the name of two theta column head to “tth”
 - 9b. Choose a vacant column.
 - 9c. Column > Set column values
 - 9d. Type in “2*pi*2*sin(pi/180*col(tth)/2)/1.54”,

since $q = \frac{2\pi}{d} = \frac{4\pi \sin \theta}{\lambda}$, $\lambda = 1.54 \text{ \AA}$, and two theta values in degree needs to be

converted to radian values for calculation of $\sin \theta$.

10. Choose two columns, either t th column & X-ray scattering data column or q column & X-ray scattering data column. Make a graph. Add another graph to the graph if needed.

C.5 Growth studies on *E. coli* after exposure to the X-rays

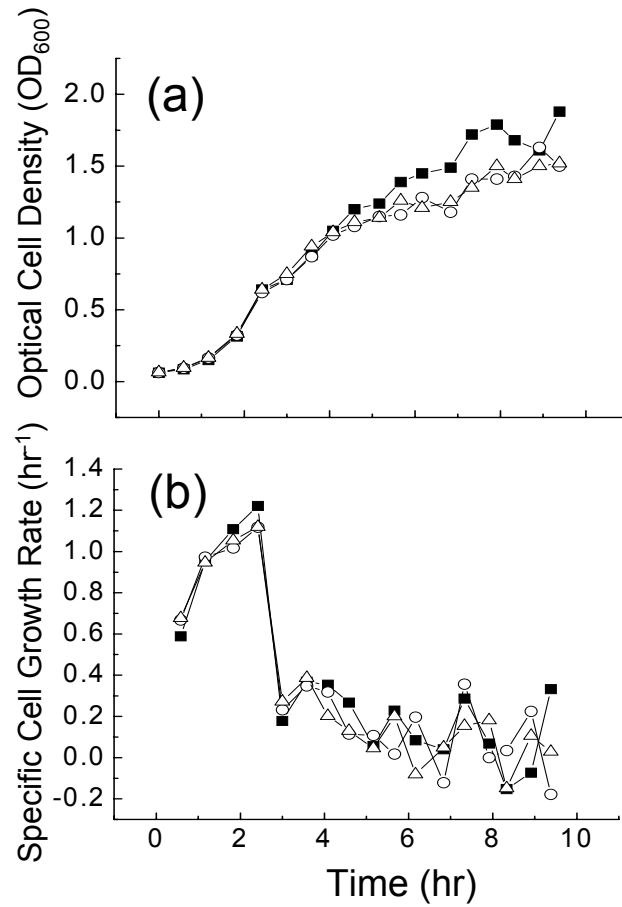


Figure C.4 Comparison of growth curves of *E. coli* in batch cultures in LB medium. The seeds were sampled from different continuous culture conditions; ■: Neither X-rays nor magnetic fields were applied, Δ: only X-rays were applied, and ○: X-rays and 423 mT of magnetic field strength were applied. Magnetic nanoparticles were not added to the continuous cultures from which the seeds were taken.

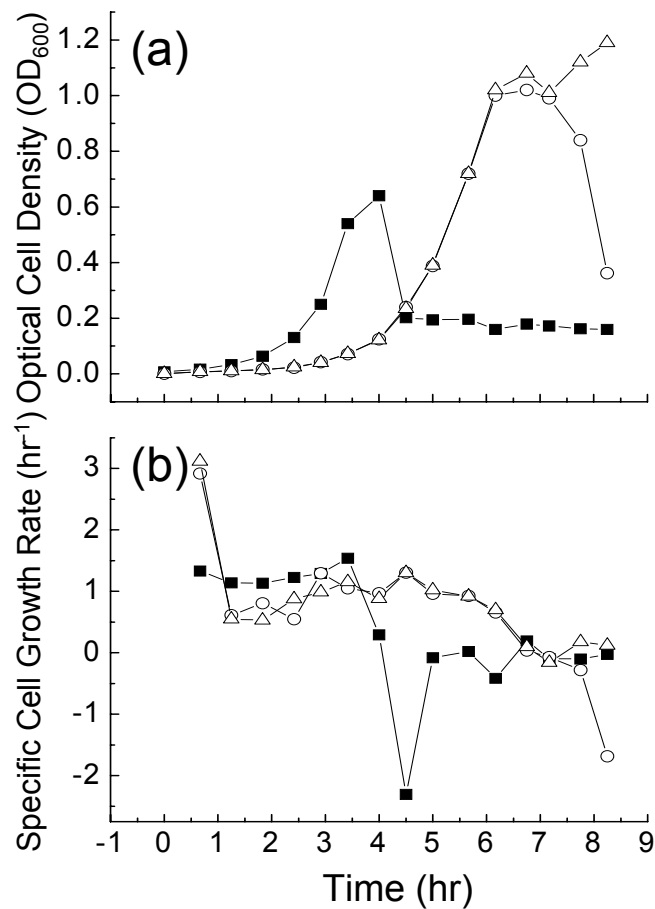


Figure C.5 Comparison of growth curves of *E. coli* in batch cultures in LB medium. The seeds were sampled from different continuous culture conditions: ■: Neither X-rays nor magnetic fields were applied, Δ: only X-rays were applied, and ○: X-rays and 423 mT of magnetic field strength were applied. 20 mg/l of SiO₂/γ-Fe₂O₃ particles was added to the continuous cultures, from which the seeds were taken.

C.6 X-ray scattering study of the interactions between magnetic nanoparticles and living cell membranes: Effect of concentrations of magnetic nanoparticles and divalent salt ions

Chapter 5 describes XRS results for 0 and 40 mg MNP/L concentrations as a function of applied magnetic field strengths. One concentration of MNP, 40 mg MNP/L, was used in the XRS works reported in Chapter 5 to see the role of the presence of MNPs in an *E. coli* culture. Therefore, there is a need to investigate the effects of other MNP concentrations on the XRS results. In addition to 0 and 40 mg MNP/L, MNP concentrations of 20 and 100 mg MNP/L were examined to see the effects of particle concentrations on XRS-detected peaks.

Divalent ions in M9 medium such as Ca^{2+} , Mg^{2+} , and SO_4^{2-} have a large effect on ionic strength of the medium, and thus on particle agglomerations and cell membranes. Three sets of divalent concentration were used in order to see the effects of the divalent ion concentrations on XRS peaks (Table C.1). The M9 medium used in Chapter 5 was M9 type II in Table C.1. Figures C.5, C.6, and C.7 display representative XRS results at different MNP concentrations up to 100 mg MNP/L. XRS results at different MNP concentrations were shown on the same graph with the same scale for comparisons. XRS peak positions are shown in Table C.2, C.3, and C.4.

M9 type I medium did not show a peak at around 0.52 \AA^{-1} at MNP concentrations of 0 and 20 mg MNP/L as shown in Figure C.5.

Table C.1 Medium composition of three types of M9 media used in XRS studies

	Type I (mL)	Type II (mL)	Type III (mL)
sterile 10X salt	100	100	100
20% glucose	20	20	20
0.01 M CaCl ₂	10	20	20
0.1 M MgCl ₂	10	20	0
0.1 M MgSO ₄	0	0	20
20% casamino acids	20	20	20
distilled H ₂ O	840	820	820

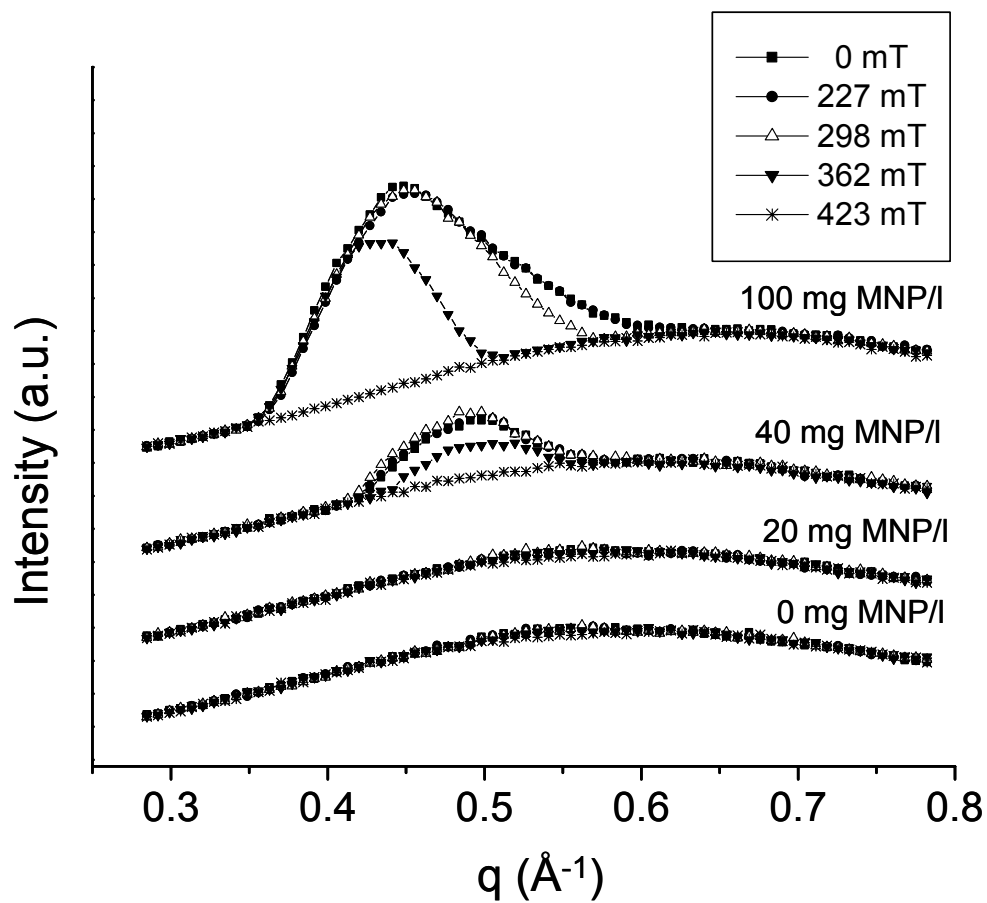


Figure C.6 XRS data of M9 medium type I as a function of MNP concentration up to 100 mg/L.

Table C.2 Peak positions of XRS data of M9 medium type I as a function of magnetic field strength and MNP concentration.

	q (\AA^{-1})			
	0 mg/L	20 mg/L	40 mg/L	100 mg/L
0 mT	N/A	N/A	0.49	0.45
227 mT	N/A	N/A	0.49	0.45
298 mT	N/A	N/A	0.49	0.45
362 mT	N/A	N/A	0.49	0.425
423 mT	N/A	N/A	N/A	N/A

XRS peaks at around 0.49 \AA^{-1} appeared in the presence of MNPs at 40 mg MNP/L. The peaks grew bigger in intensity and were shifted to the smaller side of q at 100 mg MNP/L.

M9 type II medium displays XRS results as a function of the concentrations of MNPs including the results reported in Chapter 5. The peak positions at 0.52 \AA^{-1} at 0 mg MNP/L were not shifted in the presence of MNPs at 20 mg MNP/L. 40 mg MNP/L caused the sharp peak shifted to the lower side of q . Basically, 100 mg MNP/L concentration of MNPs showed the same peak positions with XRS results at 40 mg MNP/L.

Figure C.7 shows XRS results for MNPs in M9 type III medium. Distinct peaks were detected even at 0 mg MNP/L. At 0 mg MNP/L, the sharp peak positions were shifted from 0.52 \AA^{-1} in M9 type II to 0.46 \AA^{-1} in M9 type III in the applied magnetic field strengths of 0, 227, and 298 mT. 362 mT of applied magnetic field strength shifted the sharp peak to 0.43 \AA^{-1} , whereas no peak shift was observed in M9 type I and M9 type II at 362 mT and at 0 mg MNP/L. XRS data at 20 mg MNP/L showed almost same peak positions with the case when no MNPs are present in the cell culture. When 40 mg MNP/L was present in the cell culture medium, the XRS peaks grew both in intensities and peak widths. The sharp peaks at 0, 227, and 298 mT were shifted to 0.40 \AA^{-1} , while 362 mT showed the peak at 0.37 \AA^{-1} . Interestingly, 100 mg MNP/L of MNP concentration shifted back the sharp peak positions to the higher side of q . This may be explained by the highest ionic strength of the M9 type III and the presence of MNPs at the highest concentration

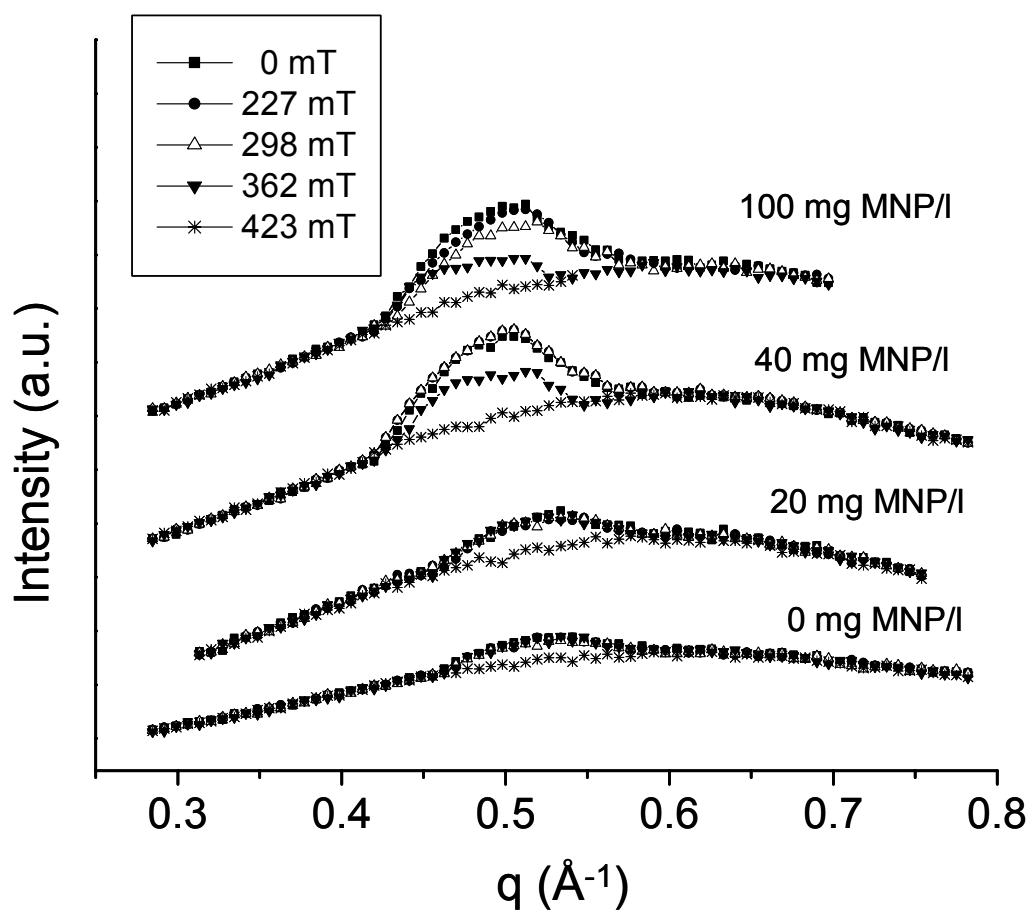


Figure C.7 XRS data of M9 medium type II as a function of MNP concentration up to 100 mg/L.

Table C.3 Peak positions of XRS data of M9 medium type II as a function of magnetic field strength and MNP concentration.

	q (\AA^{-1})			
	0 mg/L	20 mg/L	40 mg/L	100 mg/L
0 mT	0.528	0.52	0.485	0.49
227 mT	0.528	0.52	0.485	0.49
298 mT	0.528	0.52	0.485	0.49
			0.481	
362 mT	0.528	0.52	0.485	0.475
			0.459	
423 mT	N/A	N/A	N/A	N/A
			N/A	

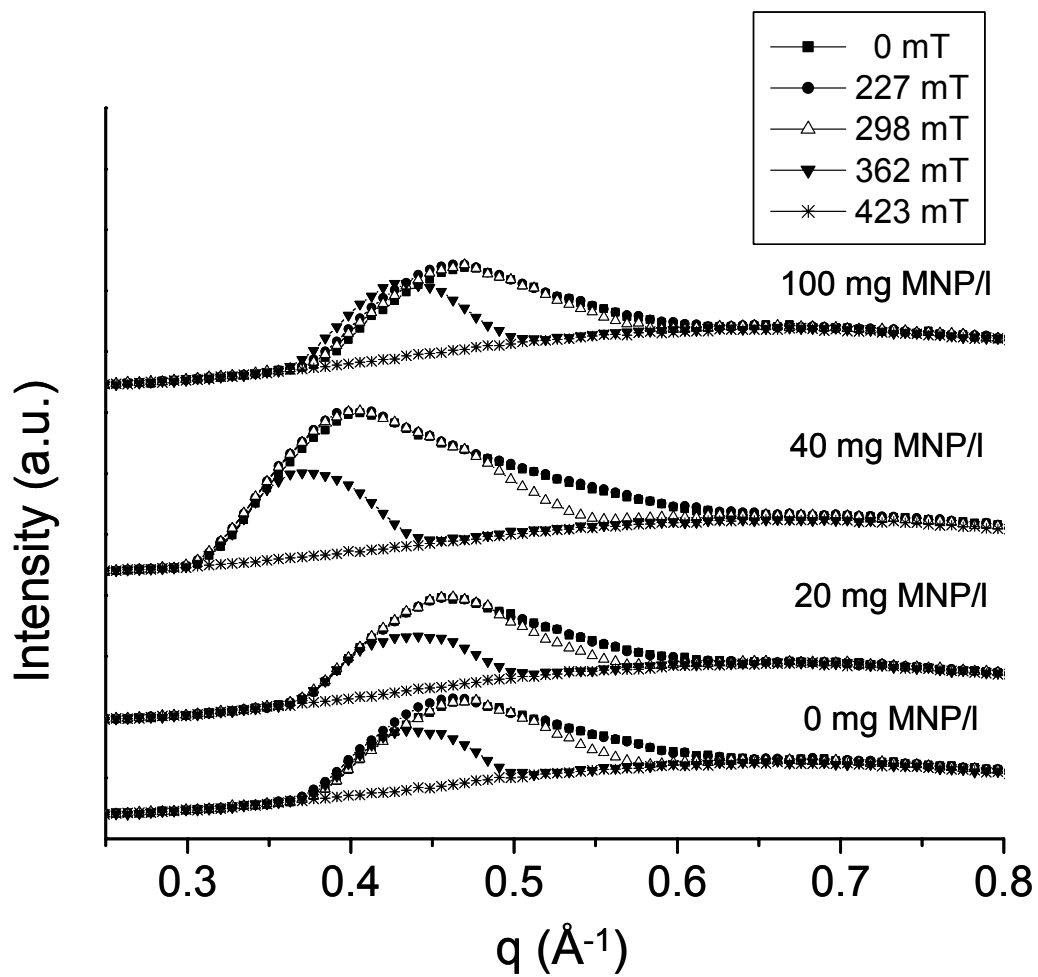


Figure C.8 XRS data of M9 medium type III as a function of MNP concentration up to 100 mg/L.

Table C.4 Peak positions of XRS data of M9 medium type III as a function of magnetic field strength and MNP concentration.

	q (\AA^{-1})			
	0 mg/L	20 mg/L	40 mg/L	100 mg/L
0 mT	0.47	0.47	0.39	0.45
	0.46	0.46	0.399	
227 mT	0.47	0.47	0.39	0.45
	0.46	0.46		
298 mT	0.47	0.47	0.39	0.45
	0.46	0.46		
362 mT			0.375	
	0.43	0.43	0.385	0.40
	0.43	0.43	0.365	0.42
			0.370	
423 mT	N/A	N/A	N/A	N/A

Particle agglomeration arising from high ionic strength environment did likely induce the shift-back effect at 100 mg MNP/L. Figure C.8 shows d spacing as a function of magnetic field strength at different MNP concentrations.

Distinctive peak shifts of the sharp peak were observed at 362 mT. The sharp peak positions at 0 and 362 mT are shown in Figure C.9 to demonstrate M9 medium type-dependent shifts of the sharp peak at 362 mT. Doubling the amount of Ca^{2+} and Mg^{2+} in M9 medium shifted the d spacing to the smaller side (Figure C.9 (a)). The presence of SO_4^{2-} in cell culture medium led to an increased d spacing (Figure C.9 (b)).

The diffuse peak at 0.61 \AA^{-1} did not show a peak shift in M9 type I and II, except the case of 100 mg MNP/L in M9 type I at which the peak was shifted to 0.64. The presence of SO_4^{2-} caused the diffuse peak shifted to 0.67 \AA^{-1} .

In this Appendix, the effects of MNP concentrations up to 100 mg/L and divalent ion concentrations on XRS results are shown. In M9 type I, the sharp peak was not present at 0 and 20 mg MNP/L and began to appear at 40 mg MNP/L. The peaks were shifted to the lower side of q at 100 mg/L. In M9 type II, 40 mg/L is a critical concentration, at which the sharp peak was shifted to the lower side of q and additional presence of MNPs did not change the peak position further. In M9 type III, the sharp peak position was shifted to the lower side of q at 40 mg/L and was shifted back to the higher side of q with the increase of the MNP concentration to 100 mg/L. This phenomenon was likely related to the presence of high ionic concentration in the cell culture medium. As shown in Figure C.8, the difference of the XRS-determined d spacing between at 40 mg MNP/L and at 100 mg MNP/L is

dependent upon the ionic strength of cell culture medium. The d spacing was increased when the MNP concentration was increased from 40 to 100 mg MNP/L in M9 type I medium with low ionic strength. In M9 medium type II with middle ionic strength, the d spacing was almost identical between at 40 mg/L and at 100 mg/L. The presence of the high ionic strength of M9 medium type III led to a decrease in the d spacing when the MNP concentration was increased from 40 to 100 mg/L.

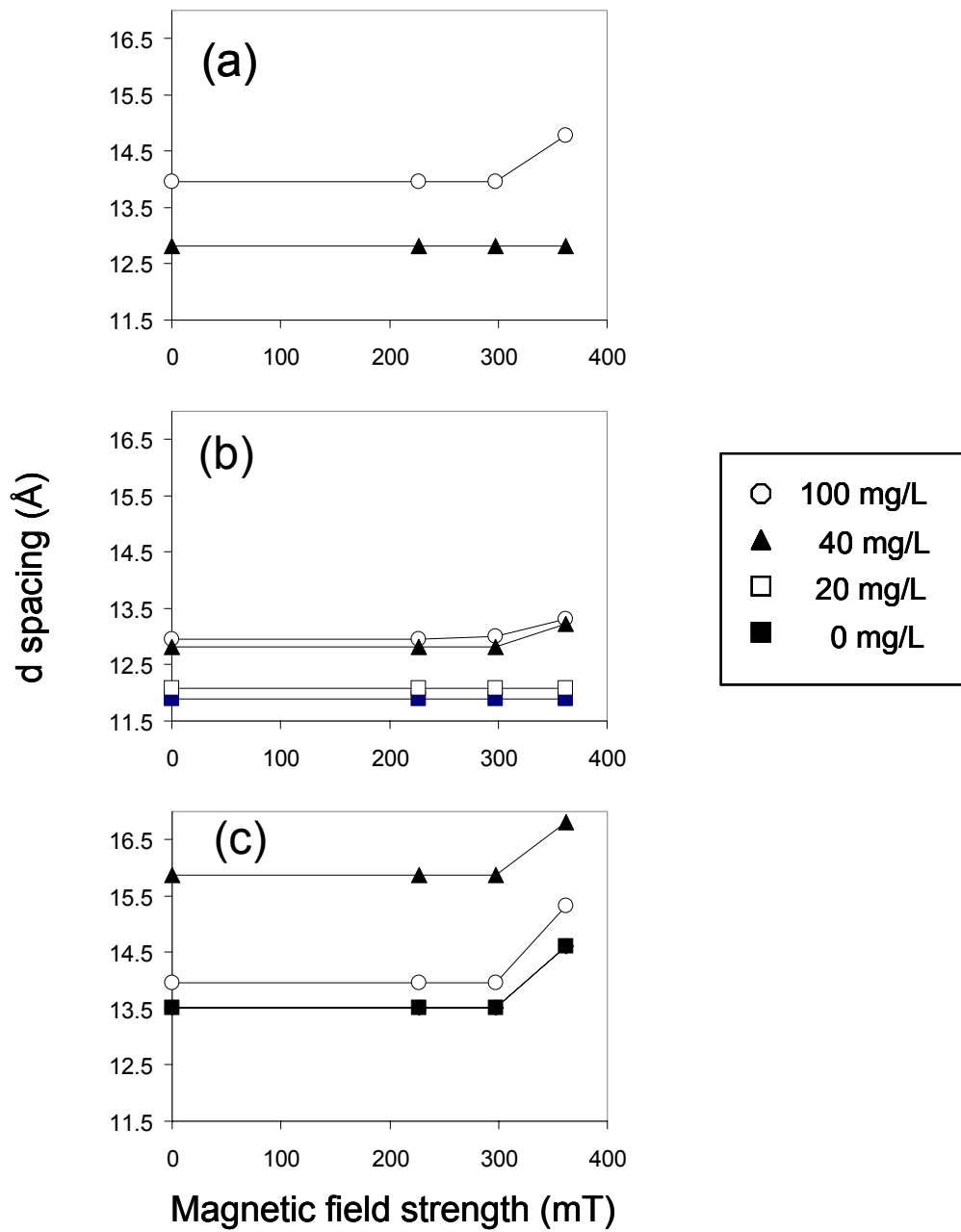


Figure C.9 d spacing (Å) as a function of applied magnetic field strengths at different MNP concentrations. (a) M9 type I, (b) M9 type II, (c) M9 type III.

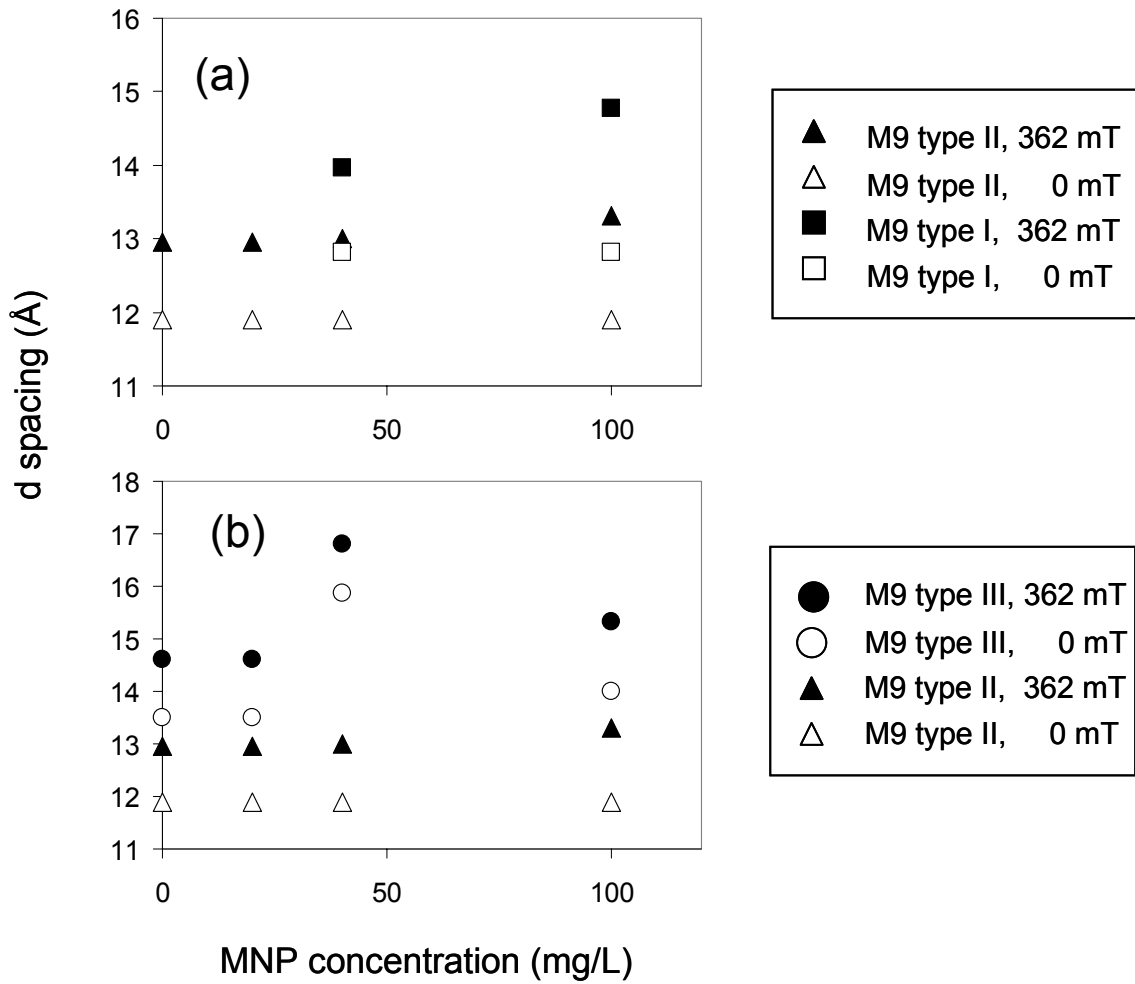


Figure C.10 d spacing (Å) as a function of MNP concentration in the applied magnetic field strength of 0 and 362 mT. (a) Effect of concentrations of cationic divalent ions, Ca^{2+} and Mg^{2+} , (b) effect of anionic divalent ion, SO_4^{2-} .

References

- (1) Katz, E.; Willner, I., Integrated nanoparticle-biomolecule hybrid systems: synthesis, properties, and applications. *Angew Chem Int Ed* **2004**, 43, (45), 6042-6108.
- (2) Won, J.; Kim, M.; Yi, Y. W.; Kim, Y. H.; Jung, N.; Kim, T. K., A magnetic nanoprobe technology for detecting molecular interactions in live cells. *Science* **2005**, 309, (5731), 121-125.
- (3) Gu, H. W.; Yang, Z. M.; Gao, J. H.; Chang, C. K.; Xu, B., Heterodimers of nanoparticles: Formation at a liquid-liquid interface and particle-specific surface modification by functional molecules. *J Am Chem Soc* **2005**, 127, (1), 34-35.
- (4) Lee, K. B.; Park, S.; Mirkin, C. A., Multicomponent magnetic nanorods for biomolecular separations. *Angew Chem Int Ed* **2004**, 43, (23), 3048-3050.
- (5) Salem, A. K.; Searson, P. C.; Leong, K. W., Multifunctional nanorods for gene delivery. *Nat Mater* **2003**, 2, (10), 668-671.
- (6) Mutin, P. H.; Lafond, V.; Popa, A. F.; Granier, M.; Markey, L.; Dereux, A., Selective surface modification of SiO₂-TiO₂ supports with phosphonic acids. *Chem Mater* **2004**, 16, (26), 5670-5675.
- (7) Michel, R.; Reviakine, I.; Sutherland, D.; Fokas, C.; Csucs, G.; Danuser, G.; Spencer, N. D.; Textor, M., A novel approach to produce biologically relevant chemical patterns at the nanometer scale: Selective molecular assembly patterning combined with colloidal lithography. *Langmuir* **2002**, 18, (22), 8580-8586.
- (8) Michel, R.; Lussi, J. W.; Csucs, G.; Reviakine, I.; Danuser, G.; Ketterer, B.; Hubbell, J. A.; Textor, M.; Spencer, N. D., Selective molecular assembly patterning: A new approach to micro- and nanochemical patterning of surfaces for biological applications. *Langmuir* **2002**, 18, (8), 3281-3287.
- (9) Ehrman, S. H.; Friedlander, S. K.; Zachariah, M. R., Phase segregation in binary SiO₂/TiO₂ and SiO₂/Fe₂O₃ nanoparticle aerosols formed in a premixed flame. *J Mater Res* **1999**, 14, (12), 4551-4561.
- (10) Hare, B. J.; Prestegard, J. H.; Engelman, D. M., Small angle x-ray scattering studies of magnetically oriented lipid bilayers. *Biophys J* **1995**, 69, (5), 1891-1896.
- (11) Ferrari, M., Cancer nanotechnology: Opportunities and challenges. *Nat Rev Cancer* **2005**, 5, (3), 161-171.
- (12) Yu, H.; Chen, M.; Rice, P. M.; Wang, S. X.; White, R. L.; Sun, S. H., Dumbbell-like bifunctional Au-Fe₃O₄ nanoparticles. *Nano Lett* **2005**, 5, (2), 379-382.

- (13) Koh, I.; Cipriano, B. H.; Ehrman, S. H.; Williams, D. N.; Holoman, T. R. P.; Martinez-Miranda, L. J., X-ray scattering study of the interactions between magnetic nanoparticles and living cell membranes. *J Appl Phys* **2005**, *97*, (8), 084310.
- (14) Massart, R., Preparation of Aqueous Magnetic Liquids in Alkaline and Acidic Media. *Ieee T Magn* **1981**, *17*, (2), 1247-1248.
- (15) Mayer, C. R.; Cabuil, V. V.; Lalot, T.; Thouvenot, R., Incorporation of Magnetic Nanoparticles in New Hybrid Networks Based on Heteropolyanions and Polyacrylamide. *Angew Chem Int Ed* **1999**, *38*, (24), 3672-3675.
- (16) Tartaj, P.; Morales, M. D.; Veintemillas-Verdaguer, S.; Gonzalez-Carreno, T.; Serna, C. J., The preparation of magnetic nanoparticles for applications in biomedicine. *J Phys D Appl Phys* **2003**, *36*, (13), R182-R197.
- (17) Hong, X.; Li, J.; Wang, M. J.; Xu, J. J.; Guo, W.; Li, J. H.; Bai, Y. B.; Li, T. J., Fabrication of magnetic luminescent nanocomposites by a layer-by-layer self-assembly approach. *Chem Mater* **2004**, *16*, (21), 4022-4027.
- (18) Jarjayes, O.; Fries, P. H.; Bidan, G., Magnetic-Properties of Fine Maghemite Particles in an Electroconducting Polymer Matrix. *J Magn Magn Mater* **1994**, *137*, (1-2), 205-218.
- (19) Bacri, J. C.; Perzynski, R.; Salin, D.; Cabuil, V.; Massart, R., Ionic Ferrofluids - a Crossing of Chemistry and Physics. *J Magn Magn Mater* **1990**, *85*, (1-3), 27-32.
- (20) Bacri, J. C.; Perzynski, R.; Salin, D.; Cabuil, V.; Massart, R., Phase-Diagram of an Ionic Magnetic Colloid - Experimental-Study of the Effect of Ionic-Strength. *J Colloid Interf Sci* **1989**, *132*, (1), 43-53.
- (21) Bacri, J. C.; Perzynski, R.; Salin, D.; Cabuil, V.; Massart, R., Magnetic Colloidal Properties of Ionic Ferrofluids. *J Magn Magn Mater* **1986**, *62*, (1), 36-46.
- (22) Massart, R.; Dubois, E.; Cabuil, V.; Hasmonay, E., Preparation and Properties of Monodisperse Magnetic Fluids. *J Magn Magn Mater* **1995**, *149*, (1-2), 1-5.
- (23) Lefebure, S.; Dubois, E.; Cabuil, V.; Neveu, S.; Massart, R., Monodisperse magnetic nanoparticles: Preparation and dispersion in water and oils. *J Mater Res* **1998**, *13*, (10), 2975-2981.
- (24) Massart, R.; Cabuil, V., Effect of Some Parameters on the Formation of Colloidal Magnetite in Alkaline-Medium - Yield and Particle-Size Control. *J Chim Phys Pcb* **1987**, *84*, (7-8), 967-973.
- (25) Huh, Y. M.; Jun, Y. W.; Song, H. T.; Kim, S.; Choi, J. S.; Lee, J. H.; Yoon, S.; Kim, K. S.; Shin, J. S.; Suh, J. S.; Cheon, J., In vivo magnetic resonance detection of cancer by using multifunctional magnetic nanocrystals. *J Am Chem Soc* **2005**, *127*, (35), 12387-12391.
- (26) Jun, Y. W.; Huh, Y. M.; Choi, J. S.; Lee, J. H.; Song, H. T.; Kim, S.; Yoon, S.; Kim, K. S.; Shin, J. S.; Suh, J. S.; Cheon, J., Nanoscale size effect of magnetic

- nanocrystals and their utilization for cancer diagnosis via magnetic resonance imaging. *J Am Chem Soc* **2005**, 127, (16), 5732-5733.
- (27) Hyeon, T.; Lee, S. S.; Park, J.; Chung, Y.; Na, H. B., Synthesis of highly crystalline and monodisperse maghemite nanocrystallites without a size-selection process. *J Am Chem Soc* **2001**, 123, (51), 12798-12801.
- (28) Park, J.; An, K. J.; Hwang, Y. S.; Park, J. G.; Noh, H. J.; Kim, J. Y.; Park, J. H.; Hwang, N. M.; Hyeon, T., Ultra-large-scale syntheses of monodisperse nanocrystals. *Nat Mater* **2004**, 3, (12), 891-895.
- (29) Sun, S.; Zeng, H., Size-controlled synthesis of magnetite nanoparticles. *J Am Chem Soc* **2002**, 124, (28), 8204-8205.
- (30) Stober, W.; Fink, A.; Bohn, E., Controlled Growth of Monodisperse Silica Spheres in Micron Size Range. *J Colloid Interf Sci* **1968**, 26, (1), 62-69.
- (31) Caruso, F., Nanoengineering of particle surfaces. *Adv Mater* **2001**, 13, (1), 11-22.
- (32) Mitchell, D. T.; Lee, S. B.; Trofin, L.; Li, N. C.; Nevanen, T. K.; Soderlund, H.; Martin, C. R., Smart nanotubes for bioseparations and biocatalysis. *J Am Chem Soc* **2002**, 124, (40), 11864-11865.
- (33) Zhang, Q. L.; Du, L. C.; Weng, Y. X.; Wang, L.; Chen, H. Y.; Li, J. Q., Particle-size-dependent distribution of carboxylate adsorption sites on TiO₂ nanoparticle surfaces: Insights into the surface modification of nanostructured TiO₂ electrodes. *J Phys Chem B* **2004**, 108, (39), 15077-15083.
- (34) Rajh, T.; Chen, L. X.; Lukas, K.; Liu, T.; Thurnauer, M. C.; Tiede, D. M., Surface restructuring of nanoparticles: An efficient route for ligand-metal oxide crosstalk. *J Phys Chem B* **2002**, 106, (41), 10543-10552.
- (35) Dimitrijevic, N. M.; Saponjic, Z. V.; Bartels, D. M.; Thurnauer, M. C.; Tiede, D. M.; Rajh, T., Revealing the nature of trapping sites in nanocrystalline titanium dioxide by selective surface modification. *J Phys Chem B* **2003**, 107, (30), 7368-7375.
- (36) Cozzoli, P. D.; Kornowski, A.; Weller, H., Low-temperature synthesis of soluble and processable organic-capped anatase TiO₂ nanorods. *J Am Chem Soc* **2003**, 125, (47), 14539-14548.
- (37) Yin, Y. D.; Lu, Y.; Xia, Y. N., A self-assembly approach to the formation of asymmetric dimers from monodispersed spherical colloids. *J Am Chem Soc* **2001**, 123, (4), 771-772.
- (38) Lu, Y.; Xiong, H.; Jiang, X. C.; Xia, Y. N.; Prentiss, M.; Whitesides, G. M., Asymmetric dimers can be formed by dewetting half-shells of gold deposited on the surfaces of spherical oxide colloids. *J Am Chem Soc* **2003**, 125, (42), 12724-12725.
- (39) Gu, H. W.; Zheng, R. K.; Zhang, X. X.; Xu, B., Facile one-pot synthesis of bifunctional heterodimers of nanoparticles: A conjugate of quantum dot and magnetic nanoparticles. *J Am Chem Soc* **2004**, 126, (18), 5664-5665.

- (40) Hirsch, L. R.; Stafford, R. J.; Bankson, J. A.; Sershen, S. R.; Rivera, B.; Price, R. E.; Hazle, J. D.; Halas, N. J.; West, J. L., Nanoshell-mediated near-infrared thermal therapy of tumors under magnetic resonance guidance. *Proc Natl Acad Sci USA* **2003**, 100, (23), 13549-13554.
- (41) Hirsch, L. R.; Jackson, J. B.; Lee, A.; Halas, N. J.; West, J., A whole blood immunoassay using gold nanoshells. *Anal Chem* **2003**, 75, (10), 2377-2381.
- (42) Brongersma, M. L., Nanoshells: gifts in a gold wrapper. *Nat Mater* **2003**, 2, (5), 296-297.
- (43) Caruntu, D.; Cushing, B. L.; Caruntu, G.; O'Connor, C. J., Attachment of gold nanograins onto colloidal magnetite nanocrystals. *Chem Mater* **2005**, 17, (13), 3398-3402.
- (44) Cozzoli, P. D.; Comparelli, R.; Fanizza, E.; Curri, M. L.; Agostiano, A.; Laub, D., Photocatalytic synthesis of silver nanoparticles stabilized by TiO₂ nanorods: A semiconductor/metal nanocomposite in homogeneous nonpolar solution. *J Am Chem Soc* **2004**, 126, (12), 3868-3879.
- (45) Naoi, K.; Ohko, Y.; Tatsuma, T., TiO₂ films loaded with silver nanoparticles: Control of multicolor photochromic behavior. *J Am Chem Soc* **2004**, 126, (11), 3664-3668.
- (46) Ohko, Y.; Tatsuma, T.; Fujii, T.; Naoi, K.; Niwa, C.; Kubota, Y.; Fujishima, A., Multicolour photochromism of TiO₂ films loaded with silver nanoparticles. *Nat Mater* **2003**, 2, (1), 29-31.
- (47) Tian, Y.; Tatsuma, T., Mechanisms and applications of plasmon-induced charge separation at TiO₂ films loaded with gold nanoparticles. *J Am Chem Soc* **2005**, 127, (20), 7632-7637.
- (48) Tada, H.; Ishida, T.; Takao, A.; Ito, S., Drastic enhancement of TiO₂-photocatalyzed reduction of nitrobenzene by loading Ag clusters. *Langmuir* **2004**, 20, (19), 7898-7900.
- (49) Chen, C. T.; Chen, Y. C., Fe₃O₄/TiO₂ core/shell nanoparticles as affinity probes for the analysis of phosphopeptides using TiO₂ surface-assisted laser desorption/ionization mass spectrometry. *Anal Chem* **2005**, 77, (18), 5912-5919.
- (50) Dawson, A.; Kamat, P. V., Semiconductor-metal nanocomposites. Photoinduced fusion and photocatalysis of gold-capped TiO₂ (TiO₂/Gold) nanoparticles. *J Phys Chem B* **2001**, 105, (5), 960-966.
- (51) Pratsinis, S. E., Flame aerosol synthesis of ceramic powders. *Prog Energy Combust* **1998**, 24, (3), 197-219.
- (52) Ulrich, G. D., Flame synthesis of fine particles. *Chem Eng News* **1984**, 62, (32), 22-29.
- (53) Miquel, P. F.; Hung, C. H.; Katz, J. L., Formation of V₂O₅-Based Mixed Oxides in Flames. *J Mater Res* **1993**, 8, (9), 2404-2413.

- (54) Hung, C. H.; Katz, J. L., Formation of Mixed-Oxide Powders in Flames .1. $\text{TiO}_2\text{-SiO}_2$. *J Mater Res* **1992**, 7, (7), 1861-1869.
- (55) Hung, C. H.; Miquel, P. F.; Katz, J. L., Formation of Mixed-Oxide Powders in Flames .2. $\text{SiO}_2\text{-GeO}_2$ and $\text{Al}_2\text{O}_3\text{-TiO}_2$. *J Mater Res* **1992**, 7, (7), 1870-1875.
- (56) Ehrman, S. H.; Friedlander, S. K.; Zachariah, M. R., Characteristics of $\text{SiO}_2/\text{TiO}_2$ nanocomposite particles formed in a premixed flat flame. *J Aerosol Sci* **1998**, 29, (5-6), 687-706.
- (57) Liu, Z. F.; Crumbaugh, G. M.; Davis, R. J., Effect of structure and composition on epoxidation of hexene catalyzed by microporous and mesoporous Ti-Si mixed oxides. *J Catal* **1996**, 159, (1), 83-89.
- (58) Zachariah, M. R.; Chin, D.; Semerjian, H. G.; Katz, J. L., Silica particle synthesis in a counterflow diffusion flame reactor. *Combust Flame* **1989**, 78, (3-4), 287-298.
- (59) Chung, S. L.; Katz, J. L., The Counterflow Diffusion Flame Burner - a New Tool for the Study of the Nucleation of Refractory Compounds. *Combust Flame* **1985**, 61, (3), 271-284.
- (60) Briesen, H.; Fuhrmann, A.; Pratsinis, S. E., The effect of precursor in flame synthesis of SiO_2 . *Chem Eng Sci* **1998**, 53, (24), 4105-4112.
- (61) Tsantilis, S.; Kammler, H. K.; Pratsinis, S. E., Population balance modeling of flame synthesis of titania nanoparticles. *Chem Eng Sci* **2002**, 57, (12), 2139-2156.
- (62) Kim, S. H.; Liu, B. Y. H.; Zachariah, M. R., Ultrahigh surface area nanoporous silica particles via an aero-sol-gel process. *Langmuir* **2004**, 20, (7), 2523-2526.
- (63) Prakash, A.; McCormick, A. V.; Zachariah, M. R., Aero-sol-gel synthesis of nanoporous iron-oxide particles: A potential oxidizer for nanoenergetic materials. *Chem Mater* **2004**, 16, (8), 1466-1471.
- (64) Prakash, A.; McCormick, A. V.; Zachariah, M. R., Tuning the reactivity of energetic nanoparticles by creation of a core-shell nanostructure. *Nano Lett* **2005**, 5, (7), 1357-1360.
- (65) Tartaj, P.; Gonzalez-Carreno, T.; Serna, C. J., Single-step nanoengineering of silica coated maghemite hollow spheres with tunable magnetic properties. *Adv Mater* **2001**, 13, (21), 1620-1624.
- (66) Li, Y. Z.; Kim, S. J., Synthesis and characterization of nano titania particles embedded in mesoporous silica with both high photocatalytic activity and adsorption capability. *J Phys Chem B* **2005**, 109, (25), 12309-12315.
- (67) Jung, K. Y.; Park, S. B., Enhanced photoactivity of silica-embedded titania particles prepared by sol-gel process for the decomposition of trichloroethylene. *Appl Catal B-Environ* **2000**, 25, (4), 249-256.

- (68) Panayotov, D. A.; Paul, D. K.; Yates, J. T., Photocatalytic oxidation of 2-chloroethyl ethyl sulfide on TiO₂-SiO₂ powders. *J Phys Chem B* **2003**, 107, (38), 10571-10575.
- (69) Hu, C.; Tang, Y. C.; Yu, J. C.; Wong, P. K., Photocatalytic degradation of cationic blue X-GRL adsorbed on TiO₂/SiO₂ photocatalyst. *Appl Catal B-Environ* **2003**, 40, (2), 131-140.
- (70) Hu, C.; Wang, Y. Z.; Tang, H. X., Preparation and characterization of surface bond-conjugated TiO₂/SiO₂ and photocatalysis for azo dyes. *Appl Catal B-Environ* **2001**, 30, (3-4), 277-285.
- (71) Hirano, M.; Ota, K.; Iwata, H., Direct formation of anatase (TiO₂)/silica (SiO₂) composite nanoparticles with high phase stability of 1300 degrees C from acidic solution by hydrolysis under hydrothermal condition. *Chem Mater* **2004**, 16, (19), 3725-3732.
- (72) Hounslow, M. J.; Ryall, R. L.; Marshall, V. R., A Discretized Population Balance for Nucleation, Growth, and Aggregation. *Aiche J* **1988**, 34, (11), 1821-1832.
- (73) Jeong, J. I.; Choi, M., A sectional method for the analysis of growth of polydisperse non-spherical particles undergoing coagulation and coalescence. *J Aerosol Sci* **2001**, 32, (5), 565-582.
- (74) Lee, B. W.; Jeong, J. I.; Hwang, J. Y.; Choi, M.; Chung, S. H., Analysis of growth of non-spherical silica particles in a counterflow diffusion flame considering chemical reactions, coagulation and coalescence. *J Aerosol Sci* **2001**, 32, (2), 165-185.
- (75) Tsantilis, S.; Pratsinis, S. E., Evolution of primary and aggregate particle-size distributions by coagulation and sintering. *Aiche J* **2000**, 46, (2), 407-415.
- (76) Xiong, Y.; Pratsinis, S. E., Formation of Agglomerate Particles by Coagulation and Sintering .1. A 2-Dimensional Solution of the Population Balance Equation. *J Aerosol Sci* **1993**, 24, (3), 283-300.
- (77) Ulrich, G. D.; Riehl, J. W., Aggregation and Growth of Sub-Micron Oxide Particles in Flames. *J Colloid Interf Sci* **1982**, 87, (1), 257-265.
- (78) Lindackers, D.; Strecker, M. G. D.; Roth, P.; Janzen, C.; Pratsinis, S. E., Formation and growth of SiO₂ particles in low pressure H₂/O₂/Ar flames doped with SiH₄. *Combust Sci Technol* **1997**, 123, (1-6), 287-315.
- (79) Dobbins, R. A.; Megaridis, C. M., Morphology of Flame-Generated Soot as Determined by Thermophoretic Sampling. *Langmuir* **1987**, 3, (2), 254-259.
- (80) Ulman, A., Formation and structure of self-assembled monolayers. *Chem Rev* **1996**, 96, (4), 1533-1554.
- (81) Silberzan, P.; Leger, L.; Ausserre, D.; Benattar, J. J., Silanation of Silica Surfaces - a New Method of Constructing Pure or Mixed Monolayers. *Langmuir* **1991**, 7, (8), 1647-1651.

- (82) Sagiv, J., Organized Monolayers by Adsorption .1. Formation and Structure of Oleophobic Mixed Monolayers on Solid-Surfaces. *J Am Chem Soc* **1980**, 102, (1), 92-98.
- (83) Wasserman, S. R.; Tao, Y. T.; Whitesides, G. M., Structure and Reactivity of Alkylsiloxane Monolayers Formed by Reaction of Alkyltrichlorosilanes on Silicon Substrates. *Langmuir* **1989**, 5, (4), 1074-1087.
- (84) Legrange, J. D.; Markham, J. L.; Kurkjian, C. R., Effects of Surface Hydration on the Deposition of Silane Monolayers on Silica. *Langmuir* **1993**, 9, (7), 1749-1753.
- (85) Onclin, S.; Ravoo, B. J.; Reinhoudt, D. N., Engineering silicon oxide surfaces using self-assembled monolayers. *Angew Chem Int Ed* **2005**, 44, (39), 6282-6304.
- (86) Levy, L.; Sahoo, Y.; Kim, K. S.; Bergey, E. J.; Prasad, P. N., Nanochemistry: Synthesis and characterization of multifunctional nanoclinics for biological applications. *Chem Mater* **2002**, 14, (9), 3715-3721.
- (87) Son, S. J.; Reichel, J.; He, B.; Schuchman, M.; Lee, S. B., Magnetic nanotubes for magnetic-field-assisted bioseparation, biointeraction, and drug delivery. *J Am Chem Soc* **2005**, 127, (20), 7316-7317.
- (88) Bauer, L. A.; Birenbaum, N. S.; Meyer, G. J., Biological applications of high aspect ratio nanoparticles. *J Mater Chem* **2004**, 14, (4), 517-526.
- (89) Kohler, N.; Fryxell, G. E.; Zhang, M., A bifunctional poly(ethylene glycol) silane immobilized on metallic oxide-based nanoparticles for conjugation with cell targeting agents. *J Am Chem Soc* **2004**, 126, (23), 7206-7211.
- (90) Veiseh, O.; Sun, C.; Gunn, J.; Kohler, N.; Gabikian, P.; Lee, D.; Bhattarai, N.; Ellenbogen, R.; Sze, R.; Hallahan, A.; Olson, J.; Zhang, M. Q., Optical and MRI multifunctional nanoprobe for targeting gliomas. *Nano Lett* **2005**, 5, (6), 1003-1008.
- (91) Giri, S.; Trewyn, B. G.; Stellmaker, M. P.; Lin, V. S. Y., Stimuli-responsive controlled-release delivery system based on mesoporous silica nanorods capped with magnetic nanoparticles. *Angew Chem Int Ed* **2005**, 44, (32), 5038-5044.
- (92) Hubbuch, J. J.; Thomas, O. R. T., High-gradient magnetic affinity separation of trypsin from porcine pancreatin. *Biotechnol Bioeng* **2002**, 79, (3), 301-313.
- (93) Takafuji, M.; Ide, S.; Ihara, H.; Xu, Z. H., Preparation of poly(1-vinylimidazole)-grafted magnetic nanoparticles and their application for removal of metal ions. *Chem Mater* **2004**, 16, (10), 1977-1983.
- (94) Mikhaylova, M.; Kim, D. K.; Berry, C. C.; Zagorodni, A.; Toprak, M.; Curtis, A. S. G.; Muhammed, M., BSA immobilization on amine-functionalized superparamagnetic iron oxide nanoparticles. *Chem Mater* **2004**, 16, (12), 2344-2354.

- (95) Xu, Z. H.; Liu, Q. X.; Finch, J. A., Silanation and stability of 3-aminopropyl triethoxy silane on nanosized superparamagnetic particles: I. Direct silanation. *Applied Surface Science* **1997**, 120, (3-4), 269-278.
- (96) Kim, D. K.; Mikhaylova, M.; Zhang, Y.; Muhammed, M., Protective coating of superparamagnetic iron oxide nanoparticles. *Chem Mater* **2003**, 15, (8), 1617-1627.
- (97) Dyal, A.; Loos, K.; Noto, M.; Chang, S. W.; Spagnoli, C.; Shafi, K. V.; Ulman, A.; Cowman, M.; Gross, R. A., Activity of *Candida rugosa* lipase immobilized on γ -Fe₂O₃ magnetic nanoparticles. *J Am Chem Soc* **2003**, 125, (7), 1684-1685.
- (98) Dimitrijevic, N. M.; Rajh, T.; Saponjic, Z. V.; de la Garza, L.; Tiede, D. M., Light-induced charge separation and redox chemistry at the surface of TiO₂/host-guest hybrid nanoparticles. *J Phys Chem B* **2004**, 108, (26), 9105-9110.
- (99) Mutin, P. H.; Guerrero, G.; Vioux, A., Hybrid materials from organophosphorus coupling molecules. *J Mater Chem* **2005**, 15, (35-36), 3761-3768.
- (100) Tosatti, S.; Michel, R.; Textor, M.; Spencer, N. D., Self-assembled monolayers of dodecyl and hydroxy-dodecyl phosphates on both smooth and rough titanium and titanium oxide surfaces. *Langmuir* **2002**, 18, (9), 3537-3548.
- (101) Hofer, R.; Textor, M.; Spencer, N. D., Alkyl phosphate monolayers, self-assembled from aqueous solution onto metal oxide surfaces. *Langmuir* **2001**, 17, (13), 4014-4020.
- (102) Wang, P.; Zakeeruddin, S. M.; Humphry-Baker, R.; Moser, J. E.; Gratzel, M., Molecular-scale interface engineering of TiO₂ nanocrystals: Improving the efficiency and stability of dye-sensitized solar cells. *Adv Mater* **2003**, 15, (24), 2101-2104.
- (103) Xu, C. J.; Xu, K. M.; Gu, H. W.; Zheng, R. K.; Liu, H.; Zhang, X. X.; Guo, Z. H.; Xu, B., Dopamine as a robust anchor to immobilize functional molecules on the iron oxide shell of magnetic nanoparticles. *J Am Chem Soc* **2004**, 126, (32), 9938-9939.
- (104) Paunesku, T.; Rajh, T.; Wiederrecht, G.; Maser, J.; Vogt, S.; Stojicevic, N.; Protic, M.; Lai, B.; Oryhon, J.; Thurnauer, M.; Woloschak, G., Biology of TiO₂-oligonucleotide nanocomposites. *Nat Mater* **2003**, 2, (5), 343-346.
- (105) Rajh, T.; Saponjic, Z.; Liu, J. Q.; Dimitrijevic, N. M.; Scherer, N. F.; Vega-Arroyo, M.; Zapol, P.; Curtiss, L. A.; Thurnauer, M. C., Charge transfer across the nanocrystalline-DNA interface: Probing DNA recognition. *Nano Lett* **2004**, 4, (6), 1017-1023.
- (106) Dimitrijevic, N. M.; Saponjic, Z. V.; Rabatic, B. M.; Rajh, T., Assembly and charge transfer in hybrid TiO₂ architectures using biotin-avidin as a connector. *J Am Chem Soc* **2005**, 127, (5), 1344-1345.

- (107) Saponjic, Z. V.; Dimitrijevic, N. M.; Tiede, D. M.; Goshe, A. J.; Zuo, X. B.; Chen, L. X.; Barnard, A. S.; Zapol, P.; Curtiss, L.; Rajh, T., Shaping nanometer-scale architecture through surface chemistry. *Adv Mater* **2005**, *17*, (8), 965-971.
- (108) Dalsin, J. L.; Lin, L. J.; Tosatti, S.; Voros, J.; Textor, M.; Messersmith, P. B., Protein resistance of titanium oxide surfaces modified by biologically inspired mPEG-DOPA. *Langmuir* **2005**, *21*, (2), 640-646.
- (109) Dalsin, J. L.; Hu, B. H.; Lee, B. P.; Messersmith, P. B., Mussel adhesive protein mimetic polymers for the preparation of nonfouling surfaces. *J Am Chem Soc* **2003**, *125*, (14), 4253-4258.
- (110) Boal, A. K.; Das, K.; Gray, M.; Rotello, V. M., Monolayer exchange chemistry of γ -Fe₂O₃ nanoparticles. *Chem Mater* **2002**, *14*, (6), 2628-2636.
- (111) Frankamp, B. L.; Boal, A. K.; Tuominen, M. T.; Rotello, V. M., Direct control of the magnetic interaction between iron oxide nanoparticles through dendrimer-mediated self-assembly. *J Am Chem Soc* **2005**, *127*, (27), 9731-9735.
- (112) Laibinis, P. E.; Hickman, J. J.; Wrighton, M. S.; Whitesides, G. M., Orthogonal Self-Assembled Monolayers - Alkanethiols on Gold and Alkane Carboxylic-Acids on Alumina. *Science* **1989**, *245*, (4920), 845-847.
- (113) Gardner, T. J.; Frisbie, C. D.; Wrighton, M. S., Systems for Orthogonal Self-Assembly of Electroactive Monolayers on Au and ITO - an Approach to Molecular Electronics. *J Am Chem Soc* **1995**, *117*, (26), 6927-6933.
- (114) Veiseh, M.; Wickes, B. T.; Castner, D. G.; Zhang, M. Q., Guided cell patterning on gold-silicon dioxide substrates by surface molecular engineering. *Biomaterials* **2004**, *25*, (16), 3315-3324.
- (115) Curreli, M.; Li, C.; Sun, Y. H.; Lei, B.; Gundersen, M. A.; Thompson, M. E.; Zhou, C. W., Selective functionalization of In₂O₃ nanowire mat devices for biosensing applications. *J Am Chem Soc* **2005**, *127*, (19), 6922-6923.
- (116) Bailey, J. E. O., D.F., *Biochemical engineering fundamentals*. 2nd ed.; McGraw-Hill: New York, 1986; 382-388.
- (117) <http://www.cat.cc.md.us/courses/bio141/lecguides/unit1/prostruct/u1fig10a.html>.
- (118) Chiras, D. D., *Human biology*. 5th ed.; Jones and Bartlett: 2005.
- (119) <http://www.biologie.uni-hamburg.de/b-online/e22/22.htm>.
- (120) Perez, J. M.; O'Loughin, T.; Simeone, F. J.; Weissleder, R.; Josephson, L., DNA-based magnetic nanoparticle assembly acts as a magnetic relaxation nanoswitch allowing screening of DNA-cleaving agents. *J Am Chem Soc* **2002**, *124*, (12), 2856-2857.
- (121) Jordan, A.; Scholz, R.; Wust, P.; Schirra, H.; Schiestel, T.; Schmidt, H.; Felix, R., Endocytosis of dextran and silan-coated magnetite nanoparticles and the effect of intracellular hyperthermia on human mammary carcinoma cells in vitro. *J Magn Magn Mater* **1999**, *194*, (1-3), 185-196.

- (122) Jordan, A.; Scholz, R.; Wust, P.; Föhling, H.; Felix, R., Magnetic fluid hyperthermia (MFH): Cancer treatment with AC magnetic field induced excitation of biocompatible superparamagnetic nanoparticles. *J Magn Magn Mater* **1999**, 201, 413-419.
- (123) Wang, D. S.; He, J. B.; Rosenzweig, N.; Rosenzweig, Z., Superparamagnetic Fe₂O₃ Beads-CdSe/ZnS quantum dots core-shell nanocomposite particles for cell separation. *Nano Lett* **2004**, 4, (3), 409-413.
- (124) Perez, J. M.; Simeone, F. J.; Saeki, Y.; Josephson, L.; Weissleder, R., Viral-induced self-assembly of magnetic nanoparticles allows the detection of viral particles in biological media. *J Am Chem Soc* **2003**, 125, (34), 10192-10193.
- (125) Ma, M.; Zhang, Y.; Yu, W.; Shen, H. Y.; Zhang, H. Q.; Gu, N., Preparation and characterization of magnetite nanoparticles coated by amino silane. *Colloid Surface A* **2003**, 212, (2-3), 219-226.
- (126) Wadu-Mesthrige, K.; Amro, N. A.; Garno, J. C.; Xu, S.; Liu, G., Fabrication of nanometer-sized protein patterns using atomic force microscopy and selective immobilization. *Biophys J* **2001**, 80, (4), 1891-1899.
- (127) Wadu-Mesthrige, K.; Xu, S.; Amro, N. A.; Liu, G. Y., Fabrication and imaging of nanometer-sized protein patterns. *Langmuir* **1999**, 15, (25), 8580-8583.
- (128) Yamaura, M.; Camilo, R. L.; Sampaio, L. C.; Macedo, M. A.; Nakamura, M.; Toma, H. E., Preparation and characterization of (3-aminopropyl) triethoxysilane-coated magnetite nanoparticles. *J Magn Magn Mater* **2004**, 279, (2-3), 210-217.
- (129) Morgan, M.; Okamoto, K.; Kahn, J. D.; English, D. S., Single Molecule Spectroscopic Determination of Lac Repressor-DNA Loop Conformational Populations. *Biophys J* **2005**, 89, 2588-2596.
- (130) Okamoto, K.; Shook, C.; Bivona, L.; Lee, S. B.; English, D. S., Direct observation of wetting and diffusion in the hydrophobic interior of silica nanotubes. *Nano Lett* **2004**, 4, (2), 233-239.
- (131) *Handbook of X-ray photoelectron spectroscopy*. Chastain, J. U.; King, R. C.ed.; Physical Electronics Inc: Eden Prairie, 1995.
- (132) Silverton, E. W.; Navia, M. A.; Davies, D. R., Three-dimensional structure of an intact human immunoglobulin. *Proc Natl Acad Sci U S A* **1977**, 74, (11), 5140-4.
- (133) FRET Efficiency is defined as $Eff=(1-IDA/ID)$ where IDA is the intensity when donor and acceptor are both present and ID is the intensity when donor only is present
- (134) Gu, H. W.; Ho, P. L.; Tsang, K. W. T.; Yu, C. W.; Xu, B., Using biofunctional magnetic nanoparticles to capture Gram-negative bacteria at an ultra-low concentration. *Chem Commun* **2003**, (15), 1966-1967.
- (135) Gu, H. W.; Ho, P. L.; Tsang, K. W. T.; Wang, L.; Xu, B., Using biofunctional magnetic nanoparticles to capture vancomycin-resistant enterococci and other

- gram-positive bacteria at ultralow concentration. *J Am Chem Soc* **2003**, 125, (51), 15702-15703.
- (136) Xu, C. J.; Xu, K. M.; Gu, H. W.; Zhong, X. F.; Guo, Z. H.; Zheng, R. K.; Zhang, X. X.; Xu, B., Nitriolotriacetic acid-modified magnetic nanoparticles as a general agent to bind histidine-tagged proteins. *J Am Chem Soc* **2004**, 126, (11), 3392-3393.
- (137) Bucak, S.; Jones, D. A.; Laibinis, P. E.; Hatton, T. A., Protein separations using colloidal magnetic nanoparticles. *Biotechnol Progr* **2003**, 19, (2), 477-484.
- (138) Martin, B. R.; Dermody, D. J.; Reiss, B. D.; Fang, M. M.; Lyon, L. A.; Natan, M. J.; Mallouk, T. E., Orthogonal self-assembly on colloidal gold-platinum nanorods. *Adv Mater* **1999**, 11, (12), 1021-1025.
- (139) Nicewarner-Pena, S. R.; Freeman, R. G.; Reiss, B. D.; He, L.; Pena, D. J.; Walton, I. D.; Cromer, R.; Keating, C. D.; Natan, M. J., Submicrometer metallic barcodes. *Science* **2001**, 294, (5540), 137-141.
- (140) Teranishi, T.; Inoue, Y.; Nakaya, M.; Oumi, Y.; Sano, T., Nanoacorns: Anisotropically phase-segregated CoPd sulfide nanoparticles. *J Am Chem Soc* **2004**, 126, (32), 9914-9915.
- (141) Bauer, L. A.; Reich, D. H.; Meyer, G. J., Selective functionalization of two-component magnetic nanowires. *Langmuir* **2003**, 19, (17), 7043-7048.
- (142) Keating, C. D.; Natan, M. J., Striped metal nanowires as building blocks and optical tags. *Adv Mater* **2003**, 15, (5), 451-454.
- (143) Birenbaum, N. S.; Lai, B. T.; Chen, C. S.; Reich, D. H.; Meyer, G. J., Selective noncovalent adsorption of protein to bifunctional metallic nanowire surfaces. *Langmuir* **2003**, 19, (23), 9580-9582.
- (144) Zorn, G.; Gotman, I.; Gutmanas, E. Y.; Adadi, R.; Salitra, G.; Sukenik, C. N., Surface modification of Ti₄₅Nb alloy with an alkylphosphonic acid self-assembled monolayer. *Chem Mater* **2005**, 17, (16), 4218-4226.
- (145) Lukes, I.; Borbaruah, M.; Quin, L. D., Direct Reaction of Phosphorus-Acids with Hydroxy of a Silanol and on the Silica-Gel Surface. *J Am Chem Soc* **1994**, 116, (5), 1737-1741.
- (146) Lafond, V.; Gervais, C.; Maquet, J.; Prochnow, D.; Babonneau, F.; Mutin, P. H., ¹⁷O MAS NMR study of the bonding mode of phosphonate coupling molecules in a titanium oxo-alkoxo-phosphonate and in titania-based hybrid materials. *Chem Mater* **2003**, 15, (21), 4098-4103.
- (147) Wang, C. Y.; Groenzin, H.; Shultz, M. J., Molecular species on nanoparticulate anatase TiO₂ film detected by sum frequency generation: Trace hydrocarbons and hydroxyl groups. *Langmuir* **2003**, 19, (18), 7330-7334.
- (148) Nakatsuka, T.; Kawasaki, H.; Itadani, K.; Yamashita, S., Phosphate Coupling Agents for Calcium-Carbonate Filler. *J Appl Polym Sci* **1982**, 27, (1), 259-269.

- (149) Pawsey, S.; McCormick, M.; De Paul, S.; Graf, R.; Lee, Y. S.; Reven, L.; Spiess, H. W., ¹H fast MAS NMR studies of hydrogen-bonding interactions in self-assembled monolayers. *J Am Chem Soc* **2003**, 125, (14), 4174-4184.
- (150) Pawsey, S.; Yach, K.; Reven, L., Self-assembly of carboxyalkylphosphonic acids on metal oxide powders. *Langmuir* **2002**, 18, (13), 5205-5212.
- (151) *Scientific and clinical applications of magnetic microspheres*. Häfeli, U. S., W.; Teller, J.; Zborowski, M.ed.; Plenum: New York, 1997.
- (152) Weitschies, W. K., R.; Bunte, R.; Trahms, L., *Pharm Pharmacol Lett* **1997**, 7, (1), 5-8.
- (153) Enpuku, K. M., T; Gima, T; Kuroki, Y; Itoh, Y.; Yamashita, M; Katakura, Y.; Kuhara, S., Detection of magnetic nanoparticles with superconducting quantum interference device (SQUID) magnetometer and application to Immunoassays. *Jpn J Appl Phys, Part 2* **1999**, 38, (L1102-L1105).
- (154) Giri, A. K. C., K.M.; Humfeld, K.D.; Majetich, S.A., AC magnetic properties of FeCo nanocomposites. *IEEE Trans. Magn.* **2000**, 36, (5), 3026-3028.
- (155) Wilhelm, C.; Gazeau, F.; Roger, J.; Pons, J. N.; Bacri, J. C., Interaction of anionic superparamagnetic nanoparticles with cells: Kinetic analyses of membrane adsorption and subsequent internalization. *Langmuir* **2002**, 18, (21), 8148-8155.
- (156) Wilhelm, C.; Billotey, C.; Roger, J.; Pons, J. N.; Bacri, J. C.; Gazeau, F., Intracellular uptake of anionic superparamagnetic nanoparticles as a function of their surface coating. *Biomaterials* **2003**, 24, (6), 1001-1011.
- (157) Fabre, P.; Casagrande, C.; Veyssie, M.; Cabuil, V. V.; Massart, R., Ferrosmectics: A new magnetic and mesomorphic phase. *Phys Rev Lett* **1990**, 64, (5), 539-542.
- (158) Ponsinet, V.; Fabre, P.; Veyssie, M.; Auvray, L., A Small-Angle Neutron-Scattering Study of the Ferrosmectic Phase. *J Phys Li* **1993**, 3, (7), 1021-1039.
- (159) Ponsinet, V.; Fabre, P., Modification of the interactions in a lamellar phase by the presence of nanoparticles. *J Phys Li* **1996**, 6, (7), 955-960.
- (160) Prosser, R. S.; Hwang, J. S.; Vold, R. R., Magnetically aligned phospholipid bilayers with positive ordering: a new model membrane system. *Biophys J* **1998**, 74, (5), 2405-2418.
- (161) Spoliansky, D. P., V.; Ferre, J.; Jamet, J.-P., Magneto-optical study of the orientation confinement of particles in ferrolyotropic systems. *Eur Phys J E* **2000**, 1, 227-235.
- (162) Esfahani, M.; Limbrick, A. R.; Knutton, S.; Oka, T.; Wakil, S. J., The molecular organization of lipids in the membrane of Escherichia coli: phase transitions. *Proc Natl Acad Sci U S A* **1971**, 68, (12), 3180-3184.
- (163) Shechter, E.; Kaback, H. R.; Gulikkrz.T, Correlations between Fluorescence, X-Ray-Diffraction, and Physiological Properties in Cytoplasmic Membrane

- Vesicles Isolated from *Escherichia coli*. *Biochim Biophys Acta* **1972**, 274, (2), 466-477.
- (164) Shechter, E.; Letellie, L.; Gulikkrz, T., Relations between Structure and Function in Cytoplasmic Membrane-Vesicles Isolated from an *Escherichia coli* Fatty-Acid Auxotroph - High-Angle X-Ray-Diffraction, Freeze-Etch Electron-Microscopy and Transport Studies. *Eur J Biochem* **1974**, 49, (1), 61-76.
- (165) Letellier, L.; Moudden, H.; Shechter, E., Lipid and Protein Segregation in Escherichia-Coli Membrane - Morphological and Structural Study of Different Cytoplasmic Membrane-Fractions. *P Natl Acad Sci USA* **1977**, 74, (2), 452-456.
- (166) Linden, C. D.; Blasie, J. K.; Fox, C. F., A confirmation of the phase behavior of Escherichia coli cytoplasmic membrane lipids by X-ray diffraction. *Biochemistry* **1977**, 16, (8), 1621-1625.
- (167) Harder, M. E.; Banaszak, L. J., Small angle x-ray scattering from the inner and outer membranes from Escherichia coli. *Biochim Biophys Acta* **1979**, 552, (1), 89-102.
- (168) Nakayama, H.; Mitsui, T.; Nishihara, M.; Kito, M., Relation between Growth Temperature of Escherichia-Coli and Phase-Transition Temperatures of Its Cytoplasmic and Outer Membranes. *Biochim Biophys Acta* **1980**, 601, (1), 1-10.
- (169) Prenner, E. J.; Lewis, R. N.; Neuman, K. C.; Gruner, S. M.; Kondejewski, L. H.; Hodges, R. S.; McElhaney, R. N., Nonlamellar phases induced by the interaction of gramicidin S with lipid bilayers. A possible relationship to membrane-disrupting activity. *Biochemistry* **1997**, 36, (25), 7906-7916.
- (170) Staudegger, E.; Prenner, E. J.; Kriechbaum, M.; Degovics, G.; Lewis, R. N.; McElhaney, R. N.; Lohner, K., X-ray studies on the interaction of the antimicrobial peptide gramicidin S with microbial lipid extracts: evidence for cubic phase formation. *Biochim Biophys Acta* **2000**, 1468, (1-2), 213-230.
- (171) Williams, D. N.; Ehrman, S. H.; Pulliam-Holoman, T. R., Unpublished.
- (172) Sambrook, J. R. D. W., *Molecular Cloning: A Laboratory Manual*. 3rd ed.; Cold Spring Harbor Laboratory: New York, 2001.
- (173) Ranck, J. L., X-Ray-Diffraction Studies of the Phase-Transitions of Hydrocarbon Chains in Bilayer Systems - Statics and Dynamics. *Chem Phys Lipids* **1983**, 32, (3-4), 251-270.
- (174) Koh, I.; Kurihara, L. K.; Martínez-Miranda, L. J., Unpublished.
- (175) Li, Y. Q.; Zhang, G.; Nurmikko, A. V.; Sun, S. H., Enhanced magneto-optical response in dumbbell-like Ag-CoFe₂O₄ nanoparticle pairs. *Nano Lett* **2005**, 5, (9), 1689-1692.
- (176) Subramanian, V.; Wolf, E. E.; Kamat, P. V., Influence of metal/metal ion concentration on the photocatalytic activity of TiO₂-Au composite nanoparticles. *Langmuir* **2003**, 19, (2), 469-474.

- (177) Chan, S. C.; Barteau, M. A., Preparation of highly uniform Ag/TiO₂ and Au/TiO₂ supported nanoparticle catalysts by photodeposition. *Langmuir* **2005**, 21, (12), 5588-5595.
- (178) Zhang, L. Z.; Yu, J. C.; Yip, H. Y.; Li, Q.; Kwong, K. W.; Xu, A. W.; Wong, P. K., Ambient light reduction strategy to synthesize silver nanoparticles and silver-coated TiO₂ with enhanced photocatalytic and bactericidal activities. *Langmuir* **2003**, 19, (24), 10372-10380.
- (179) Zhang, F. X.; Guan, N. J.; Li, Y. Z.; Zhang, X.; Chen, J. X.; Zeng, H. S., Control of morphology of silver clusters coated on titanium dioxide during photocatalysis. *Langmuir* **2003**, 19, (20), 8230-8234.
- (180) West, A. R., *Solid state chemistry and its applications*. ed.; John Wiley & Sons: Singapore, 1984; 122.